

Preparation of the Operation and Calibration of the Fluorescence Detector of AugerPrime

Zur Erlangung des akademischen Grades eines

Doktors der Naturwissenschaften

an der KIT - Fakultät für Physik des
Karlsruher Instituts für Technologie (KIT)

genehmigte

Dissertation

von

M. Sc. Joachim Friedemann Debatin

aus Mühlacker

Tag der mündlichen Prüfung: 8. November 2019

Referent: Prof. Dr. Ralph Engel

Korreferent: Prof. Dr. Guido Drexlin

Betreuer: Dr. Michael Unger



This document is licensed under a Creative Commons Attribution-ShareAlike 4.0 International License (CC BY-SA 4.0): <https://creativecommons.org/licenses/by-sa/4.0/deed.en>

Abstract

In this thesis, two studies are presented that are relevant for the future operation of the Pierre Auger Observatory until 2030 and possibly beyond: The performance of the Fluorescence Detector under increased night-sky background to increase the current data taking rate, and a novel technique to set the absolute energy scale of the Observatory.

As a part of the upgrade of the Pierre Auger Observatory, the duty cycle of the Fluorescence Detector will be increased by 50 %. This is beneficial for many analyses of the Pierre Auger Observatory, but especially for mass composition studies using the unrivaled capabilities of the Fluorescence Detector to observe the development of air showers in the atmosphere. To increase the duty cycle of the Fluorescence Detector the PMTs have to be able to cope with a higher background light flux and, therefore, the gain is reduced by a factor of 10. Simulations were performed to estimate the additional amount of events and to study the data quality depending on the night-sky background. The results show that the full reconstruction efficiency over the Surface Detector array is reached at $10^{19.5}$ eV, thus the number of additional events above this energy scales with the measurement time. The decrease in energy and X_{\max} resolution was found to be less than 50 %. In test measurements during high night-sky background, we have shown that the detector behaves well under switching of gain levels. 28 events were reconstructed from the 9 days of data taking at low gain, of which 3 were in the targeted energy range above 10^{19} eV.

A new method for the end-to-end calibration of large-aperture telescopes, called the “XY-Scanner”, is introduced. The energy calibration of the Fluorescence Detector sets the energy scale of the whole experiment. The good resolution of the calorimetric energy measurement is used to cross calibrate the Surface Detector with hybrid events. Instead of illuminating the whole aperture at once, the new technique combines many measurements with a smaller light source at different positions in the aperture. We present simulations, performed to find the optimal discretization grid of the illuminated area and to estimate the systematic uncertainties. In three measurement campaigns, XY-Scanners were installed and test measurements were taken successfully at seven telescopes. In between the measurement campaigns, the optical properties of the telescopes change by the accumulation of dust on optical components. This was also measured by cleaning a mirror. The measurements finally are used to derive the relative energy calibration of the telescopes. The relative differences are within ± 5 %, for the HEAT telescopes the calibration was found to be $0.75 \pm 0,05$ relative to Coihueco. The new calibration method yields reproducible results within 0.5 % and thus is well suited to replace the drum calibration method.

Zusammenfassung

In der vorliegenden Arbeit werden zwei Studien vorgestellt, die für den zukünftigen Betrieb des Pierre Auger Observatoriums bis 2030, möglicherweise darüber hinaus, relevant sind: Der Betrieb des Fluoreszenzdetektors bei erhöhtem Hintergrundlicht um die Datenerfassungsrate zu steigern sowie eine neue Technik zur absoluten Kalibrierung der optischen Teleskope mit großer Apertur.

Im Rahmen des Ausbaus des Pierre Auger Observatoriums zu AugerPrime wird die relative Messzeit des Fluoreszenzdetektors um 50 % erhöht. Dies ist für viele Analysen des Pierre Auger Observatoriums von Vorteil, jedoch vor allem für die Untersuchung der Massenzusammensetzung der kosmischen Strahlung, bei der die unerreichten Fähigkeiten des Fluoreszenzdetektors zur Beobachtung der longitudinalen Schauerentwicklung in der Atmosphäre genutzt werden. Um die relative Messzeit des Fluoreszenzdetektors zu erhöhen, muss die Verstärkung um den Faktor 10 reduziert werden, damit das höhere Hintergrundlicht bewältigt werden kann. Es wurden Simulationen durchgeführt, um die Anzahl der zusätzlichen Ereignisse abzuschätzen und die Qualität der Daten in Abhängigkeit vom Hintergrundlicht zu untersuchen. Es konnte gezeigt werden, dass die volle Rekonstruktionseffizienz über dem Oberflächendetektorarray bei $1 \times 10^{19,5}$ eV erreicht wird, darüber skaliert die Anzahl der zusätzlichen Ereignisse mit der Messzeit. Die Verschlechterung der Energie- und X_{\max} -Auflösung beträgt weniger als 50 %. In Testmessungen bei erhöhtem Hintergrundlicht zeigte sich, dass der Detektor auch beim Umschalten der Verstärkung gut funktioniert. Aus neun Nächten Messungen mit geringerer Verstärkung wurden 28 Luftschaer rekonstruiert. Drei davon lagen im anvisierten Energiebereich über 1×10^{19} eV.

Eine neue Methode zur vollständigen Kalibrierung von Fluoreszenzteleskopen, der sogenannte "XY-Scanner" wird vorgestellt. Die Energiekalibrierung des Fluoreszenzdetektors legt die Energieskala des gesamten Experiments fest. Die gute Auflösung der kalorimetrischen Energiemessung mit dem Fluoreszenzdetektor wird genutzt, um den Oberflächendetektor mit Ereignissen zu kalibrieren, die von beiden Detektoren gemessen wurden. Anstatt die gesamte Apertur auf einmal zu beleuchten, werden für die neue Technik viele Messungen mit einer kleineren Lichtquelle an unterschiedlichen Positionen in der Apertur kombiniert. Simulationen wurden durchgeführt, um die optimale Verteilung der Positionen

zu finden und die systematischen Unsicherheiten abzuschätzen. In drei Messkampagnen wurden an sieben Teleskopen XY-Scanner installiert und Testmessungen durchgeführt. Zwischen den Messkampagnen ändern sich die optischen Eigenschaften der Teleskope durch die Anlagerung von Staub auf optischen Komponenten. Dies wurde durch die Reinigung eines Spiegels überprüft. Schließlich wurde aus den Messungen die relative Energiekalibrierung der Teleskope ermittelt. Die relativen Unterschiede liegen innerhalb von $\pm 5\%$. Für die HEAT-Teleskope beträgt die Kalibrierung relativ zu Coihueco $0,75 \pm 0,05$. Die Reproduzierbarkeit der neuen Kalibrierungsmethode liegt innerhalb von $0,5\%$ und ist somit gut geeignet, die bisherige Kalibrierungsmethode zu ersetzen.

Contents

1	Introduction	1
2	Ultrahigh-energy Cosmic Rays and the Pierre Auger Observatory	3
2.1	Ultrahigh-energy Cosmic Rays	4
2.2	The Pierre Auger Observatory	11
2.3	AugerPrime	23
3	Extended Uptime of Fluorescence Telescopes	25
3.1	The Duty Cycle of FD	26
3.2	Simulation Study at Reduced Gain	28
3.3	Test Measurements	34
3.4	Calibration	36
4	A new Method to Calibrate Fluorescence Telescopes	39
4.1	The Light Source	40
4.2	The Scanner	47
5	First Results from the XY-Scanner	49
5.1	Analysis	50
5.2	Optimal Grid for Calibration	57
5.3	Reproducibility	63
5.4	Isotropy of the Light Source	68

5.5	Relative Calibration of Telescopes	71
6	Summary and Outlook	75
	Acronyms	77
A	Logbook	79
A.1	XY-Scanner	79
A.2	Extended Uptime	91
B	Hardware Details of the XY-Scanner	93
B.1	Size of the Scannable Aperture	93
B.2	Electronics	93
B.3	Czech Sphere Angular Positions	93
B.4	Minor Hardware Parts	94
C	FD trigger threshold in low gain simulations	99
C.1	Introduction	99
C.2	Threshold simulation	99
C.3	How to use it	101
C.4	Summary	102
	Acknowledgments	103
	Bibliography	105

CHAPTER

1

Introduction

Cosmic rays are fully ionized atomic nuclei which continuously hit our atmosphere from outer space. At low energies ($\lesssim 1 \times 10^{15}$ eV) the energy and mass of those particles can be directly measured with balloon and satellite experiments. Due to the steeply falling spectrum of cosmic rays, their rate is too low for a direct measurement at high energies and therefore large-area experiments at the ground have to take over. These detectors measure air showers that are initiated by high-energy cosmic rays interacting with the atmosphere. The properties of the primary particle (energy, mass, and arrival direction) need then to be inferred from air shower observables, such as the arrival times and the densities of particles at ground or from the fluorescence light emitted along the shower in the atmosphere. A good knowledge of the energy and mass of the primary particles is needed to discriminate between different models for the acceleration and transport of cosmic rays. The arrival directions of the cosmic rays can be used to search for the astrophysical objects which are their sources. However, due to deflection in Galactic and extragalactic magnetic fields, the cosmic-ray flux is near-isotropic over most of the energy range of the cosmic-ray spectrum. Only at the highest energies, it might be possible to identify structures in the arrival directions and especially if at these energies the composition of the cosmic rays includes protons, they are expected to point back to their sources.

The composition of cosmic rays at the Pierre Auger Observatory is currently mainly analyzed with Fluorescence Detector (FD) data, using the depth of the shower maximum (X_{\max}) observed directly with FD. X_{\max} is the most precise indicator of the primary mass of cosmic rays. However, the FD operates only during clear, moonless nights, leading to a duty cycle for data taking of only 15%. This low duty cycle reduces the number of detected events that can be detected by the FD per year, and thus the maximum energy accessible for composition studies with reasonable statistics, since the flux of cosmic rays at ultra-high energies is very low due to the feature in the cosmic-ray spectrum known as flux suppression (see Section 2.1). As part of the upgrade of the Pierre Auger Observatory, a scintillator is added to each Surface Detector (SD) station. The different response of the scintillator and the current water-Cherenkov detector to the electromagnetic and muonic components of an air shower also allow to discriminate between different primary particles. The expected mass sensitivity, however, is worse than that of the FD. With the remaining years of measurement

time until the potential end of the Pierre Auger Observatory in 2030, the estimated number of additional events recorded with the FD will not be enough to extend the range of the X_{\max} measurements with the FD far to higher energies. To get more events in the remaining lifetime of the experiment the duty cycle of the FD has to be extended, which is part of the upgrade. Planned is an increase of the duty cycle by 50%. To realize such an increase the measurements have to be extended into periods with a higher background light flux. In this work, a detailed end-to-end simulation study on the amount of additional events that can be expected from the extended duty cycle measurements and their quality is presented. Furthermore, new FD measurements during high night-sky background were performed on-site at the Observatory to check these simulations and to test the performance of the detector at low gain. The results of the simulations and measurements are presented in Chapter 3.

The second part of this thesis covers the absolute calibration of the FD of the Pierre Auger Observatory. The telescopes have hitherto been calibrated with the “drum”, an unwieldy light source with a diameter of 2.4 m large enough to cover the aperture of the telescopes. The absolute calibration of the FD is of utmost importance to the Pierre Auger Observatory, as it sets the energy scale for the whole experiment. The energy measurements of the FD are used to cross-calibrate the SD with events detected by both detectors. Thus the calorimetric and model-independent energy scale of the FD can be transferred to the SD, which has a duty cycle of $\sim 100\%$. The most recent drum calibration was performed six years ago and the absolute calibration with the “drum method” is effectively discontinued at the time of writing. A replacement is urgently needed. In Chapter 4 a new method for the end-to-end calibration of large-aperture instruments is explained. The main idea is to go from one simultaneous measurement of the whole aperture to many measurements on the aperture with a smaller light source. This method is called the “XY-Scanner”. The sum of all measurements is expected to yield the same results as obtained with the drum. At the same time, the handling of the XY-Scanner and the calibration of the light source is much easier than for the drum.

In Chapter 5 simulations and first results of the XY-Scanner are presented. The best grid of positions, to reproduce the drum results precisely enough and at the same time keep the measurements short, is investigated. Furthermore, the results from the first measurements in the field are presented and the data from three measurement campaigns are analyzed. The results include the reproducibility and measurements of the optical properties of the telescopes. Furthermore, as a first application of the new calibration device to determine and improve the Auger energy scale, the relative difference of the calibration of seven telescopes is measured.

CHAPTER

2

Ultrahigh-energy Cosmic Rays and the Pierre Auger Observatory

Contents

2.1 Ultrahigh-energy Cosmic Rays	4
2.1.1 Extended Air Showers	4
2.1.2 Spectrum	6
2.1.3 Composition	8
2.1.4 Sources	8
2.2 The Pierre Auger Observatory	11
2.2.1 The Fluorescence Detector	12
2.2.2 Calibration of the Fluorescence Detector	17
2.2.3 The Surface Detector	19
2.2.4 AERA	21
2.2.5 AMIGA	22
2.2.6 Atmospheric Monitoring	22
2.3 AugerPrime	23
2.3.1 The Surface Detector	24
2.3.2 The Fluorescence Detector	24
2.3.3 The Radio Detector	24

In this chapter, a general introduction to the field of cosmic-ray research is given. The status of current research on ultrahigh-energy cosmic rays (UHECRs) will be summarized and experimental techniques to detect air showers are explained at the example of the Pierre Auger Observatory. At the end of this chapter, the upgrade of the Pierre Auger Observatory is presented.

2.1 Ultrahigh-energy Cosmic Rays

Soon after the discovery of radioactivity, Victor Hess took electroscopes on balloon flights [1], to measure the height-dependence of the discharge of electroscopes caused by radiation. Contrary to the belief at that time, he did not only find a decline in radiation with increasing height, but an increase of radiation above 1 km above ground. This should not have been the case if the source of all radiation had been radioactive elements in the crust of the Earth. Therefore he concluded, that there must be an additional source of radiation coming from above. This radiation was later coined cosmic rays by Millikan [2].

Another important discovery was made by Pierre Auger in 1938 [3]. From coincidence measurements with particle detectors on the “Jungfraujoch”¹, he concluded that the cosmic rays induce particle showers in the atmosphere. The coincidence rate was higher when the detectors were closer to each other. For random coincidences, the rate should have been constant, independent of the distance between the detectors. Therefore the arriving particles had to be correlated.

The term ultrahigh-energy cosmic rays stands for cosmic rays with an energy exceeding 1×10^{18} eV, which is the main region of interest of the Pierre Auger Observatory. Today, the term cosmic rays stands only for the charged particles arriving at earth, photons and neutrinos are usually treated separately. In the context of an air shower, the cosmic ray particle is called the primary particle.

2.1.1 Extended Air Showers

For the detection of cosmic rays two fundamental approaches exist. At lower energies² cosmic rays can be directly detected [5]. As the cosmic rays interact with the atmosphere these measurements have to be done above, or at least high up in the atmosphere. The detectors for these experiments need therefore be onboard of high-altitude balloons or satellites. These detectors work very much like the detectors used in high energy physics, with multiple instrumented layers to discriminate between different primary particles. Current examples are the PAMELA experiment [6] and AMS-02 [7].

As visible in Fig. 2.1, the flux of cosmic rays falls steeply with energy. The flux of cosmic rays in particles per area is also indicated at the features of the spectrum. This limits the direct detection method as larger detectors would be needed to get a sufficient amount of events. Bigger detectors would be both technically challenging and very expensive in space, therefore large-area experiments at the ground have to take over. The primary particles interact with the atmosphere and induce a particle shower. Secondary particles can then be detected at ground, the properties of the primary particles, however, have to be reconstructed from air shower properties. The different detection techniques, as far as they are used in the Pierre Auger Observatory, will be explained in Section 2.2.

As shown in Fig. 2.2, an air shower consists of three groups of particles, the electromagnetic, muonic and hadronic component. The simplest model for the development of an air shower is the Heitler model [9]. In this model, only electromagnetic particles are considered. In each interaction, the energy is split equally on the two daughter particles. The distance between two interactions is the distance in which a particle loses half its energy by radiative losses, or $\lambda_r \times \ln 2$, with $\lambda_r \approx 36.6 \text{ g cm}^{-2}$ being the radiation length in air [10]. This continues until the critical energy $E_c = 85 \text{ MeV}$, from where on collision energy losses are larger than

¹ in the Swiss Alps at 3.4 km above sea level ² typically below 1×10^{15} eV

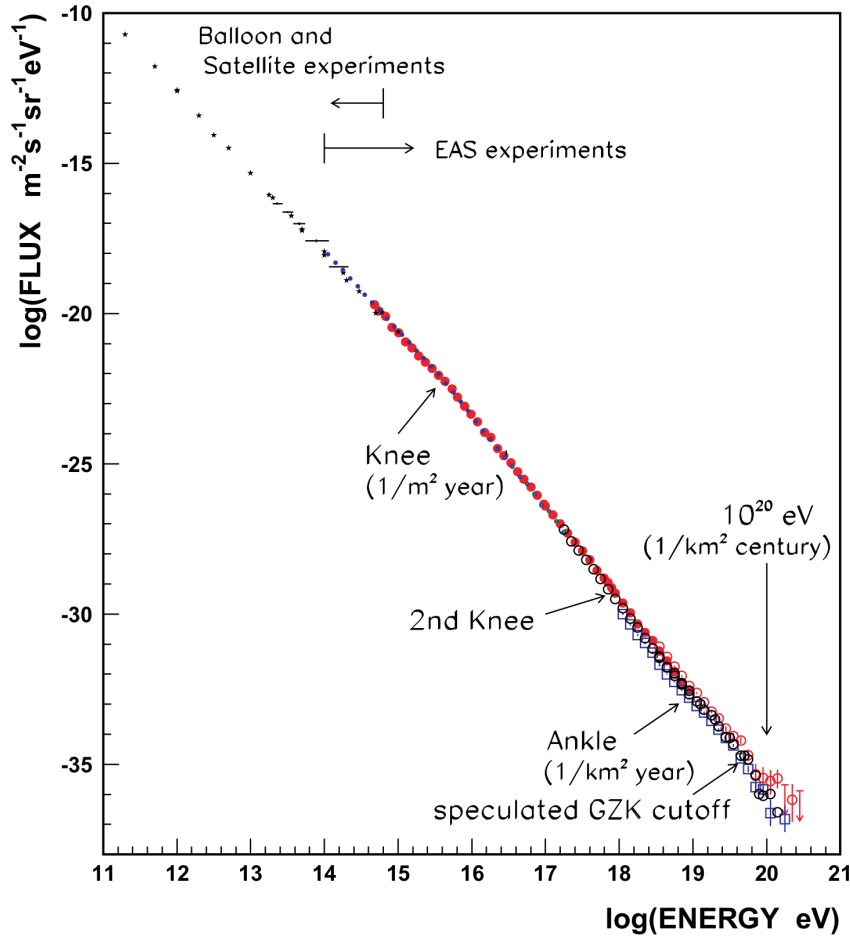


Figure 2.1: Spectrum of cosmic rays over the whole energy range from 1×10^{11} to 1×10^{21} eV [4].

radiative losses and no new particles are produced. There, the shower maximum is reached. The depth of the shower maximum, the mass along the path in the atmosphere in g cm^{-2} , is called X_{max}

$$X_{\text{max}}^{\gamma} = \lambda_r \times \ln \left(\frac{E_0}{E_c} \right). \quad (2.1)$$

The depth of the shower maximum thus grows logarithmically with energy. However, purely electromagnetic showers are only valid when the primary particle is a photon or an electron/positron.

This simple model can be generalized for hadronic primaries [11]. In each interaction, pions are produced in equal numbers and there are twice as many charged (N_{Ch}) as neutral pions generated in each interaction. The neutral pions promptly decay into photons starting an electromagnetic shower. The charged pions undergo further interactions until the critical energy $E_c^{\pi} = 20 \text{ GeV}$ is reached, where the decay length becomes shorter than the interaction length. As an estimate for the depth of the shower maximum, it is enough to calculate the electromagnetic cascade from the first interaction. From each neutral pion a electromagnetic shower with energy $E_{\gamma} = \frac{E_0}{3N_{\text{Ch}}}$ develops, as the initial energy is distributed over $\frac{3}{2}N_{\text{Ch}}$ pions

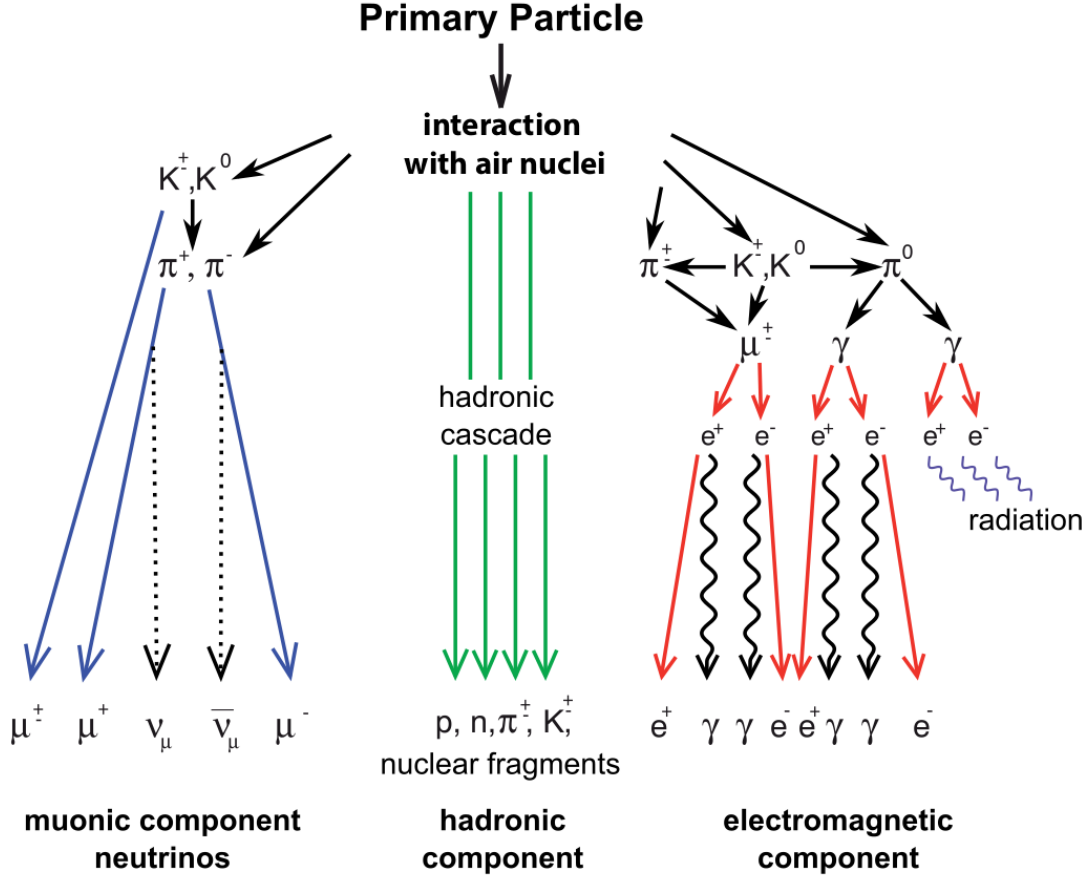


Figure 2.2: Schematic picture of an air shower with the three main components [8]. Most of the energy is in the electromagnetic component, followed by the muonic component and a small fraction of hadrons.

with two photons per neutral pion. Using E_γ in Eq. (2.1), the depth of the shower maximum for a proton shower is then

$$X_{\max}(1) = X_0 + \lambda_r \times \ln\left(\frac{E_0}{3N_{\text{Ch}}E_c}\right) = X_{\max}^\gamma + X_0 - \lambda_r \times \ln(3N_{\text{Ch}}), \quad (2.2)$$

where X_0 denotes the depth of the first interaction. A primary cosmic-ray with mass number A then produces A air showers with energy $E = \frac{E_0}{A}$, generalizing Eq. (2.2) to:

$$X_{\max}(A) = X_{\max}(1) - \lambda_r \times \ln(A). \quad (2.3)$$

For a proper treatment of fluctuations and for including all relevant elementary particles Monte Carlo simulations are used. The program of choice for these simulations is the CORSIKA framework [12]. To model the hadronic interactions, different models can be selected.

2.1.2 Spectrum

An important measurement in cosmic-ray physics is the spectrum or flux of cosmic rays. The spectrum follows a power law in energy with several breakpoints, for the resemblance

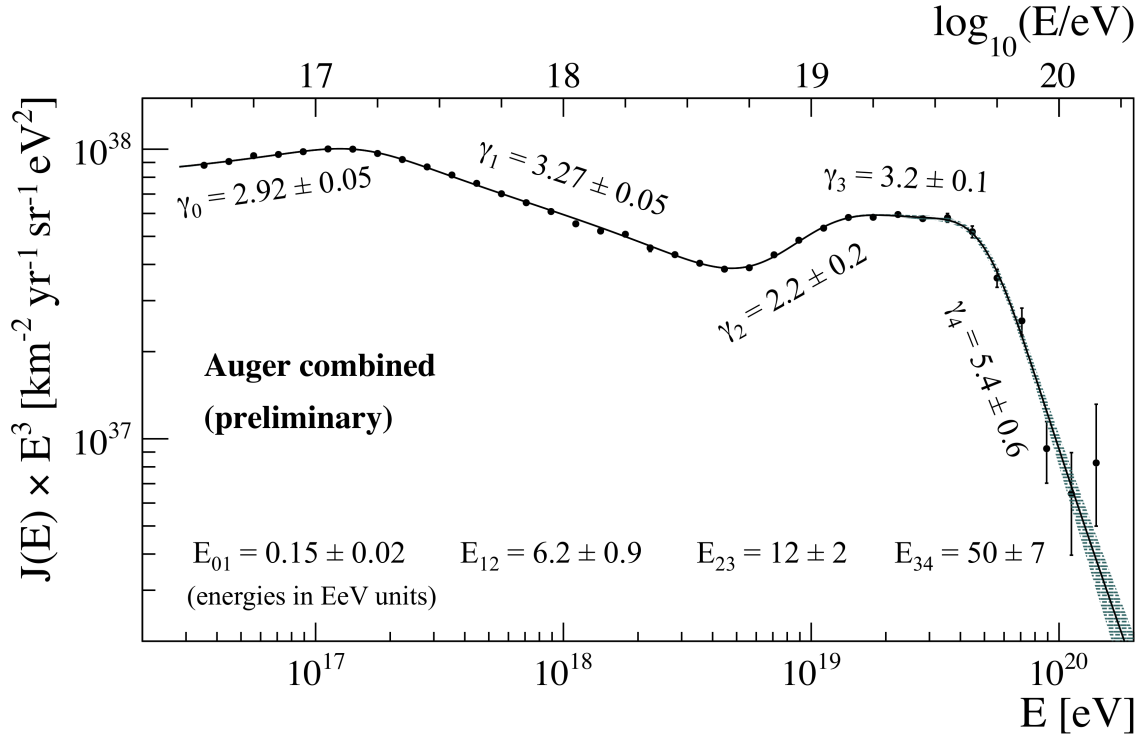


Figure 2.3: Spectrum of ultrahigh-energy cosmic rays measured by the Auger collaboration scaled with E^3 , clearly showing the “second knee” and the “ankle” feature [13].

with a leg they are called “knee” and “ankle”. At the highest energies, there is a suppression region, where the spectrum drops steeply. The latest result by the Pierre Auger Observatory is shown in Fig. 2.3, the “second knee”, the ankle and the suppression region are visible in the studied energy range. Compared to Fig. 2.1 the cosmic-ray flux has been scaled with E^3 , to better visualize the features. Since the ICRC 2019 the Pierre Auger Collaboration uses an additional breakpoint in the spectrum between the ankle and the suppression region to better describe the shape. Usually, cosmic-ray experiments are designed for a certain energy range. One example of an experiment in the knee region is the KASCADE experiment [14]. The Pierre Auger Observatory and its counterpart in the Northern hemisphere, the Telescope Array (TA) experiment [15], were designed to cover the ankle and the suppression region.

The features of the cosmic ray spectrum can be explained by properties of the sources or by propagational effects [16]. As an example, the suppression region is discussed here. This might be caused by the Greisen–Zatsepin–Kuzmin (GZK) effect [17] [18], where cosmic-ray protons interact with photons from the cosmic microwave background (CMB). They form a Δ^+ baryon which then decays into a nucleon and a pion.



This process repeats until the proton energy is below the threshold energy of this process of 5×10^{19} eV. As a result, the sources of cosmic rays observed at earth which are above this energy have to be within the GZK - horizon of ~ 100 Mpc. The giant dipole resonance has a similar effect on higher-mass cosmic rays and leads to the photodisintegration of nuclei. Alternatively, the suppression region would signify the maximum energy of the cosmic ray

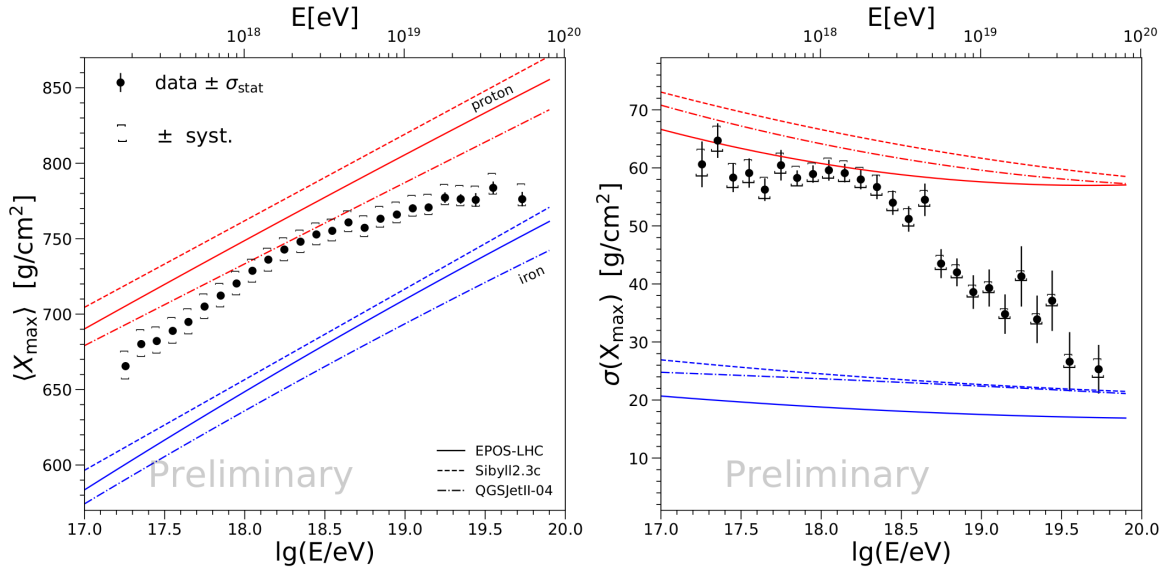


Figure 2.4: Mean (left) and standard deviation (right) of the X_{\max} distribution as a function of energy from data of the Pierre Auger Observatory. For comparison the lines show the results for pure proton and iron simulations for different interaction models [20].

sources. To discriminate between cosmic-ray sources and transportation models additional information is needed. While both ways of explaining the features can produce the same shape of the spectrum, they usually make different predictions on the composition of cosmic rays.

The energy range from 1×10^{17} eV to 1×10^{19} eV is called the transition region. There, the transition from galactic to extragalactic sources is expected to happen [19].

2.1.3 Composition

The mass of a cosmic ray primary can only be inferred indirectly from air shower measurements. One way is to reconstruct the depth of the shower maximum X_{\max} , which, as has been shown above (Eq. (2.3)), depends logarithmically on the primary mass. At the Pierre Auger Observatory, X_{\max} can be measured with the FD [21], which records the longitudinal development of air showers. The average mass of cosmic-ray particles can be inferred by comparing the moments of the measured X_{\max} distribution to simulations with different primaries. The latest results for the X_{\max} analysis by the Pierre Auger Observatory can be found in Fig. 2.4. As can be seen at $\sim 10^{18.3}$ eV, there is a break in the X_{\max} moments, going from a light composition to a gradually heavier one.

Further insights in the fraction of individual mass groups (p, He, N, Fe) can be obtained by template fits [23]. The results of the Pierre Auger Collaboration can be found in Fig. 2.5 and show the same trend towards a heavier composition for all hadronic-interaction models.

2.1.4 Sources

The identification of the sources of the cosmic rays is still an unsolved problem. The candidates have to meet two conditions: the necessary conditions for the acceleration of cosmic

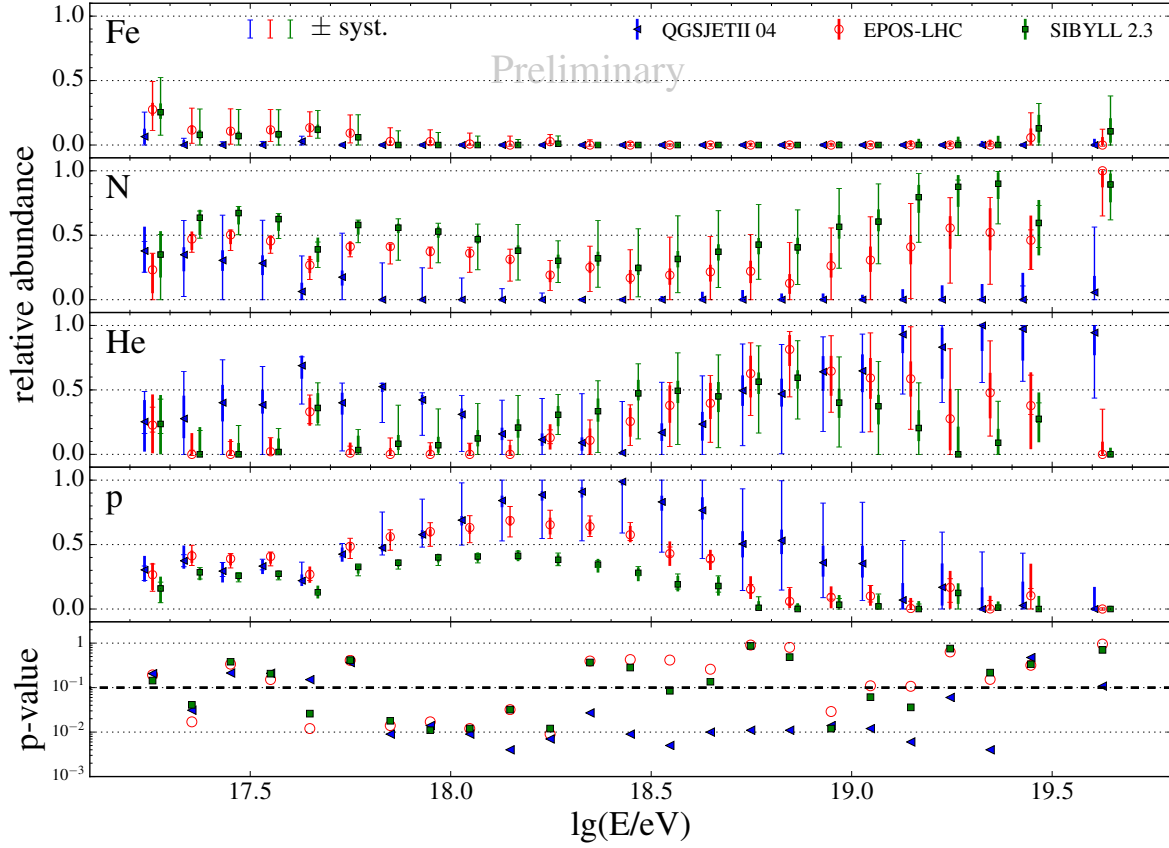


Figure 2.5: Cosmic ray composition obtained from template fits to the X_{\max} spectrum for different interaction models [22].

rays and the size and strength of magnetic fields to contain them in the accelerator. The basic mechanism has been established by Fermi [24]. Particles get reflected on moving magnetic clouds and gain energy in each reflection. Higher energies are achieved many repetitions of this process. Depending on the geometry a first and a second-order process exist. The second-order process is on magnetic clouds and the energy gain per cycle is proportional to β^2 , where β is the velocity of the magnetic cloud in units of the speed of light. The first order process happens in shock waves and is proportional to β [25], therefore more efficient.

In the search for possible sources for UHECR, the Hillas criterion [27] is used. It is based on the purely geometrical consideration, that particles have to be contained in the acceleration region. This containment is realized by deflection on magnetic fields, the source has, therefore, to be bigger than twice the Larmor radius of the particles. The acceleration is constrained by the lifetime of the astrophysical object, thus the velocity of the shock front β has to be taken into account, the Hillas criterion results in:

$$E_{\max} = qBL\beta, \quad (2.5)$$

here, B is the strength of the magnetic field and L the size of the source region. For a classification of possible sources in this way see Fig. 2.6. This can however only be used to exclude sources from being the dominant source of cosmic rays at the highest energies, for a confirmation direct detection is needed.

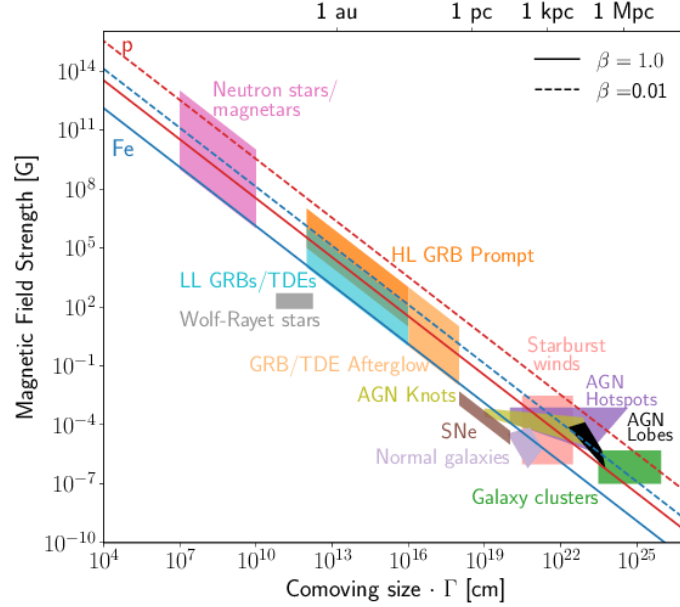


Figure 2.6: Hillas Plot [26] based on [27]. Sources are plotted by their size and magnetic field strength. The lines show the requirements to accelerate proton and iron to $E = 10^{20}$ eV depending on the shock front velocity.

Anisotropy Searches

At lower energies, the cosmic ray flux is mainly isotropic because of deflections on the turbulent magnetic fields in our galaxy. Only structures of order 1×10^{-3} and smaller have been found, for example by the HAWK³ and IceCube collaborations in the TeV range [28][29]. The expectation is, that at the highest energies the deflection on magnetic fields becomes small and sources appear as clusters of events on the sky map. A non zero fraction of protons at the highest energies would help the discovery of cosmic ray sources as protons are deflected the least. So far a large-scale dipolar anisotropy with an amplitude of 6.5% above 8 EeV was found in the data of the Pierre Auger Observatory [30]. It does not point in the direction of the galactic center, this is the first direct evidence that UHECRs are of extragalactic origin. On intermediate scales, indication for a correlation of the arrival direction of cosmic rays with the distribution of nearby starburst galaxies was found above 39 EeV [31]. TA reports a cluster of events above 57 EeV [32].

Additional information on the sources of UHECRs can be obtained in multi-messenger studies. In interactions with the matter surrounding the cosmic-ray sources, neutrinos and gamma rays are produced. As those are neutral particles, they would directly point back to their sources. A diffuse background comes from pions produced in the GZK effect, see Eq. (2.4), which also decay into photons and neutrinos.

$$\begin{aligned} \pi^0 &\rightarrow \gamma\gamma \\ \pi^+ &\rightarrow \mu^+ + \nu_\mu \rightarrow e^+ + \nu_e + \bar{\nu}_\mu + \nu_\mu \end{aligned} \quad (2.6)$$

These neutral messengers can be searched for in the data of cosmic-ray observatories [33], or in combination with dedicated experiments for those particles [34] [35].

³ High-Altitude Water Cherenkov Observatory



Figure 2.7: Photo of an SD station with an FD building in the background [36].

2.2 The Pierre Auger Observatory

The Pierre Auger Observatory [37] was founded in 1999 and is a hybrid detector for the study of cosmic rays at the highest energies with high statistics. It was built in western Argentina, close to the city of Malargüe. The two main detectors are the Surface Detector (SD), and the Fluorescence Detector (FD). The SD consists of ~ 1650 water-Cherenkov detectors (WCDs) spanning an area of $\sim 3000 \text{ km}^2$. The FD consists of $24 + 3$ fluorescence telescopes distributed over four sites at the border of the SD array. Three additional telescopes are placed at the Coihueco (CO) site as a low energy extension called High Elevation Auger Telescopes (HEAT). A picture can be found in Fig. 2.7 and the layout in Fig. 2.8. This hybrid approach was chosen to combine the advantages of the two detection methods and thus compensate for their shortcomings. The FD measures the longitudinal profile of an air shower and thus provides a calorimetric measurement of the energy with good resolution and minimal theoretical uncertainties. But it can measure only in dark and clear nights and therefore its duty cycle is only $\sim 15\%$ [38]. On the other hand, the SD has a duty cycle of almost 100%, but it measures only the density of particles in an air shower at ground. The correlation of the particle density at ground to the energy of the air shower is obtained by cross-calibration with FD data in hybrid events. In addition, the observatory is equipped with an array of antennas to detect the radio emission of air showers called Auger Engineering Radio Array (AERA) and buried scintillators for the detection of muons called Auger Muon Detectors for the Infill Ground Array (AMIGA).

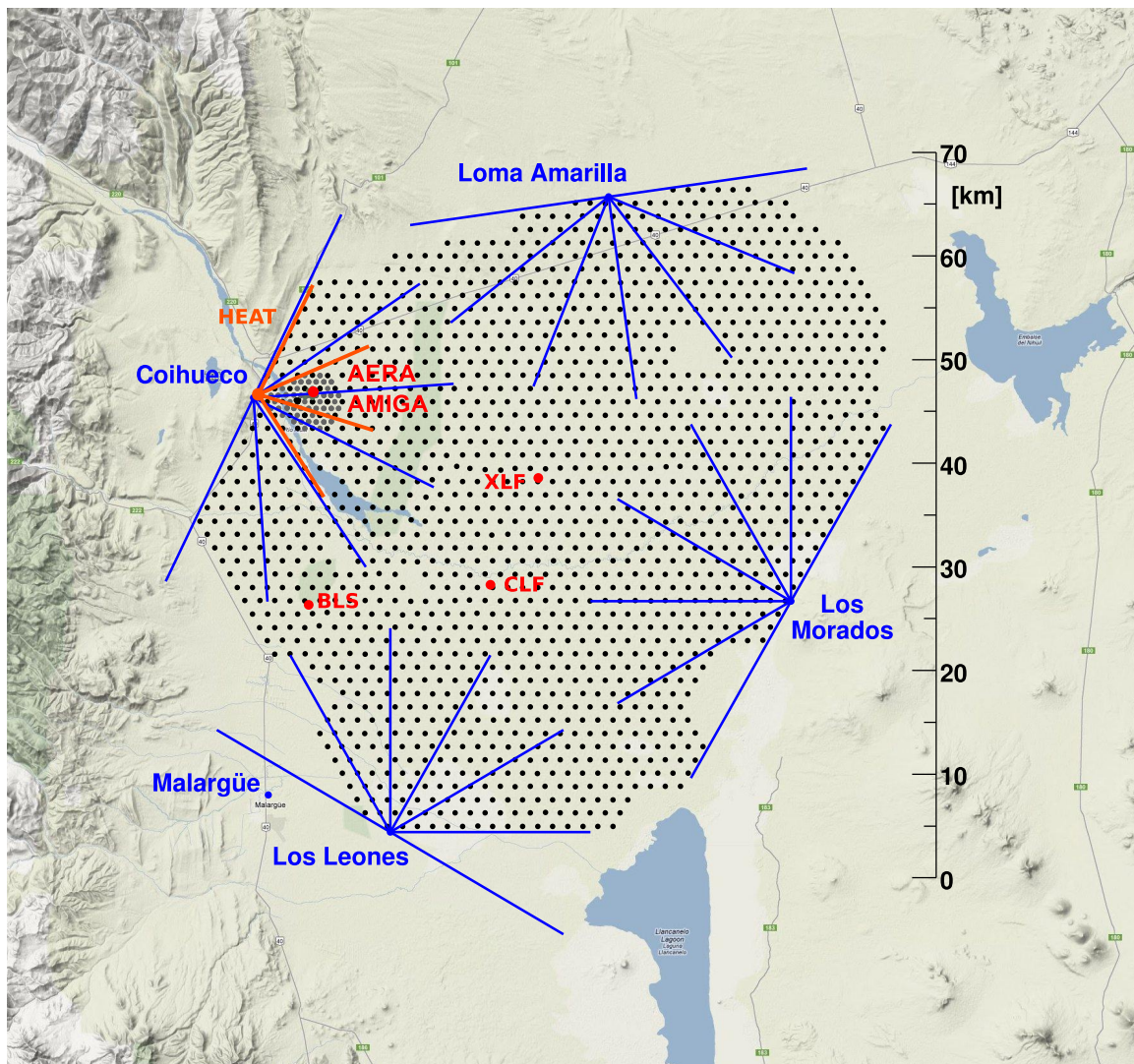


Figure 2.8: Map of the Pierre Auger Observatory. Each SD station is represented by a dot, the colored lines indicate the field of view for the single telescopes. The positions of AERA, AMIGA and the laser facilities are also indicated [36].

2.2.1 The Fluorescence Detector

When the charged particles of an air shower travel through the atmosphere they excite nitrogen molecules. When these molecules deexcitate again they emit photons in the ultraviolet (UV) range. The spectrum of the emission is shown in Fig. 2.12(a). The emission of these photons is isotropic, therefore fluorescence telescopes can detect air showers over a large air volume by observing the showers from the side. The yield of UV photons is proportional to the energy deposit in the air shower. Therefore the longitudinal development of the air shower can be recorded. The integral is proportional to the energy and the depth of the shower maximum (X_{\max}) can be directly observed.

The telescope follows the Schmidt design [40] which allows for a large aperture and field of view (FoV). The camera is located between the aperture and the spherical mirror. A corrector plate in the aperture eliminates the spherical aberration of the mirror. The FoV of one telescopes is $30^\circ \times 30^\circ$. Six telescopes are arranged at each of the four sites, as shown in

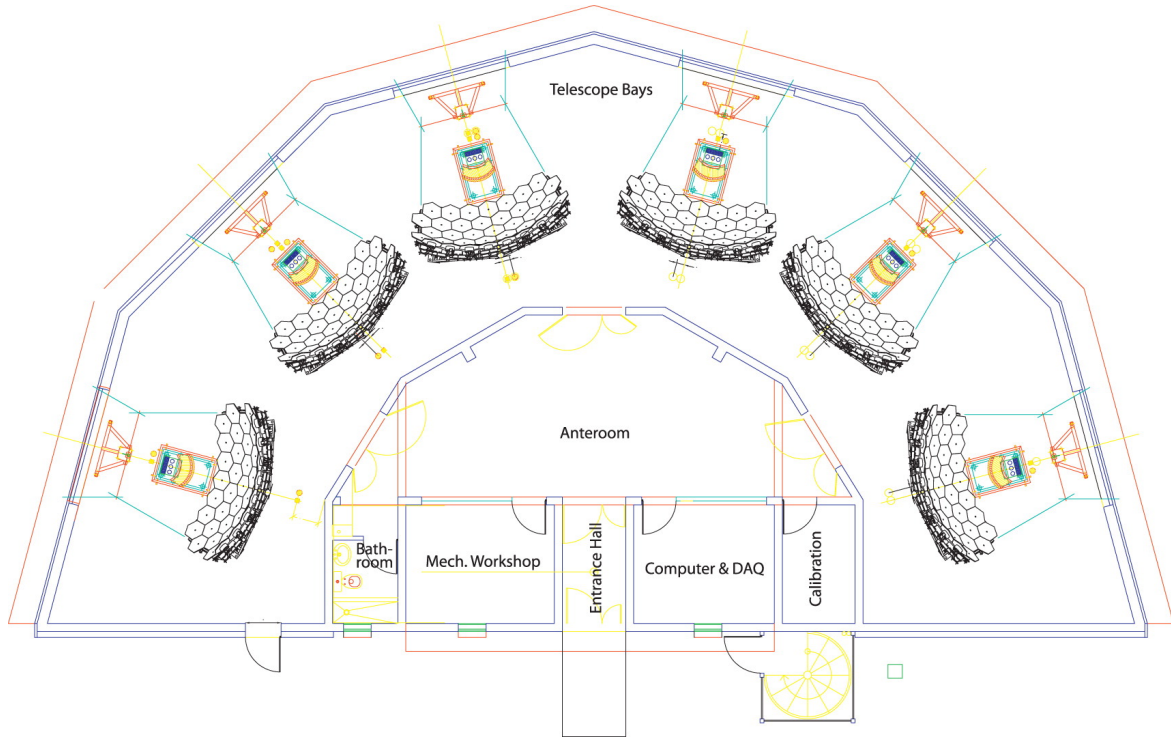


Figure 2.9: Schematic of FD - Building with arrangement of the six telescopes. Numbering goes counterclockwise from one to six in each of the four sites [39].

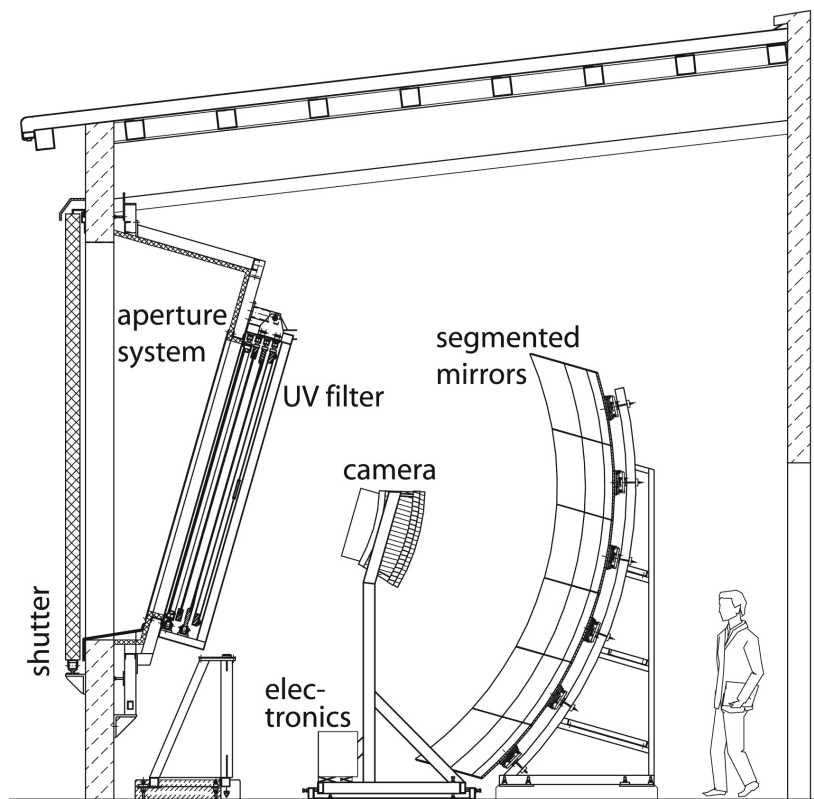


Figure 2.10: Schematic drawing of a fluorescence telescope [39].

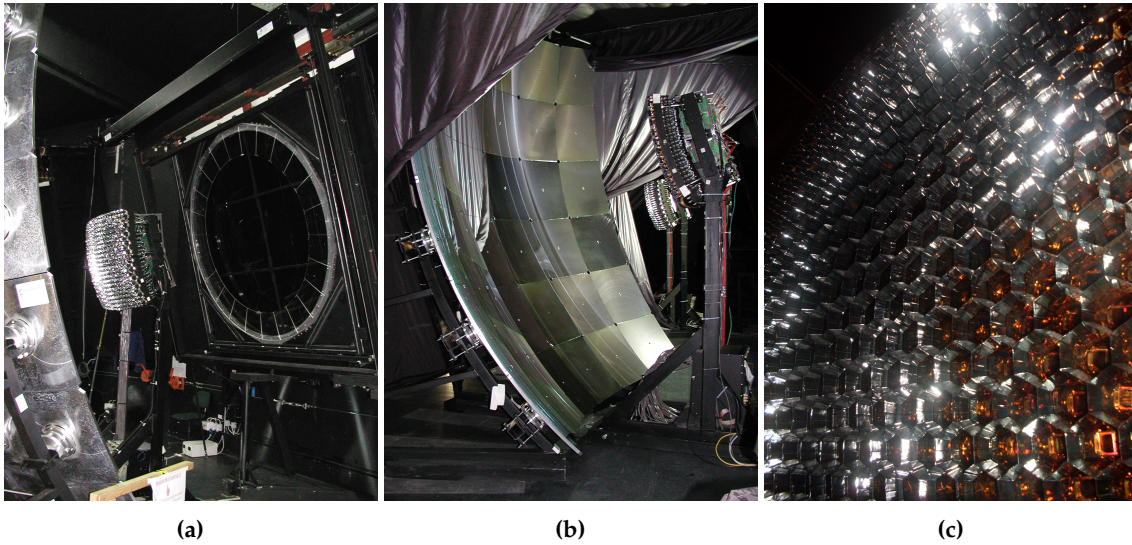


Figure 2.11: Pictures of the optical system of the FD. (a) Camera in front of the Corrector ring and UV filter (b) Mirror and (c) closeup of Camera [36].

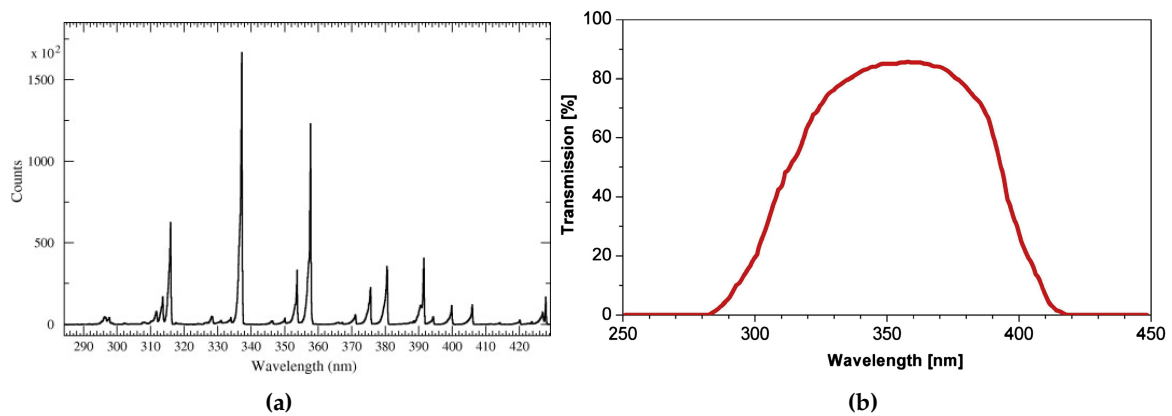


Figure 2.12: (a) Nitrogen fluorescence light emission spectrum [41], (b) Transmission of M-UG-6 glass used for the UV-filters [39]

Fig. 2.9, to obtain a full 180° FoV in azimuth. The bottom border of the FoV is slightly above the horizon. For a schematic drawing of one telescope see Fig. 2.10. The optical components are described in the following. For an in-depth description see [39].

UV Filter

Behind the shutters, which are closed at daytime or when the outside conditions do not allow data taking, are the UV filters. The main purpose is to reduce the amount of background light and block the light outside of the frequency range of the fluorescence light. They are built from Schott M-UG-6 [42] glass. The transmission curve of the filters and the emission spectrum of the fluorescence light can be found in Fig. 2.12. Because of the size of the filter, that needs to cover the full aperture of 3.8 m², it is segmented. An additional benefit of the UV filter is, that it encloses the telescope buildings against the environment at night. There is no direct air exchange with the environment, which minimizes the intake of dust. The

influence of dust on measurements is discussed in Section 5.3.3. A picture of a filter is shown in Fig. 2.11(a).

Corrector ring

Here, the design differs from the classical Schmidt telescope design. Instead of the whole corrector plate, only the outermost part is used as a corrector ring. The corrector ring is placed inside the aperture of the telescope. It was designed to minimize both spherical aberration and production cost, keeping the angular spread below 0.5° [39]. For comparison, the angular acceptance of one pixel of the camera is 1.5° . A picture is shown in Fig. 2.11(a).

Mirror

The spherical mirror of the telescope has an area of $\sim 13 \text{ m}^2$ and consists of multiple segments. Two different designs were used. One consists of 36 quadratic segments milled from aluminum blocks. This design is used for the telescopes at the sites of Los Leones (LL) and Loma Amarilla (LA). The second design uses 60 hexagonal glass segments and is used at the sites of Los Morados (LM) and CO and for the HEAT extension. A picture of a mirror made of quadratic segments is shown in Fig. 2.11(b).

Camera

In a Schmidt telescope design, the focal plane is curved, in this case, the focal plane has a radius of curvature of $\sim 1.7 \text{ m}$. On this surface 440 pixels are arranged in a 22×20 matrix, every second row is indented by half a pixel to form a hexagonal grid [43]. The angular distance between neighboring pixels is 1.5° . Each pixel is a photo-multiplier tube (PMT) with a hexagonal photocathode with 40 mm diameter. In between the PMTs, Winston-cone-like light collectors⁴ are installed. They ensure a high light collection efficiency without gaps between the pixels, as well as a sharp transition in between pixels. A picture is shown in Fig. 2.11(c). Later, many plots will show calibration constants as a function of the channel number. The organization of the PMTs on the 2D camera is shown in Fig. 2.13.

HEAT

The HEAT telescopes [45] are the low-energy extension of the FD of the Pierre Auger Observatory. Three additional telescopes were installed close to the FD site of Coihueco. The important difference to the standard telescopes is that they are tiltable between the standard position and 30° up. Pictures of both orientations are shown in Fig. 2.14. At lower energies, air showers develop higher up in the atmosphere. Below $1 \times 10^{18} \text{ eV}$ the shower maximum is usually outside of the field of view of a standard telescope, as the shower would need to be relatively close to the telescope to pass detection thresholds. By tilting the telescope up by 30° the relevant part of the atmosphere can now be observed closer to the telescope and allows the detection at lower energies. The reduced area in which air showers can be detected in front of the telescope is compensated by the higher flux at lower energies.

HEAT and the 750 m infill of the SD (see Section 2.2.3) were built to extend the detection of UHECR down to an energy of $1 \times 10^{17} \text{ eV}$. This creates an overlap with other experiments

⁴ called *mercedes* because of their three-legged shape

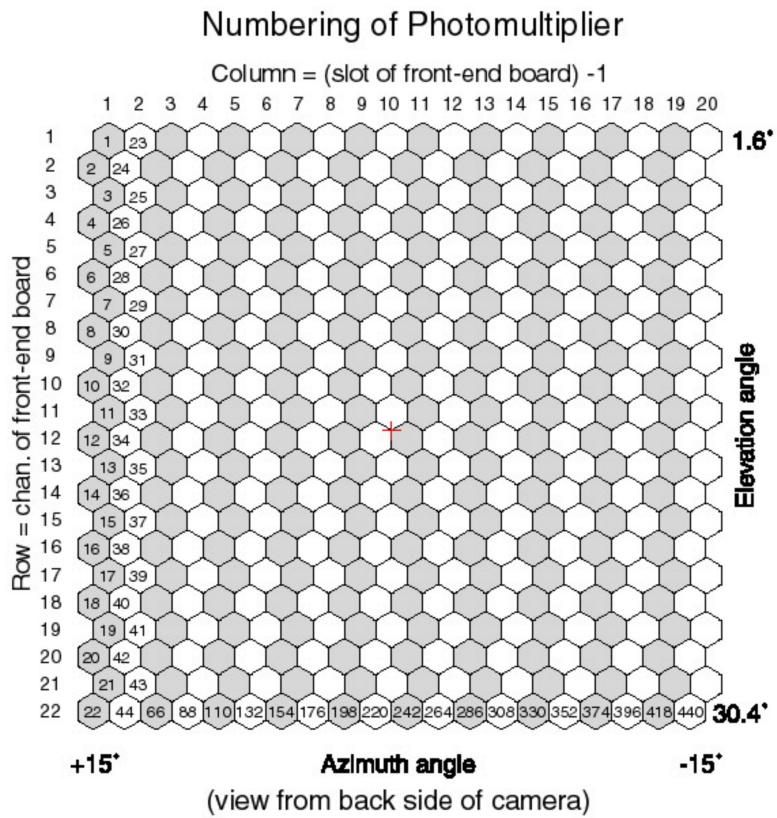


Figure 2.13: Numbering of the PMT on the camera as seen from behind [44].



Figure 2.14: The HEAT telescopes in (a) downward and (b) upward mode [36].

in the transition region, like KASCADE grande, Tunka, and IceTop, which can be used to compare the results.

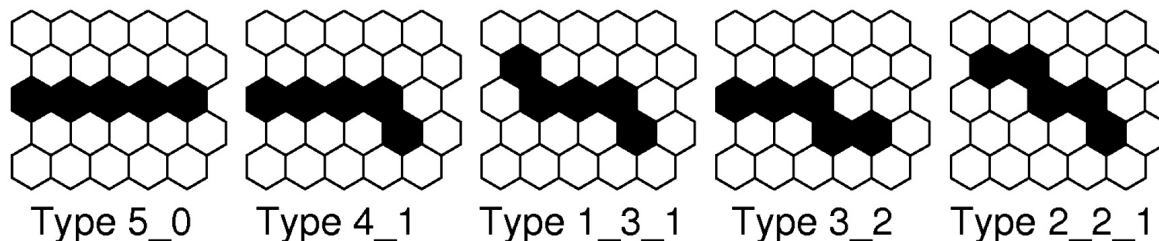


Figure 2.15: Fundamental track patterns on a hexagonal grid for the SLT [39], all other five pixel long tracks can be obtained by mirroring and rotation.

Triggers

The trigger of the FD is split in three levels called first level trigger (FLT), second level trigger (SLT) and third level trigger (TLT). The FLT is on the single PMT level. It is a signal over baseline trigger where the threshold is adjusted such, that the single-pixel trigger rate is 100 Hz. This results in on average four randomly triggered pixels per event. The SLT checks for geometrical patterns, as air showers are expected to leave a track in the camera. The five-pixel patterns that are used are shown in Fig. 2.15. If four out of five pixels in a pattern can be matched to the FLTs, the second level is passed. The TLT then checks the timing structure inside the pattern. This catches 99 % of all lightning and random triggers. FLT to TLT are performed on the telescope level. After the TLT the data from all triggered telescopes of a site is combined. On the combined data a hybrid trigger, called T3, is run, which performs a preliminary reconstruction of the event. The T3 is then used as an external trigger to the SD, to read out the SD stations closest to the building [39].

2.2.2 Calibration of the Fluorescence Detector

The calibration of the FD sets the energy scale for the whole experiment. The detection of fluorescence light from air showers is a calorimetric measurement. The energy is proportional to the integral of the longitudinal profile, and the proportional factor is the fluorescence yield which can be measured in the laboratory [41]. The FD energy is then used to cross-calibrate the SD array, see Section 2.2.3.

The calibration of the FD is split into two systems. The absolute calibration with a well-understood light source, which is done in regular time intervals, and a relative calibration system to track the change in between the absolute calibration runs. The absolute calibration light source is called “the drum”. For the relative calibration three light sources are mounted at every telescope, Calibration A (Cal A), Calibration B (Cal B), and Calibration C (Cal C).

The Drum

The drum [46] is a 2.5 m diameter cylinder that can be mounted onto the aperture of the fluorescence telescopes, see Fig. 2.16(a). The insides are lined with Tyvek which is diffusively reflecting, the window towards the drum is a thin Teflon sheet which is diffusively transmitting. A 375 nm light-emitting diode (LED) is used as a lightsource. The light source is mounted in the center of the drum on the side facing the telescope. It is inside a reflec-

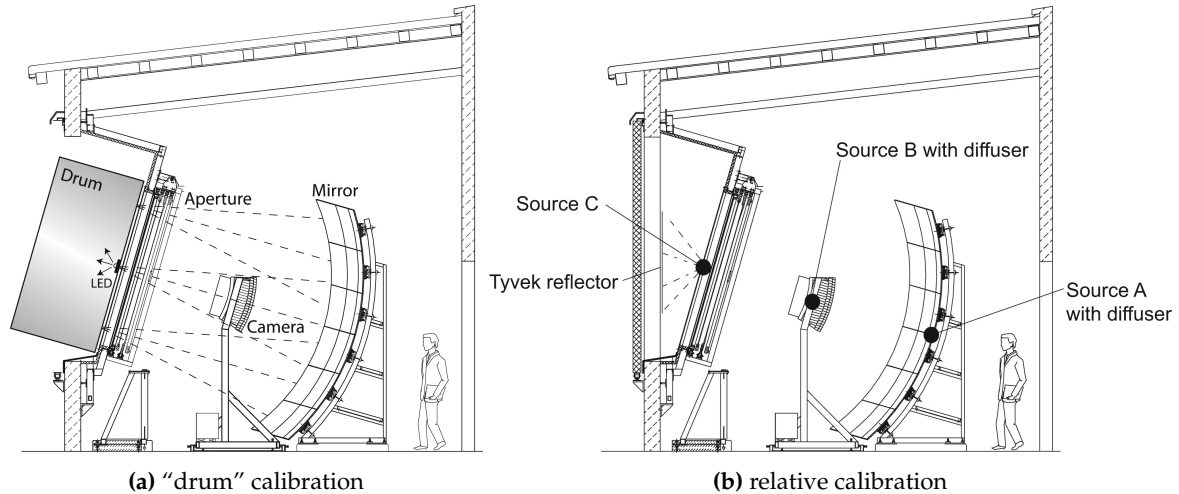


Figure 2.16: Schematic drawings for the (a) drum and the (b) relative calibration. The positions for the three light sources (Cal A, Cal B and Cal C) are indicated [39].

tor which prevents direct light to be emitted into the telescope. The result is a Lambertian emitter. A light source is Lambertian if the intensity decreases with $\cos \theta$:

$$I(\theta) \sim \cos \theta, \quad (2.7)$$

where θ is the angle to the surface normal. As the apparent area of the light source has the same cosine dependence, the radiance is independent of θ and the light source appears to have the same brightness in any direction. The uniformity and the calibration of the drum are measured in a laboratory at the central campus of the Observatory. With this method, it is possible to calibrate two telescopes per night. Originally, it was planned to be done on a yearly schedule, but due to the high amount of work needed it was done less often.

It is also possible to check the detection efficiency of the telescope depending on the wavelength of the incoming photons. For this purpose, the LED was replaced by a xenon flasher behind a filter wheel, the light was guided into the drum with a tube [47].

Relative Calibration

To keep track of the change in calibration in between the drum calibration run the light sources of the relative calibration system are used [48]. Originally the relative calibration was performed at the beginning and the end of each night. Calibration A uses a 470 nm LED One LED Calibration Unit (LCU) is installed per FD building, from there, the light is guided to the telescopes through optical fibers. A diffuser is located in the center of the mirror pointing directly to the camera. As the gain of the PMTs is drifting throughout a night, intermediate calibration runs were implemented. For an analysis of these calibration runs see [49].

The Cal B and Cal C lightsources use xenon flasher lamps with different filter wheels. The Calibration B diffuser is mounted at the sides of the camera pointing towards the mirror. The filter wheels allow testing of the linearity of the PMT response. The Calibration C light source is outside of the UV filters pointing outwards. On the inside of the shutter are Tyvek patches to reflect the light into the telescope. A wheel with interference filters allows multi-wavelength studies [39].

These three relative calibration light sources could thus be used to monitor different parts of the optical system: Cal A the camera, Cal B the mirror and the camera, and Cal C the whole telescope. However, the measurements with Cal B and Cal C produced unreliable and inconclusive results. Cal B illuminates a too-small area of the mirror, and Cal C depends heavily on the state of the Tyvec reflectors on the inside of the shutters [50]. Thus only Cal A is used for the relative calibration of the FD.

2.2.3 The Surface Detector

The other main detector of the Pierre Auger Observatory is the Surface Detector. It consists of a hexagonal grid of particle detectors distributed over a large area. The detectors do not have to cover the whole area, knowledge of the signal at some points is enough to reconstruct the particle density distribution. Different to the fluorescence detection method the longitudinal development of the air shower can not be observed, only a snapshot of it can be recorded at ground level. The relation of this snapshot to the shower energy depends on geometry and compositions. It can be calibrated with simulations or hybrid measurements.

The original SD array [51] consists of 1600 stations on a 1500 m distance hexagonal grid, covering 3000 km². The layout is shown in Fig. 2.8. Each station is a water-Cherenkov detector (WCD). The water-Cherenkov technique was chosen for its robustness and low cost. Another advantage is the rather uniform projected area up to high zenith angles. This is not given for scintillators, which are used by the other large cosmic-ray experiment TA [15]. An altitude between 1000–1500 m above sea level was found to be optimal to be close to the depth of the shower maximum, to minimize the effect shower-to-shower fluctuations have on the measurements. A flat surface is needed for communication.

The SD 1500 m grid reaches full sensitivity at $E = 10^{18.5}$ eV [51]. To lower this threshold down to $\sim 10^{17}$ eV a 750 m [52] and a 433 m [53] sub-array were built close to the FD site of Coihueco. The same detector technology as for the main array was used.

A Surface Detector Station

Each station of the SD is a huge tank of 12 000 l of ultra-pure water which acts as the detection volume. Charged particles which travel through the tank faster than the speed of light in water generate Cherenkov light. The Cherenkov light is then detected by PMTs. The water was purified on the main campus of the Observatory. Around the water, there are two layers of protection. The outer layer is a 13 mm thick polyethylene tank which acts as protection against the environment as well as a light-tight enclosure. The water is inside a flexible liner, the innermost layer is made from Tyvek which is reflective for UV photons. Above the water level, three 9-inch diameter PMTs are mounted over windows in the liner [51]. For a schematic drawing see Fig. 2.17 and a photo of an SD station is shown in Fig. 2.7.

As the stations are distributed over a large area they have to be self-sustaining. Power is generated in solar panels and stored in batteries. The data is transferred wirelessly to the main campus.

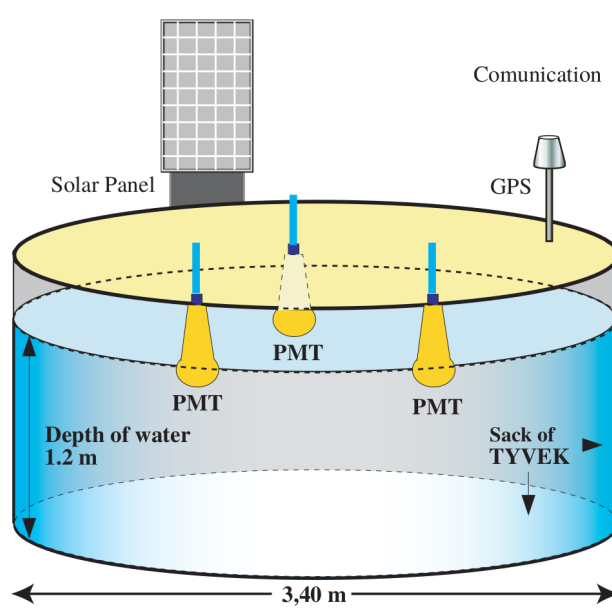


Figure 2.17: Schematic drawing of an SD station [54], three 9 inch diameter PMTs are mounted over windows in the liner.

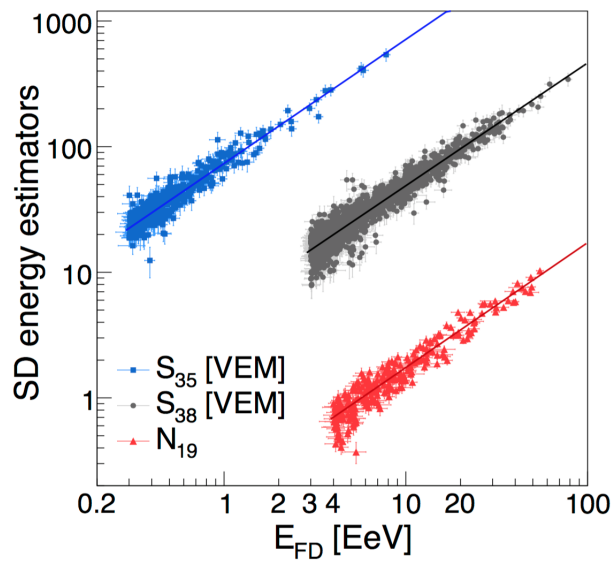


Figure 2.18: SD cross calibration [55]. S_{35} and S_{38} are the energy estimators for the infill and the standard array. For very inclined events a separate energy calibration is needed as the electromagnetic component of an air shower does no longer reach the ground. N_{19} is the energy estimator for inclined events.

Cross-Calibration with FD

The SD measures the density distribution of particles on ground of an air shower, this footprint depends on the geometry and primary particle properties. The distribution of the signal on ground is fitted, the signal at an optimal distance to the shower axis is used as

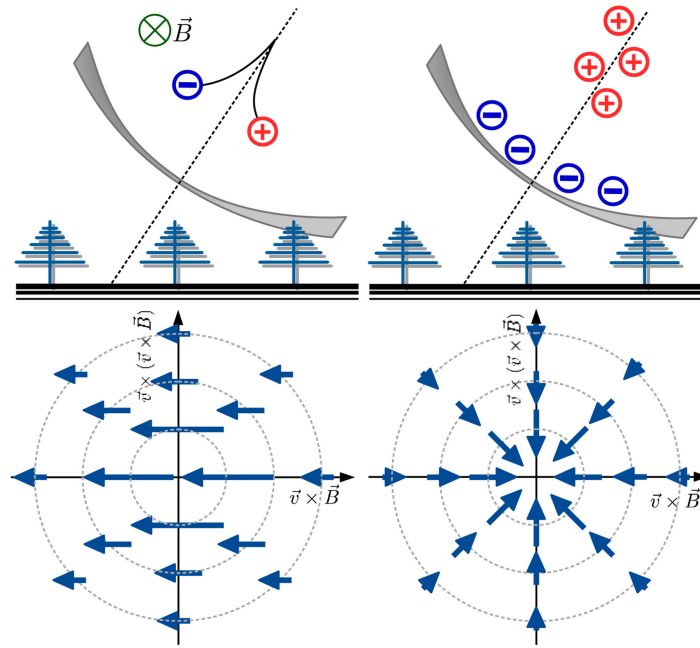


Figure 2.19: Radio emission of air showers due to geomagnetic effect (left) and charge excess (right) [59].

an energy estimator. For the SD array this optimal distance was found to be 1000 m [56]. This energy estimator still depends on the inclination angle, at larger angles the signal is attenuated more by the atmosphere. To eliminate this dependency the Constant Intensity Cut method [57] is used. The signal at the optimal distance is corrected to the signal at the median zenith angle. For the 1500 m array the median angle is 38° , the corrected energy estimator is called S_{38} . Analogously the energy estimator for the infill array is called S_{35} . These angular-independent energy estimators are calibrated with the FD energy for hybrid events as shown in Fig. 2.18 [55]. For inclined⁵ air showers the energy estimator is derived as described here [58].

2.2.4 AERA

Air showers also emit radiation in the radio spectrum. When the particles in an air shower travel through the atmosphere charge is separated by two different effects. In both cases, a time-variant dipole moment is induced, which emits radio waves. The dominating effect is the geomagnetic effect, which is caused by the magnetic field of the Earth. Electrons and positrons are deflected in opposite ways, depending on the charge. The second effect is caused by the ionization of air molecules. They remain behind the shower plane, the excess electrons are traveling with the shower. Both effects cause a characteristic polarization of the radio waves shown in Fig. 2.19. The Pierre Auger Observatory played an important role in the development of this technique with its radio array called AERA [60].

The radio emission from air showers is forward beamed. This makes it better suited for the reconstruction of inclined events. For inclined events, the footprint on the surface is much larger, which reduces the needed density of antennas. Unlike the particles, it also

⁵ inclination angle $\geq 60^\circ$

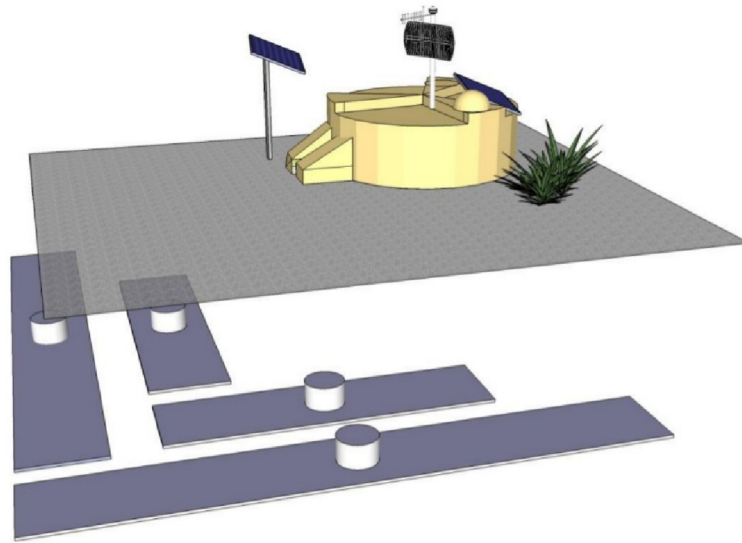


Figure 2.20: Schematic drawing of an AMIGA underground muon detector [62].

doesn't suffer from the attenuation of the signal because of the longer travel distance in the atmosphere, as the SD as radio waves get hardly absorbed [61].

2.2.5 AMIGA

The Pierre Auger Observatory also has a second type of surface detector, designed especially to detect muons, the AMIGA detector [62]. The electromagnetic particles are suppressed by burying the detectors. The 2.3 m overburden shields the detector from electrons, positrons, and photons. It consists of 5 m² and 10 m² modules of plastic scintillator, read out with a PMT. The layout of AMIGA modules in the vicinity of an SD station is shown in Fig. 2.20. The independent measurement of the muonic component can, for example, be used in composition analyses. Also, it adds to the discussion around the deficit of muons in simulations of air showers compared to the measurements [63].

2.2.6 Atmospheric Monitoring

The FD uses the atmosphere as a calorimeter, this implies the need to know the condition of the "instrument". Therefore, the Pierre Auger Observatory uses a variety of instruments to monitor the atmospheric conditions. They range from weather stations at the FD buildings to dedicated laser instruments to measure the amount of scattering in the atmosphere. The dominant correction hereby comes from scattering on aerosols in the atmosphere. Assuming an aerosol-free atmosphere would lead to an underestimation of the reconstructed air shower energy by 8 % at lower energies, to 25 % at the highest energies [64].

The Central Laser Facility (CLF) [65] and its later built but similar counterpart the eXtreme Laser Facility (XLF) are the main instruments for the analysis of the aerosol content in the atmosphere. They are placed close to the center of the SD array and shoot upward laser beams, which are then detected by the FD telescopes. Hourly average profiles are compared to a reference profile, which was taken in a presumably clean night with no aerosol content.

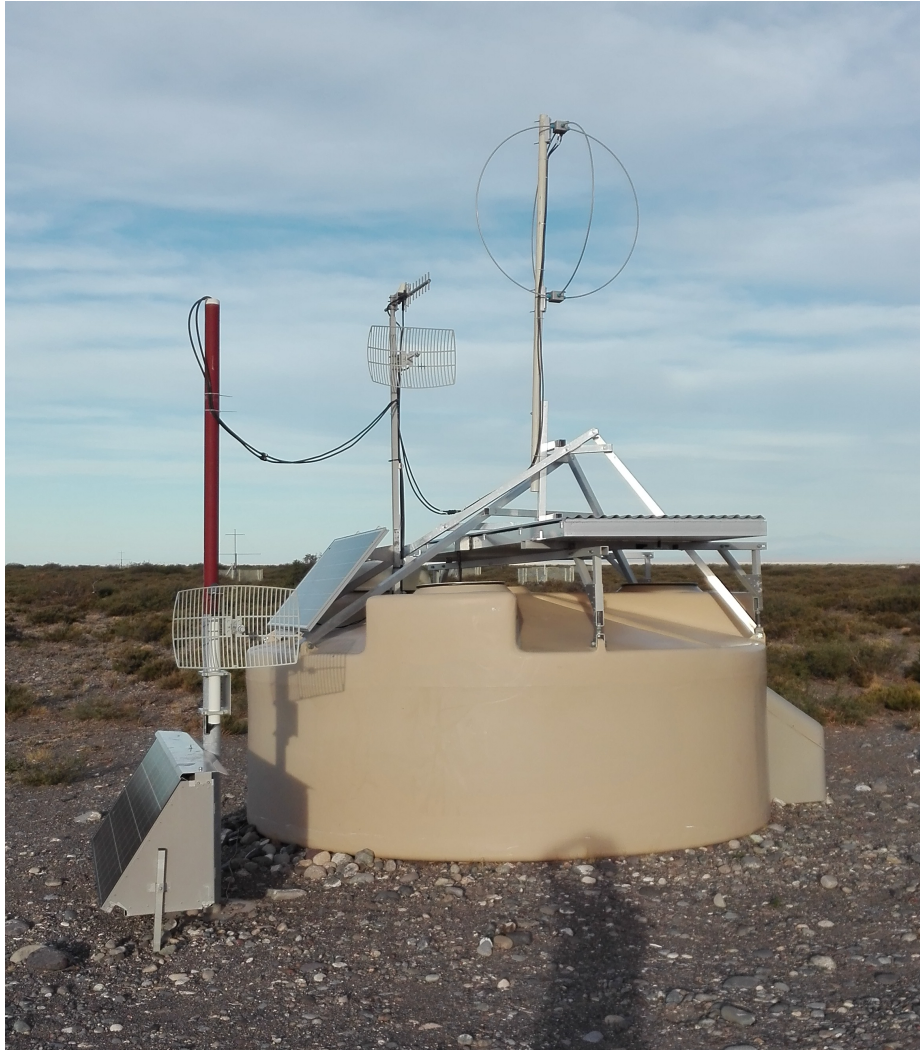


Figure 2.21: Fully upgraded SD station with SSD and radio antenna

From the difference, the vertical aerosol optical depth (VAOD) is inferred, a dimensionless measure for the extinction of photos by aerosols, depending on the height above ground [66].

Complementary lidars⁶ are installed close to the FD buildings [67] and at the CLF [68]. A lidar measures the backscattered light from a laser beam with its smaller⁷ telescope. The lidars close to the FD buildings are steerable and scan the close by atmosphere. They are also used to measure cloud height and coverage.

2.3 AugerPrime

At the moment the Auger Collaboration is undertaking an upgrade of their detectors [38]. The main goal is to obtain composition measurements up to the highest energies. Until now this was mainly done via the X_{\max} analysis with FD data. The FD, however, only has a duty cycle of $\sim 15\%$. Information on the mass composition at the highest energies is needed to discriminate between models for the acceleration and the transport of cosmic rays. A

⁶ like radar but with light ⁷ compared to the FD telescopes

population of protons at the highest energies would also point back to its sources as the deflection by galactic magnetic fields would be minimal. In the following, the components of the upgrade are briefly explained. A photo of a fully upgraded SD station is shown in Fig. 2.21.

2.3.1 The Surface Detector

The main part of the upgrade of the Pierre Auger Observatory is concerning the SD. A 4 m² scintillator detector (Scintillating surface detector (SSD)) is added on top of each WCD. The response of the SSD and the original WCD to the electromagnetic and the muonic component of the signal are different. Similar to X_{\max} , shown in Eq. (2.3), the fraction of muons in an air shower also depends on the primary mass. Air showers induced by iron nuclei have a higher fraction of muons compared to proton showers at the same energy. The separation of the electromagnetic and muonic components permits a composition analysis from SD data. Additionally a fourth smaller PMT is added to each station to extend the dynamic range of the water Cherenkov detector. To have a complementary measurement of the muonic component, the AMIGA detector is extended to the whole infill array.

2.3.2 The Fluorescence Detector

For the FD, the hardware stays unchanged in the upgrade of the Pierre Auger Observatory. However, a new mode of operation is planned. The goal is to increase the duty cycle of the FD. To achieve this, the gain of the PMTs is reduced to cope with the then higher background light flux, outside of the standard measurement time. This ensures the stability of the detector in the remaining lifetime of the observatory. An increase of the duty cycle by $\sim 50\%$ is planned. This is the topic of Chapter 3.

Although not officially part of the upgrade, a new calibration is being build for the FD. The “drum” calibration method was performed last in 2013 [69]. The absolute calibration is effectively discontinued at the time of writing and a replacement is urgently needed. A possible replacement for the drum method consists of a much smaller light source mounted onto an XY-Scanner. The new method and first results are shown in Chapters 4 and 5.

2.3.3 The Radio Detector

As an addition to the upgrade, a radio antenna will be added to each SD station [70]. The antennas will be Short Aperiodic Loaded Loop Antenna (SALLA) [71] antennas. For a full reconstruction of vertical air showers from the radio footprint, the 1500 m spacing of the SD is too sparse. However, the radio footprint grows with the shower zenith angle and allows for a sparser array for inclined air showers [61]. The antenna array offers an independent measurement of the electromagnetic component of an air shower, especially at large zenith angles where the sensitivity of the SSD drops. At large zenith angles, the projected area of the SSD becomes small and the electromagnetic component of an air shower is fully attenuated before reaching the ground. The radio signal, emitted by the electrons and positrons, however, does not get attenuated and can still be measured. Thus, measurements of the electromagnetic and muonic components are possible over the whole zenith angle range.

CHAPTER

3

Extended Uptime of Fluorescence Telescopes

Contents

3.1	The Duty Cycle of FD	26
3.2	Simulation Study at Reduced Gain	28
3.2.1	Reconstruction Efficiency	29
3.2.2	Expected Number of Events	31
3.2.3	Data Quality	33
3.3	Test Measurements	34
3.3.1	PMT Stability	34
3.3.2	On Site	35
3.3.3	Atmospheric Monitoring	36
3.4	Calibration	36

The analyses of the Pierre Auger Collaboration are limited at the highest energies by the low number of events caused by the steeply-falling spectrum of cosmic rays. This problem becomes even more severe when the analysis requires FD data, as for example the X_{\max} analysis and the energy calibration of the SD, because of the low duty cycle of the FD of $\sim 15\%$ [38]. In this chapter, a new mode of operation for the FD is introduced. This new mode of operation is part of the upgrade of the Pierre Auger Observatory [38] and has the goal to increase the duty-cycle of the FD.

The biggest limit to the standard operation duty cycle comes from the amount of background light close to the full moon period. If the duty-cycle is to be increased, the telescopes must be able to cope with more background light. The idea is to reduce the gain of the PMTs, as is was done for the MAGIC¹ [72] and VERITAS² [73] telescopes in gamma-ray astronomy. The PMTs in the camera can then also measure closer to the full moon period. At reduced

¹ Major Atmospheric Gamma Imaging Cherenkov Telescopes ² Very Energetic Radiation Imaging Telescope Array System

gain, the detection efficiency, the distance to the telescope up to which an air shower can be detected, and the quality of the data will also be reduced. Therefore, it is expected that this method will only yield satisfying results at the highest energies, where we are limited most in our statistics by the steeply falling cosmic ray spectrum but not by the number of photoelectrons in the PMTs. In the following, results from simulations of the duty cycle of the FD will be shown and the possible gain in measurement time will be discussed. Then a full air shower simulation at reduced gain will be presented to show how many more events we can get at the highest energies, and what the quality of the data will be. At the end of this chapter, the results of test measurements are presented.

3.1 The Duty Cycle of FD

The current standard measurement time is defined by the following limits:

- Sun 18° below horizon (astronomical night)
- Moon fraction below 70 % (at midnight)
- Variance in the PMTs below 100 ADC^2
- At least 3 h of continuous measurement time

These limits were determined such that the aging of the PMTs, due to the accumulated anode charge, is slow enough to ensure operation during the lifetime of the observatory. The important limit here is that the variance in the PMTs does not exceed 100 ADC^2 . Therefore, the gain of the PMTs has to be changed if the measurement time is to be increased. The variance depends quadratically on the gain, the plan is to reduce the gain by a factor of 10.

The following calculations and plots were made on simulations of the background flux during nights with the same program that is used to generate the measurement plan of the FD-shifts [74]. The years from 2014–2017 were simulated to average out effects from the shifting of the moon phases. For each minute during the astronomical night, the expected variance from the background light flux is calculated. This covers only the diffuse light flux which affects all telescopes. If the moon is inside the field of view of a telescope the background light flux is higher and this single telescope cannot take data, this is ignored in the following calculations.

In Fig. 3.1 the blue line shows the dependence of the duty-cycle on the illuminated moon fraction at midnight if this was the only criteria. The bottom x-axis shows the maximum variance³ the PMTs would have to endure if these nights were to be included in the measurement schedule. For comparison the theoretical duty cycle, if all of the criteria above are applied, and also the real duty cycle, which is around 15 %, are also plotted. The theoretical duty-cycle is above the blue line as we make shorter measurements in nights with too much moonlight as long as the moon is below the horizon. The real duty cycle comes from the criteria above plus the downtime of the detector because of unstable conditions, which include bad weather and power cuts. As a rough estimate from this plot, if the duty cycle is to be increased by 50 %, the PMTs would need to endure a variance of 1000 ADC^2 at standard operation. Without reducing the gain this is not possible without damage to the PMTs.

Table 3.1 shows the increase of the duty cycle for different possible scenarios. There, the duty-cycle of the FD was calculated with different thresholds for the variance at standard

³ with standard operation gain

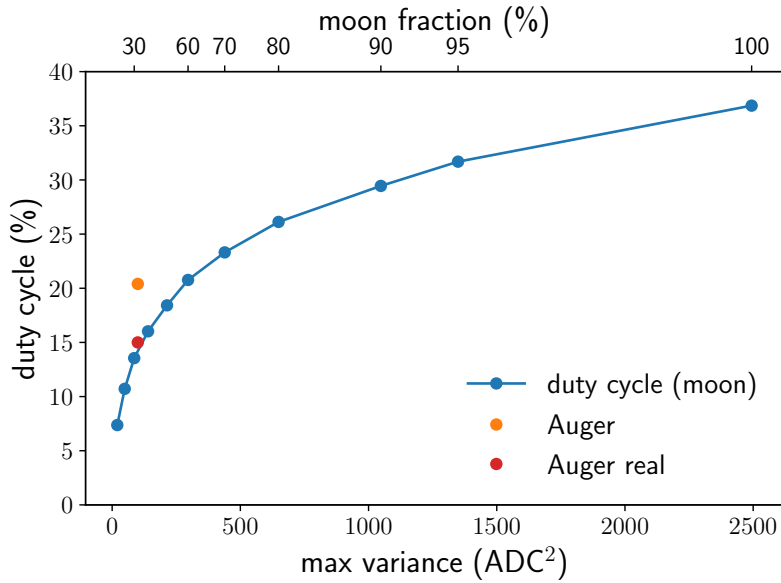


Figure 3.1: Duty-cycle of the FD. Blue is the duty cycle depending on the maximum illuminated moon fraction (upper x-axis). The bottom axis shows the maximum variance in the corresponding nights. The orange marker is the duty cycle when all criteria are applied, and red the one achieved in practice.

Table 3.1: The gain in measurement time for different possible modes of FD operation at reduced gain

mode	duty-cycle (%)	change (%)
standard	20.4	–
standard+	24.6	+ 20.5
variance $\leq 1000 \text{ ADC}^2$	31.4	+ 53.7
variance $\leq 1000 \text{ ADC}^2$ min. 3 h	30.8	+ 50.9
variance $\leq 2000 \text{ ADC}^2$	36.3	+ 78.2
astronomical night	36.9	+ 80.7

operations. The standard+ label means, that for each night we currently take measurements in, we measure for the whole night, which would not extend the time shifters are needed in Malargüe. The maximum baseline variance in a PMT for this scenario would be $\sim 500 \text{ ADC}^2$. For a maximum variance of 1000 ADC^2 the duty-cycle increase is $\sim 50\%$. Applying the same cut of at least 3 h of continuous measurement time does not change the result by much.

The additional uptime from extending the measurements into twilight time is not discussed here. For an illustration of the different twilight definitions see Fig. 3.2. In the current implementation of the measurement schedule, twilight is not included, meaning that the sun has to be at least 18° below the horizon. As a rough estimate, allowing for astronomical twilight would gain us an additional 24 minutes of measurement time per day.

$$2 \cdot \frac{6^\circ}{360^\circ} \cdot 24 \text{ h} = 24 \text{ min} \quad (3.1)$$

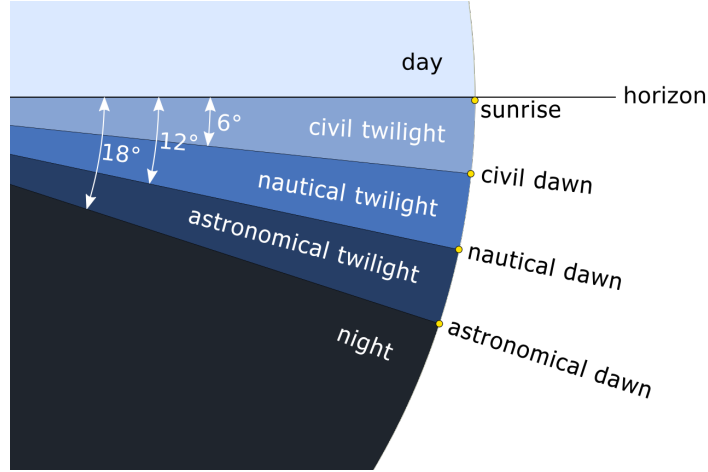


Figure 3.2: Illustration of the different definitions of twilight [75].

3.2 Simulation Study at Reduced Gain

Simulations with reduced gain do not work with the standard `Offline` [76] settings. The problem here is that the thresholds for the FLT were derived with the assumption that the electronic noise is negligible. This assumption holds for standard operation, but not for low gain as the electronic noise is a constant and does not scale down with the gain. The baseline variance V_{ADC} is given as:

$$V_{\text{ADC}} = V_{\text{NSB}} + V_{\text{elec}}, \quad (3.2)$$

where V_{NSB} is the variance of the baseline coming from the night-sky background photons and the PMT, and V_{elec} is the additional variance coming from the readout electronics. The night-sky background and the secondary electron emission at the dynodes of the PMT have Poissonian errors. The quantum efficiency and the electron collection efficiency at the first dynode follow a binomial distribution. Thus V_{NSB} can be written as [77]:

$$V_{\text{NSB}} = n_{\text{pe}} \times (1 + V_G) \times G^2, \quad (3.3)$$

with n_{pe} being the mean number of photo electrons at the PMT per unit time, V_G the gain variance and G the gain. A typical value for V_{elec} is 3.5 ADC^2 . At low gain, the electronic noise is the dominant contribution to the baseline variance over a wide range of background light fluxes. A new application was written within the `Offline` framework to simulate FLT threshold values at low gain. For a description of how the new threshold values are simulated and how to use them see Appendix C. A plot of the FLT threshold values at low gain as a function of n_{pe} is given in Fig. 3.3. One can see that the threshold stays constant for the first few photoelectron values, which shows that the electronic noise is the dominant contribution here. At standard conditions a typical value for n_{pe} is ≤ 20 .

In the following air shower simulations made with CONEX [78] in `Offline` at low gain are presented. The simulations were done with the gain reduced by a factor of ten. To simulate the higher night-sky background flux, constants were added to the flux table for a dark moonless night, used in the standard simulation All used values are given in Table 3.2. For comparison, the corresponding baseline variance these simulations would have for standard conditions are also given. The highest value is comparable to the maximum seen in the simulation of the duty cycle above.

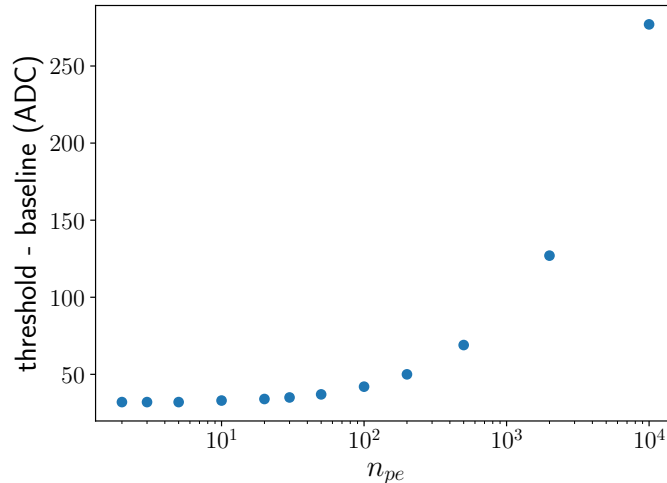


Figure 3.3: Simulated threshold at low gain as a function of the number of photoelectrons n_{pe} . The threshold is given in ADC for a baseline subtracted trace.

Table 3.2: Background light flux used in simulation. The variance given is what it would be in standard operations. At low gain the part from the background light flux would be scaled down by a factor of $gain^2$

$\Delta\phi$ (/m ² /deg ² /μs)	var (ADC ²)	$\Delta\phi$	var
0	28	1000	279
100	54	2000	531
200	79	3000	784
300	104	4000	1036
400	129	5000	1288
500	155	7000	1789
750	218	9000	2295

For each background flux value and for five different steps in energy⁴ above 1×10^{19} eV, 10 000 air showers were thrown randomly over the whole array of the SD. The maximum zenith angle used in the simulations is 60 degree. The primaries are 50 % proton and 50 % iron.

3.2.1 Reconstruction Efficiency

The goal of this study is the number of additional events we get from the operation of the FD with low gain. Thus the reconstruction efficiency is used here instead of the detection efficiency. The first step is the reconstruction efficiency versus the distance to the telescope. An example of the reconstruction efficiency can be found in Fig. 3.4. This ratio of reconstructed to simulated showers as a function of the distance shows a clear dropoff when the air showers are too far away from the telescope, and thus the signal is too faint compared

⁴ $1 \times 10^{19}, 1 \times 10^{19.3}, 1 \times 10^{19.5}, 1 \times 10^{19.7}, 1 \times 10^{20}$

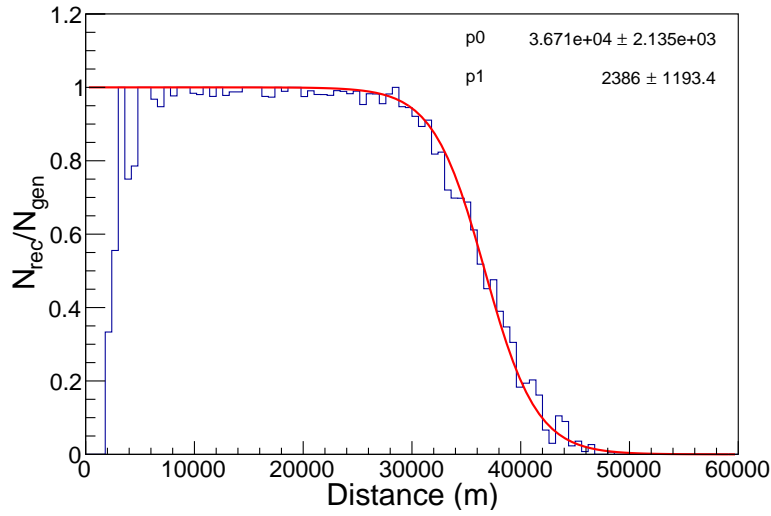


Figure 3.4: Reconstruction efficiency vs. distance at an Energy of 1×10^{20} eV and baseline variance at standard conditions of 279 ADC^2 . Note that the reconstruction efficiency also drops when the shower core is too close to the telescope, as the tracklength gets too short. The fitted function is the Fermi distribution.

to V_{ADC} , to be reconstructed. This distance grows with energy and shrinks with increasing background flux. At low gain, this distance is smaller compared to standard operation. The main reason for this is not so much the change in gain, as signal and background are scaled in the same way, but the electronic noise. V_{elec} is independent of the gain and thus, as visible from Eq. (3.2), larger in relative terms. Full reconstruction efficiency over the SD array is reached when the distance, at which the dropoff happens, is larger than the distance between the FD buildings.

A better illustration of the reconstruction efficiency is a 2D version of Fig. 3.4. Examples for different energy and background light flux can be found in Fig. 3.5. Figs. 3.5(a) to 3.5(c) show the reconstruction efficiency for a baseline variance of 2295 ADC^2 and for three different energies, 1×10^{19} eV, $1 \times 10^{19.3}$ eV and $1 \times 10^{19.5}$ eV. As expected, the area in which air showers can be reconstructed grows with energy. At $1 \times 10^{19.5}$ eV the full reconstruction efficiency over the SD array is almost reached. For comparison, the map for 1×10^{19} eV is also shown with a baseline variance of 28 ADC^2 in Fig. 3.5(d). Here the area in which air showers can be reconstructed is much larger as in the corresponding map at 2295 ADC^2 . The interesting point here is, for which energy and baseline variance the full reconstruction efficiency over the SD array is reached. Above this, the amount of additional events scales only with the additional amount of measurement time.

By integrating over these maps and dividing over the total area, the reconstruction efficiency over the whole array is obtained. The results are shown in Fig. 3.6. If we take a baseline variance of 1000 ADC^2 we reach 90% reconstruction efficiency over the whole SD-array at roughly $1 \times 10^{19.5}$ eV. This means that we can reconstruct all the additional events at the highest energies and the extension of the measurement time should be equivalent to the gain in events. For comparison, the reconstruction efficiency for standard conditions is also plotted. As we only requested that the events should reconstruct so far, it is unclear if we would gain events usable in standard physics analyses. To tackle this problem the same plot is also shown with the cuts from the X_{max} -analysis applied. The cuts used are comparable

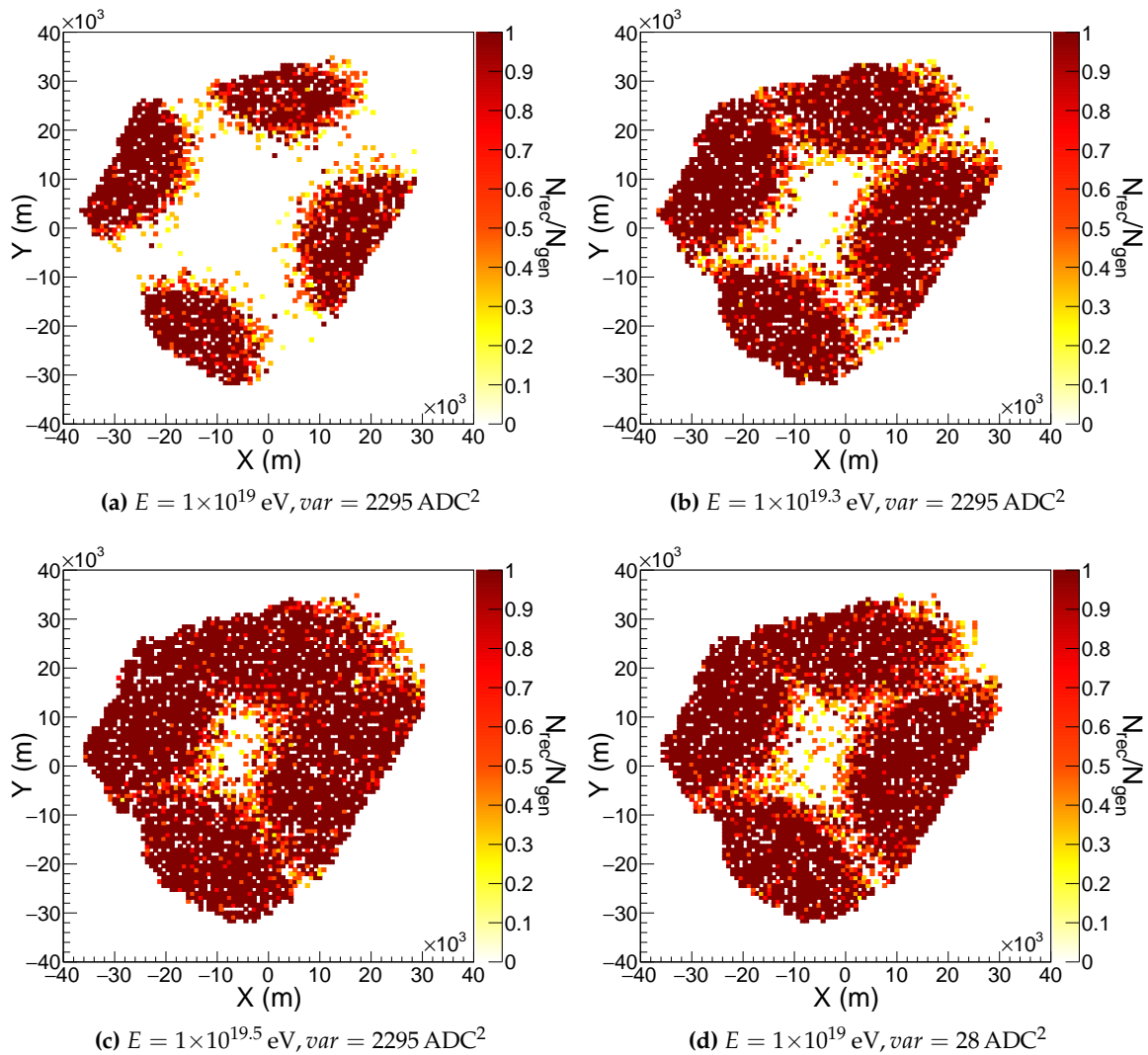


Figure 3.5: Reconstruction efficiency maps. (a), (b) and (c) show how the area in which air showers can be reconstructed increases with energy, for a baseline variance at standard conditions of 2295 ADC^2 . (d) shows the lowest energy map for a baseline variance of 28 ADC^2 , where the area is much bigger compared to the high variance version.

to the ones used here [79]. The efficiency drops a little bit compared to the simulation at standard conditions. At the highest energies, it is still above 80 % relative to the simulation at standard conditions.

3.2.2 Expected Number of Events

The combination of the reconstruction efficiency with the duty cycle gives us a handle on the expected number of events. As an estimator for the additional events N , the product for the measurement time with the reconstruction efficiency is used. For an estimate of the measurement time, the data from the duty cycle simulation above was used. The time in minutes was binned in the steps of the PMT baseline variance as given in Table 3.2.

$$N(E) = \sum_i n_i \times \epsilon_i(E), \quad (3.4)$$

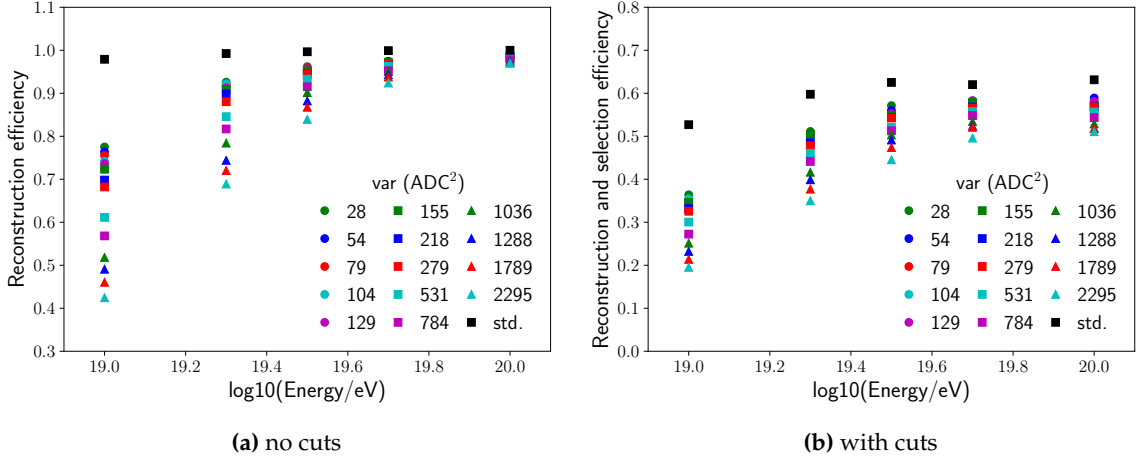


Figure 3.6: Reconstruction efficiency over the whole array without (a) and with (b) cuts applied. Note the change of scale on the y-axis.

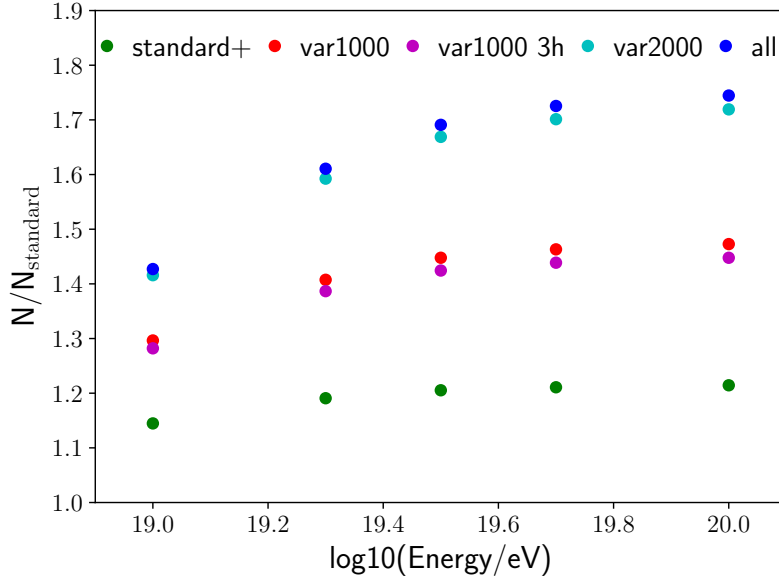


Figure 3.7: Expected number of additional events for the different possible modes of operation presented in Table 3.1.

with n_i being the measurement time in minutes for the i^{th} bin and $\epsilon_i(E)$ the reconstruction efficiency at the upper border of this bin, as shown in Fig. 3.6(a). The first four bins are in the range of standard operations and therefore used as a reference in the following. The reconstruction efficiency for standard operations in this energy range is approximately one, see Fig. 3.6(a), thus Eq. (3.4) simplifies to

$$N_{\text{ref}}(E) = \sum_{i=1}^4 n_i \times \epsilon_i(E) = \sum_{i=1}^4 n_i. \quad (3.5)$$

All other bins are then summed up and divided by the reference. Thus, the results are a conservative estimate, as the reconstruction efficiency is always from the higher border

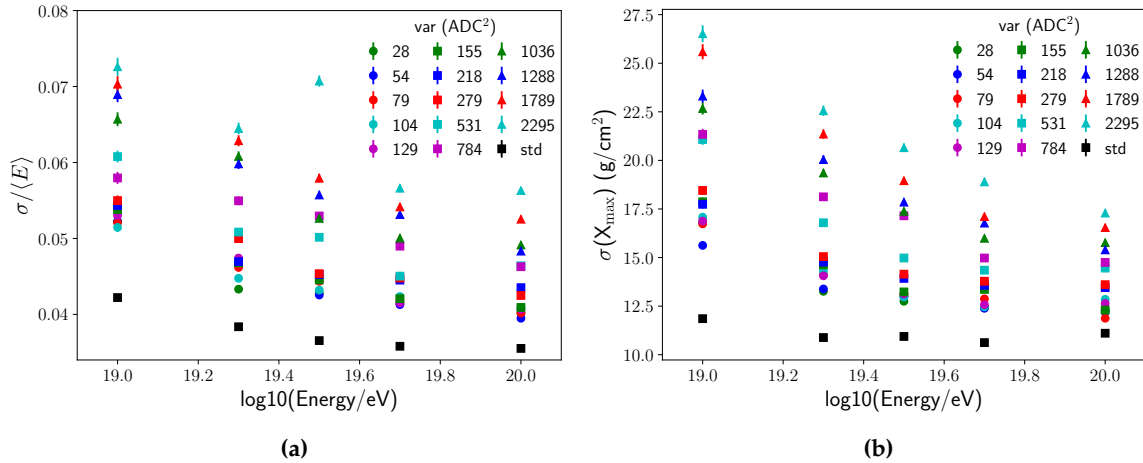


Figure 3.8: Data quality at low gain. (a) energy and (b) X_{\max} resolution at low gain for different background light fluxes. Both compared to standard simulations.

where it is the worst over the binning in baseline variance. The results for different scenarios, discussed in Section 3.1, are shown in Fig. 3.7.

In [38] an additional amount of 514 ± 27 events are expected above an energy of 10^{19} eV for measurements with standard conditions during the AugerPrime time. 52 ± 9 above $10^{19.5}$ eV. This roughly translates to 73 additional events above 10^{19} eV and 7 above $10^{19.5}$ eV per year. For the assumption that the low gain duty cycle suffers from the same reduction caused by bad weather conditions and power cuts, the relation in Fig. 3.7 holds. In the currently favored scenario, with a maximum baseline variance of 1000 ADC², this would result in a combined additional amount of ~ 11 events per year above $1 \times 10^{19.5}$ eV instead of 7.

3.2.3 Data Quality

More background and an overall higher noise level is equivalent to a decrease in data quality. The important question is if the decrease in resolution undoes the increase in statistics. How the energy and X_{\max} resolution changes with the background is shown in Fig. 3.8. For comparison, the same simulation at standard conditions is also given.

The X_{\max} resolution shown here is slightly better than shown in [21]. This is not surprising, as a partly idealized detector simulation was used here. If the relation observed here holds for the full RealMC⁵ simulation the decrease in resolution is always below a factor of two. This for background up to a baseline variance of 1000 ADC², for lower background levels the resolution is better. Overall the resolution is still good enough to separate the different primary classes. The decrease in resolution for the energy is also tolerable and in the same range as for the X_{\max} resolution. Again the resolution is slightly better than the one usually reported [80], presumably caused by the idealized detector description.

⁵ Monte Carlo simulation of air shower plus FD detector response where the time-dependent background and state of the detector is taken from real data

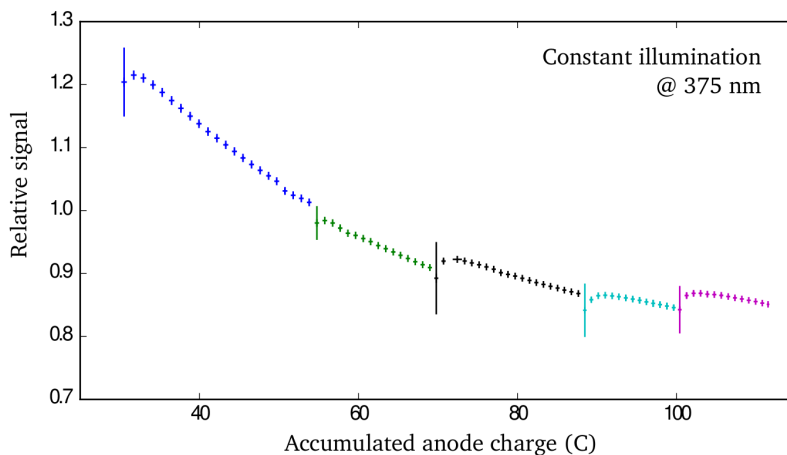


Figure 3.9: Measured PMT response as a function of accumulated anode charge. The jumps come from recovery after breaks in the measurements [38].

3.3 Test Measurements

To further investigate the operation of the FD at reduced gain, test measurements have been done on site. The test measurements are distributed over four campaigns.

- February/March 2015: test measurements with one telescope to see if air showers can be recorded at low gain
- June 2016: test measurements with two telescopes to see if the CLF shows up in the data, as it is needed for atmospheric monitoring
- March 2018: test measurements with a whole FD building to get more statistics
- November 2018: additional measurements during a shift to get more laser shots from the CLF

A complete list of the measurements with dates and run numbers is given in Appendix A.2. Most of the air showers detected at the Pierre Auger Observatory are at low energies. As those showers are lost when going to low gain the trigger rate is reduced significantly. Estimated from the test measurements the TLT trigger rate will be around 1/min when taking data with all telescopes. When switching between high voltage levels, Cal A and Cal B were done twice, once at each gain level. This was done to ensure the correct switching of the gain levels.

3.3.1 PMT Stability

Prior to this work the aging of the PMTs was tested in the laboratory [81, 82]. The question was if the aging accelerates with the higher background light flux. The results were, that the aging does not change with background light and only depends on accumulated anode charge. For standard operation the accumulated anode charge is 2.7 C per year, the estimate for low gain operation is an additional 5 C per year. This is small enough so that the lifetime

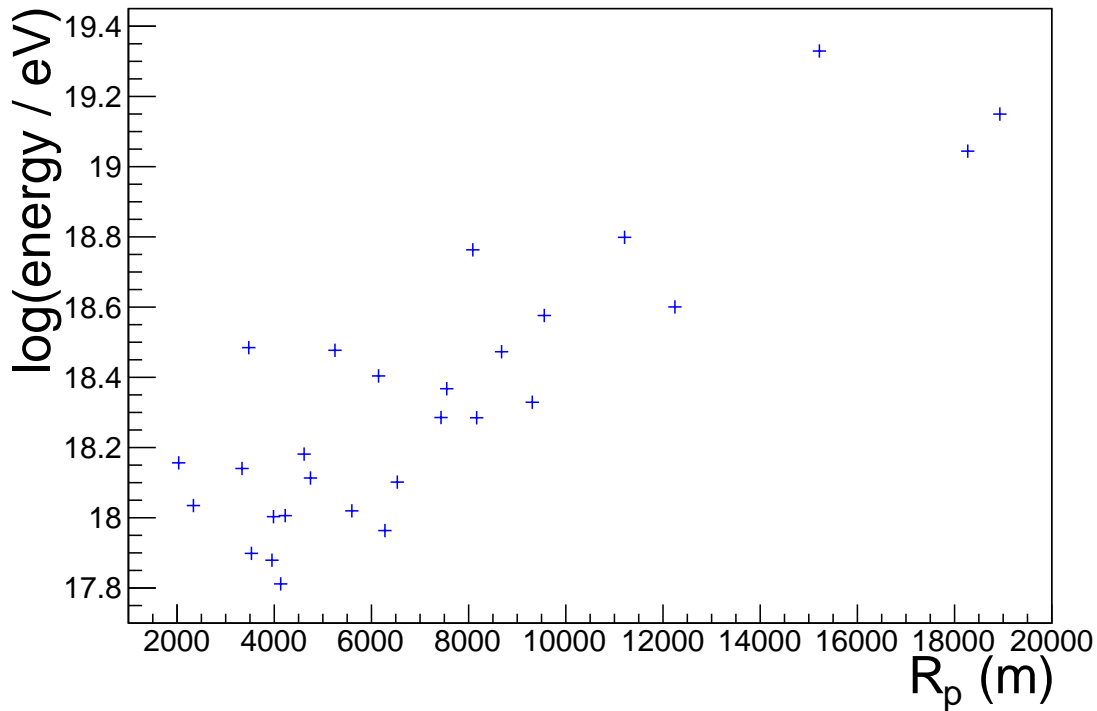


Figure 3.10: Energy of the measured events at reduced gain versus the distance to the telescope. R_p is the distance of the closest approach to the telescope.

of the PMT, which typically is reached after 250 C of accumulated anode charge, is compatible with the remaining lifetime of the observatory [38]. The measurements were done with a spare FD PMT and HEAT electronics.

3.3.2 On Site

The first test measurements at low gain were presented in [83]. Here we present a systematic study of the reconstruction efficiency, as a crosscheck the simulation study above. In Fig. 3.10 the reconstructed energy and distance to the telescope for all reconstructed events, starting from the second test measurement campaign, are plotted. As expected, there are many events at low energy close to the telescopes. For higher energies, the majority of the events are at the edge of the observable area. One can see that the distance, under which events are reconstructable, grows roughly linearly in logarithmic energy. Thus the area grows quadratically, making it more likely to record an air shower at a larger distance. There are three events in the targeted energy range above 10^{19} eV. An example is shown in Fig. 3.11. At 10^{19} eV the distance at which the reconstruction efficiency drops below 50%, see Fig. 3.4, is $\sim 21\,700$ m for a baseline variance of 100 ADC^2 and $\sim 17\,700$ m for a baseline variance of 1000 ADC^2 . Thus, the event at $\sim 10^{19}$ eV is at the border of what is reconstructable at this energy in the targeted background light range.

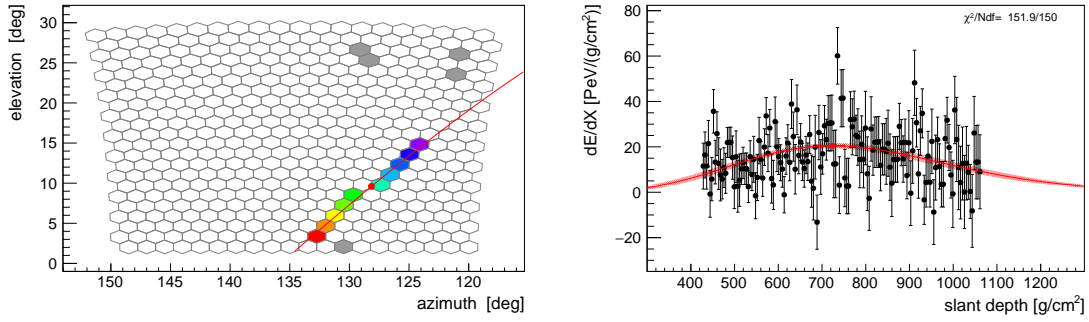


Figure 3.11: Measured event at low gain. $E = (1.14 \pm 0.08) \times 10^{19}$ eV, $X_{\max} = (724 \pm 27)$ g cm $^{-2}$ at ~ 19 km distance to the telescope.

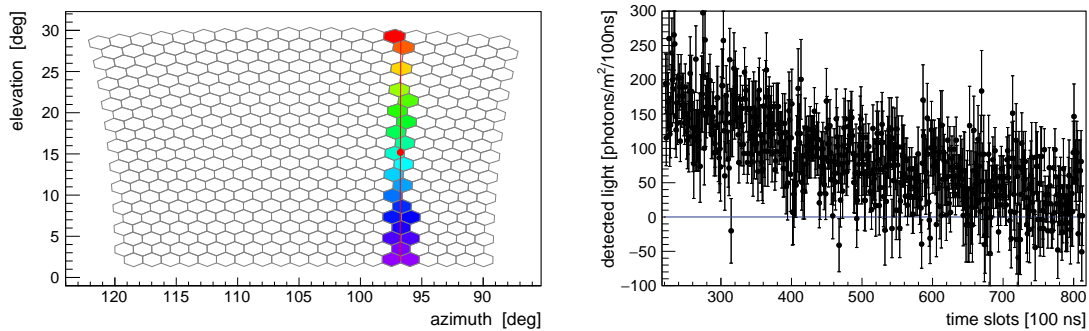


Figure 3.12: Measured laser shot from the CLF at reduced gain. The track spans the whole camera, although some pixels are missing at the top (left). (right) shows the reconstructed photon trace.

3.3.3 Atmospheric Monitoring

An important prerequisite for the new mode of operation is also if the atmospheric monitoring works at low gain. From the instrument side, CLF or XLF, nothing changes. The detector for the atmospheric monitoring, however, is also the FD. An example for a recorded laser shot at low gain is shown in Fig. 3.12. If the VAOD is calculated as at standard gain [66], the statistical uncertainty would be increased. At the moment the aerosol uncertainties contribute 1.2% to 3.8% to the energy resolution of the FD, growing with energy [80]. There are two possible options to reduce the statistical uncertainties at low gain. One is to shoot the lasers more often, which would increase the dead time of the detector. The other is to take the average of the laser shots over a longer time, this way we would lose sensitivity to short-time changes in the VAOD [84].

3.4 Calibration

An important part of the test measurement was to check if the calibration system can cope with the change of gain settings. The preferred way would be to use the same absolute calibration for both standard and low gain operations. The gain level would then be tracked through the relative calibration system. To ensure usage of the correct calibration values from the databases both relative calibration runs, before and after switching of gain levels,

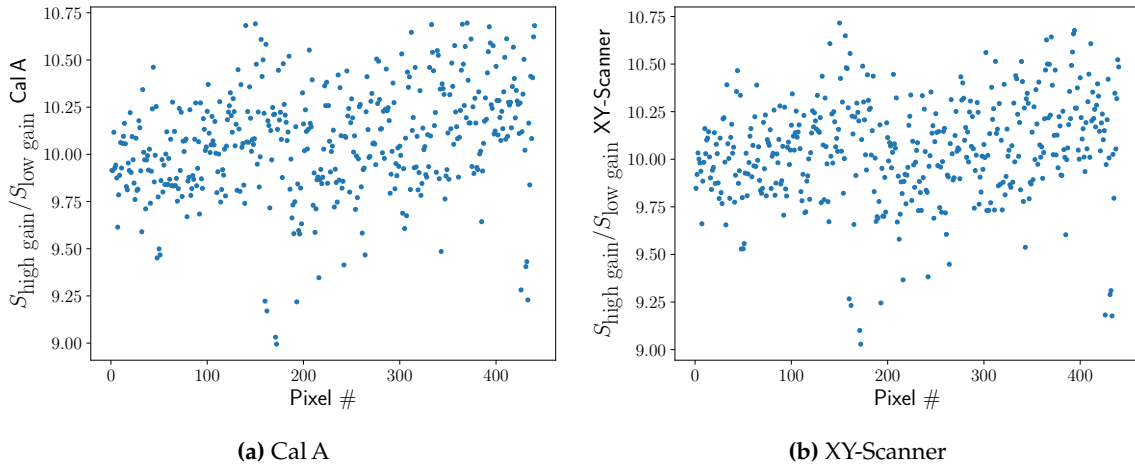


Figure 3.13: Gain ratio between standard and low gain operation, measured with both the (a) relative calibration and the (b) XY Scanner.

need to go into the database. Currently only the last Cal A of a night enters the calibration database.

In the test measurements, the relative calibration was used to check the correct switching of the gain levels. Cal A would have been the perfect tool for this. However, the online reconstruction of Cal A does not work at low gain. The reason for this is, that the online reconstruction algorithm expects a certain pulse height as an indication of a successful calibration measurement. At low gain, the signal is reduced and the pulses are too small to be accepted. The data, however, is not lost and can be reconstructed offline.

Cal B is also used for linearity tests of the PMTs. It is equipped with a filter wheel with 5 different attenuation steps. This reduces the pulse height, thus the online reconstruction program accepts smaller peaks, furthermore also at low gain. Therefore, Cal B was used to check the gain level in the test measurements.

Although it is not planned to perform the absolute calibration of the FD also at low gain, a test measurement at low gain is necessary to crosscheck the relative calibration system. The drum is discontinued and can not be used for this test. Instead, the “XY-Scanner” is used, this is the new method for the absolute calibration of the FD which will be introduced in the following chapter. The following sequence of measurements was carried out.

- Cal A, XY-Scanner, Cal A at standard gain
- Switch to low gain
- Cal A, XY-Scanner, Cal A at low gain

The ratio of the signal at high and low gain for both methods, Cal A and the XY-Scanner, is shown in Fig. 3.13 for each PMT in the camera. On average, both methods reproduce the factor of 10, which the gain was changed by. The PMTs which deviate from the factor of ten are the same in both methods. As both methods yield consistent results an absolute calibration at low gain is not necessary. The same absolute calibration measurement can be used for both gain levels, and the change of gain be tracked with the relative calibration system.

CHAPTER

4

A new Method to Calibrate Fluorescence Telescopes

Contents

4.1	The Light Source	40
4.1.1	Calibration	43
4.1.2	Characterization	44
4.2	The Scanner	47

The calibration of the FD is of utmost importance to the Pierre Auger Observatory as the energy scale of the whole experiment is set by it. The calorimetric measurement of air showers with the FD is used to cross calibrate the SD through hybrid events [55]. In this way, the good energy measurement of the FD is connected with the large duty cycle of the SD.

The end-to-end calibration of the fluorescence telescopes is done with the “drum”, as explained in Section 2.2.2. This method uses a light source of the size of the aperture which is mounted onto the telescope. Unlike in air-shower measurements, all PMTs are illuminated at once. The calibration and uniformity measurements of this light source are described in [39, 85]. The most recent drum calibration was performed in April 2013 [69], since then the drum calibration is effectively discontinued. Also in the time previously the envisaged yearly calibration measurements were not performed, because this method is very time-consuming and requires a lot of manpower. A replacement of the drum should meet the following requirements:

- Comparable or smaller systematic errors
- Easier to calibrate
- Less work and manpower needed for transport and operation
- Possibility to calibrate at least three telescopes per night

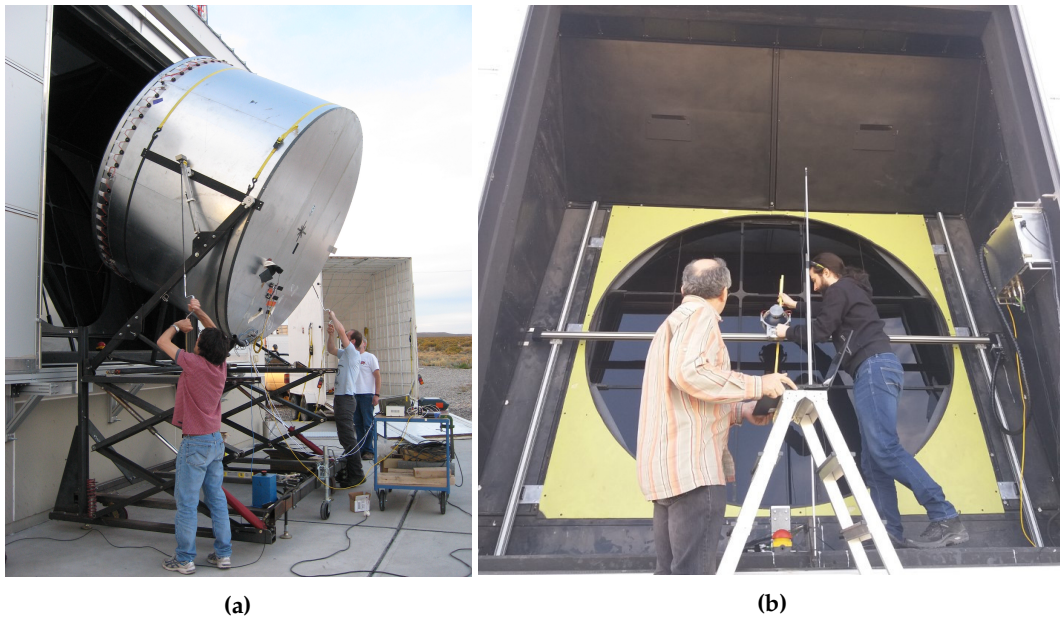


Figure 4.1: Photos of the (a) Drum and the (b) XY-Scanner during the mounting of the lightsource.

The idea is to go from a large light source, illuminating the whole aperture at once, to a much smaller light source and to take many measurements at different positions on the aperture. The sum of all measurements is expected to resemble the measurements taken with the drum. The realization of this new method is done with an LED inside of an integrating sphere, which is mounted on a scanner. The scanner consists of two independent linear stages which can move the sphere on the aperture. The hardware used for this new end-to-end calibration method is described in the following sections, and from now on called the “XY-Scanner”. Pictures of the mounting of both light sources are shown in Fig. 4.1, it can clearly be seen that the handling of the XY-Scanner is much easier.

4.1 The Light Source

In the reconstruction of data from the FD of the Pierre Auger Observatory, the cosine dependence of the aperture can be ignored, because it is absorbed into the calibration constants. The light from the drum follows the Lambertian emission spectrum, which has the same cosine dependence one would see from a constant flux at different angles. This is ignored in the reconstruction of the calibration measurements and thus the cosine dependence of the aperture can also be ignored in the reconstruction of air showers. An integrating sphere, with the light source inside, is by design a Lambertian emitter and, therefore, an obvious choice for the light source of the new calibration method.

The integrating sphere used for the prototype, which was used for most of the measurements covered in the following chapter, is a general-purpose sphere from Labsphere of type 4P-GPS-053-SL [86]. The diameter of the sphere is 5.3 inch in diameter and has four ports. The exit port has a diameter of 2.5 inch. Two smaller 1 inch ports are on the equator of the sphere and hold the LED and a photodiode as an internal reference, as shown in Fig. 4.2(a). The fourth port is opposite to the exit port and has a plug because it is not needed here. A

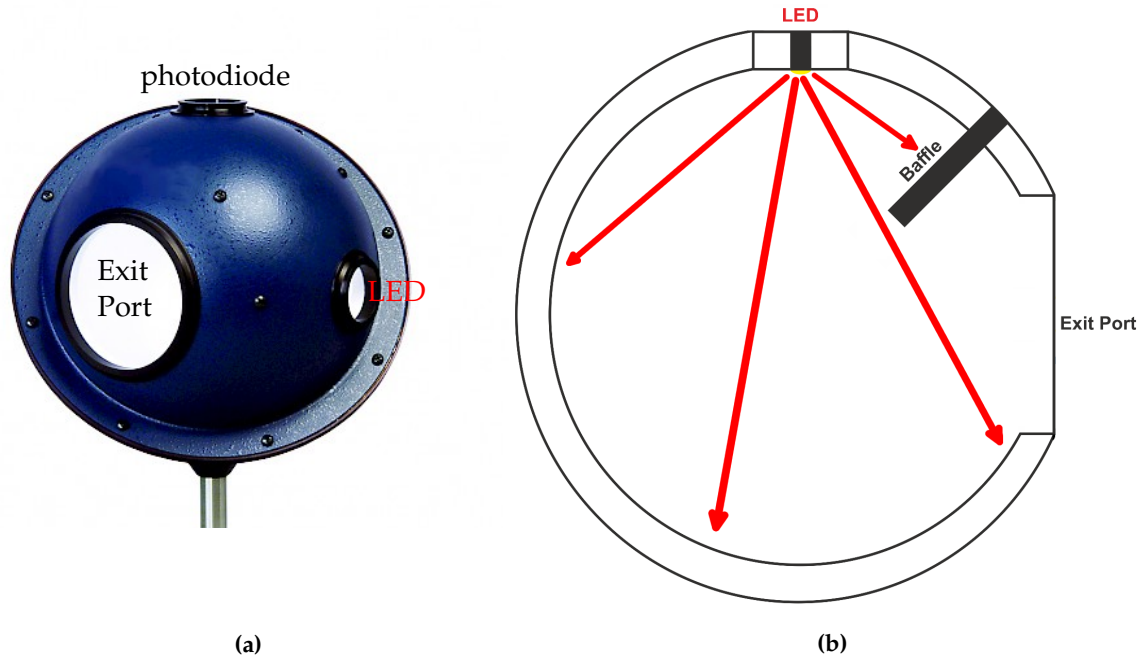


Figure 4.2: (a) picture of integrating sphere with positions of LED, photodiode and exit port indicated [86]. (b) illustration of the baffle blocking direct light from the LED to the exit port of the sphere. Adapted from [87]

baffle is in between the LED and the exit port to block direct light. This sphere is called the “Karlsruhe sphere” in the following.

The uniformity of the emitted light of the integrating sphere is reached by a multitude of internal reflections. Thus the sphere is coated with spectralon [88] on the inside, which is a Lambertian reflector. The reflectivity is $> 99\%$. To achieve a good homogeneity in the light output, the diameter of the sphere should be three times the diameter of the exit port [89]. This condition is not met for our sphere, here the diameter ratio is ~ 2 . Measurements of the spatial and angular homogeneity and the optimization of the sphere design will be covered below. For calibration measurements of the telescopes a good angular homogeneity is important, each PMT sees the same angular range of the emission spectrum from each position on the aperture.

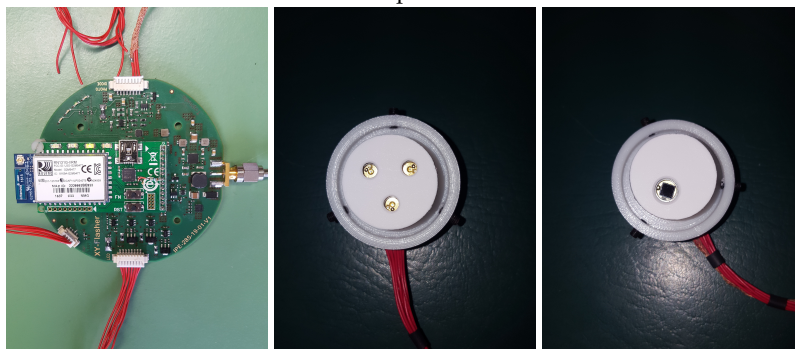
Both the LEDs and the photodiode are integrated into “heads”. The LED-head houses three LEDs of type UVLED365-110E from Roithner Lasertechnik GmbH [90], each LED has its use case.

- LED 1 is intended as a reference to check the aging of the other two LEDs and therefore should rarely be used.
- LED 2 is for the actual measurements in the field or calibration of the light source.
- LED 3 is for testing in the lab before the actual measurements are done with LED 2.

The arrangement of the three LEDs on the head is shown in Fig. 4.3(b), the position of the head in the sphere was marked to always have the same orientation in the measurements. In the test measurements, different versions of the electronics were used. The first one allowed for steps in the LED current on 1 mA up to 20 mA. In the very first measurements, at the



(a) sphere



(b) electronics

Figure 4.3: Light source of the XY-Scanner, Photos of the (a) sphere and (b) flasher board, LED and photodiode (left to right). In (a) the flasher board is in the gray box.

beginning of a shift 3 mA of LED current were chosen. This did produce pulses close to saturation in the PMTs. Over the course of an FD shift the PMTs get more sensitive [49] and the pulses in camera saturated. To be able to operate the XY-Scanner close to saturation in the telescope the steps in LED current were changed to 0.1 mA with a maximum of 10 mA for later versions. All measurements were done with a pulse length of $5 \mu\text{s}$ ¹, as it was done for the drum calibration method [39].

The photodiode is of type S1336-44BQ from Hamamatsu [91] and intended to check for relative changes in the measurements. Both the LEDs and the photodiode head are temperature stabilized to $30 \pm 1^\circ$ to minimize the temperature-dependent change of the efficiency. The temperature stabilization, as well as the pulse settings for the LED and the readout of the photodiode, is done by the “flasher board”, produced by the Institute for Data Processing and Electronics (IPE) at KIT [92]. The communication with the flasher board is done via WiFi.

In Fig. 4.4 an online progress display is shown, which was used to track the status of the calibration measurements at the telescopes. The top left panel shows the temperature stabilization of the LED and the photodiode. After turning on the flasher board, 5 min are needed

¹ or 50 bins in the PMT trace of a standard telescope, 100 bins for HEAT

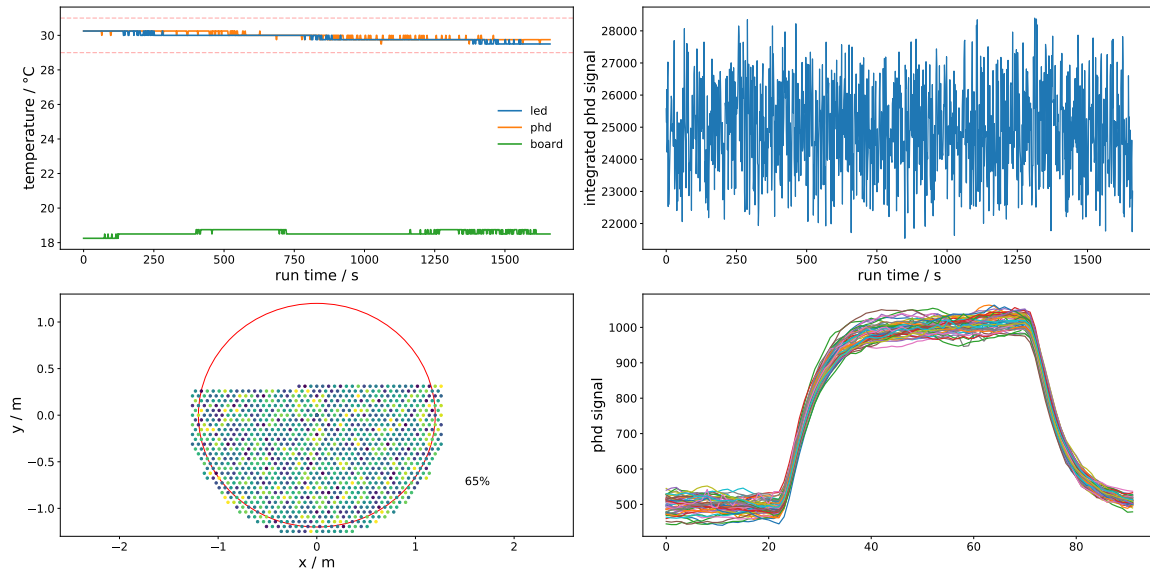


Figure 4.4: XY-Scanner progress display. Top left: temperature monitoring, top right: integrated photodiode signal for each pulse, bottom left: progress of grid with the integrated photodiode signal color-coded and bottom right: the shape of the last 50 photodiode pulses.

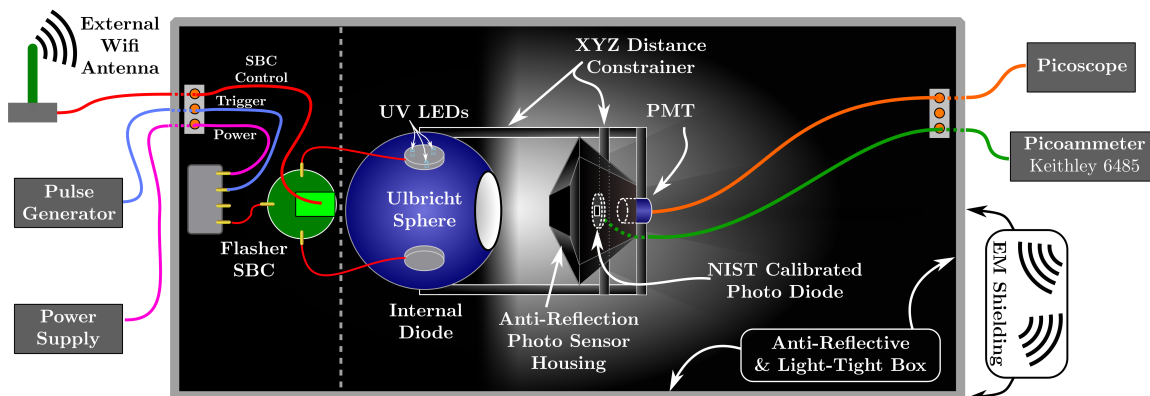


Figure 4.5: Schematic drawing of the XY-Scanner calibration bench at the university of Wuppertal [93].

for the temperature to level out at $\sim 30^\circ$. The other three panels show data from the internal photodiode. The top right panel shows the integrated signal per flash over time, on the bottom left the same information is color-coded into the progress of a run. The bottom right panel shows the shape of the last 50 pulses. This does not track the quality of the data taken with the telescope but is meant to easily detect mistakes from the setup.

4.1.1 Calibration

The calibration of the light source of the XY-Scanner is currently developed by the astroparticle group at the Department for Mathematics and Science of the University of Wuppertal [93]. A schematic drawing of the calibration bench is shown in Fig. 4.5. In a light-tight and electromagnetically shielded box, the flux parallel to the optical axis of the sphere is measured



Figure 4.6: Test stand in Olomouc. The horizontal linear stage and the rotational stage is in the foot for the sphere. The vertical linear stage is attached to the detector, which consists of a SiPM behind a double pinhole. The second rotation is done by rotating the sphere in its mount. [95]

with a calibrated photodiode and a PMT. The photodiode and the PMT are inside an anti-reflection housing which only lets in direct light from the sphere, but blocks most of the light reflected from anywhere else inside of the calibration bench. All surfaces, which are visible from the photodiode or the PMT, are painted black. The response of the photodiode is too slow to measure individual $5 \mu\text{s}$ pulses from the sphere at 1 Hz ². To simulate continuous light the pulse frequency is changed from 1 Hz to 100 Hz . The PMT is used to correct the photodiode measurement for the on/off ratio of the LED. The PMT is also used to correct for deformation in the pulse shape between the two pulsing frequencies. The pulse shape is recorded both at 1 Hz and 100 Hz and the signal in the photodiode corrected correspondingly.

A preliminary calibration of the Karlsruhe sphere in Wuppertal yielded the number of photons per pulse to be [94]:

$$n_{\gamma} = (2.157 \pm 0.083) \times 10^9, \quad (4.1)$$

for an LED current of 2.7 mA and a $5 \mu\text{s}$ pulse. At the time of writing, they claim a systematic uncertainty on the calibration of the sphere of 4% , including an unaccounted error of 3% . This number will be used below for a preliminary calibration of an Auger telescope.

It is yet to be decided, if the light source should be calibrated in Europe before and after each measurement campaign and then be transported back and forth in hand luggage, or if the final design of the calibration stand will be brought to Malargüe. Both options are viable, as the integrating sphere fits into hand luggage and, thus, is easy to transport, see Fig. B.5.

4.1.2 Characterization

As mentioned above, the light source for the calibration has to be a Lambertian emitter. The measurement of deviations from the Lambertian emission spectrum is done at RCPTM³, Palacký University Olomouc. Deviations were expected as the Karlsruhe sphere is a general-purpose sphere [86], and does not have the optimal ratio of sphere to exit port diameter. These kinds of spheres are usually used for measuring light coming from a light source outside of the sphere. Because of the size of the exit port, the internal baffle is visible already at small angles to the optical axis, which is the main reason for the inhomogeneities. Using a bigger sphere would solve this problem but it would also be heavier and would not fit into the aperture box. A smaller exit port would increase the number of positions in the aperture

² roughly the pulse frequency during measurements for the FD calibration ³ Regional Centre of Advanced Technologies and Materials

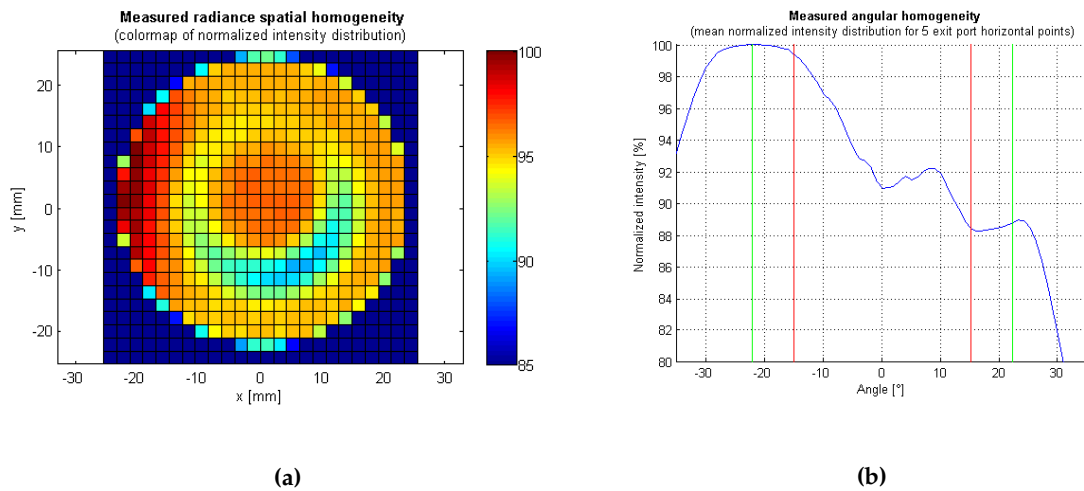


Figure 4.7: (a) spatial and (b) angular homogeneity of the Karlsruhe sphere [87].

and is thus not favorable either. Both options are discussed in Section 5.2. In the test stand in Olomouc, both the spatial and angular homogeneity are measured. This is automated with two linear and one rotational stage. The needed second rotational axis is done by hand. The detector is a Silicon Photomultiplier (SiPM), 20 cm away from the exit port. In front of the SiPM is a double pin hole with 2 mm diameter and 10 cm length. This reduces the seen area in the exit port to a spot of 6 mm diameter. The angular homogeneity is measured at five characteristic positions in the exit port: One at the center and one in each direction with 15 mm distance [87]. Pictures of the test stand are shown in Fig. 4.6.

The measured spatial and angular homogeneity for the Karlsruhe sphere, used in most of the measurements presented in this work, can be found in Fig. 4.7. The circular structure in the spatial homogeneity plot originates from the plug in the fourth port opposite to the exit port. There is a small gap between the sphere and the plug which decreases the reflectivity at this point. The gap is asymmetrical and can be seen in Fig. 4.8(a) close to the bottom left border of the exit port. Additionally, there is a hot spot on the left side of the exit port. It is opposite to the position of the LED head in this measurement and is caused by the first reflection inside the sphere. The main effect in the angular homogeneity plot is a shadow from the baffle inside the sphere, which reduces the light intensity in this direction. The angular homogeneity was measured in three orientations at 0° , 45° and 90° to the plane defined by the exit port and the LED position. The measurement at 0° is shown in Fig. 4.7(b). For this angle, the angular scan crosses the baffle and thus the effect is the largest. The normalized and averaged intensity for the five positions in the exit port is plotted, it drops by 12% when the scan crosses the baffle. For the measurements at 45° it drops by 8% and at 90° ⁴ the angular homogeneity is within 2%. Important for the measurements at the telescopes is the angular range inside the green and red lines, indicated in Fig. 4.7(b). The green line is at 15° which corresponds to the FoV of a telescope. The red line is at 22° , which corresponds to the angle of the PMTs in the corners⁵ of the camera to the optical axis of the telescope. Therefore, it is favorable to have the direction with the worst emission properties, i.e. the 0° plane as defined above, either in the horizontal or vertical plane, as the instrumented area in angular distance is smallest there. The influence these inhomogeneities measured in the laboratory have on the calibration measurements of the FD are shown in Section 5.4.

⁴ here the angular scan does not cross the baffle ⁵ 15° vertically and horizontally

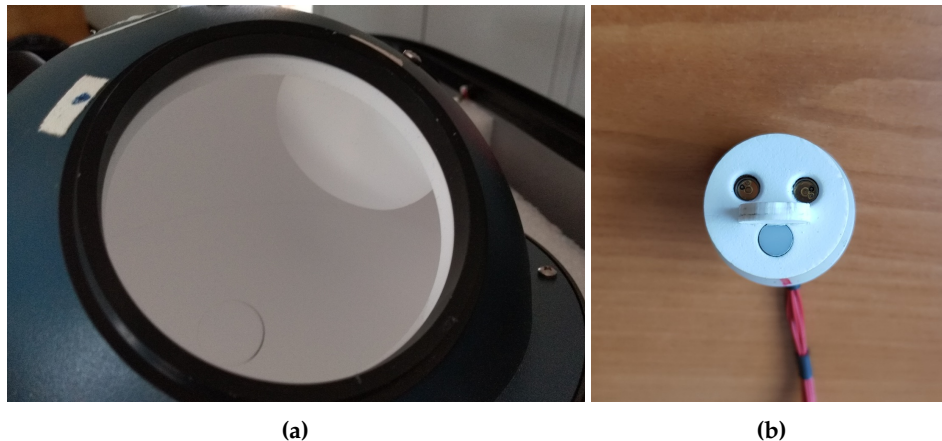


Figure 4.8: (a) internal baffle of the Karlsruhe sphere (lighter area in the top right of the port) and (b) upgraded baffle directly on the LED head and a diffuser masking the active LED (2) for the Czech sphere [87].

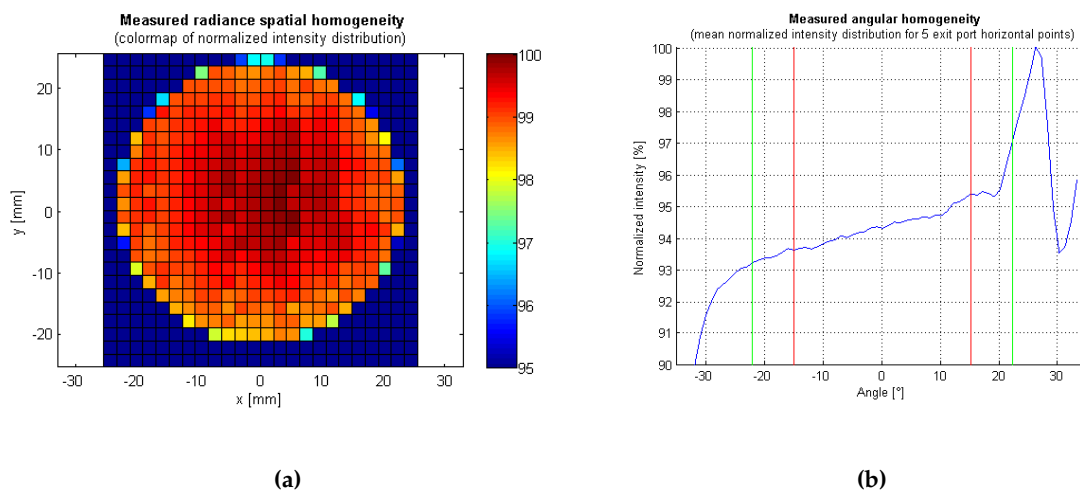


Figure 4.9: (a) spatial and (b) angular homogeneity of the upgraded sphere from Olomouc [87].

Another area of work at the University of Olomouc is to design an optimized sphere, called “Czech sphere” in the following. The main effort is to improve the baffle design inside of the sphere. Instead of the large baffle halfway in between the LED and the exit port, a smaller baffle is attached directly to the LED head. Pictures of the original and the new baffle are shown in Fig. 4.8. The new baffle blocks only the photons coming from LED 2, which is used for the actual calibration measurements, the light from the other two LEDs is unaffected. This reduces the shadow seen before. Additionally, a diffuser is added to LED 2 to decrease the influence of production inaccuracies of the LED.

The improvement in the homogeneity measurements can be seen in Fig. 4.9. The Czech sphere does not have the fourth port opposite to the exit port, eliminating the aforementioned inefficiency with the gap. Overall a clear improvement compared to the measurements of the Karlsruhe sphere can be seen. For the angular measurements the worst direction, where the scan is in direction of the LED head, is shown. The peak in the intensity is when the detector looks at the sphere surface around the LED, however, this is outside the

15° FoV of the telescope camera. The inhomogeneity, which can be seen by the camera of a telescope, is below 2%. This is comparable to the inhomogeneity in the other two directions for the whole range up to 22°. A previous prototype of the Czech sphere, without the diffuser at the LED, was also tested at a telescope, the results are shown in Section 5.4. There, the anisotropy, compared to the Karlsruhe sphere, was decreased by a factor of three, the diffuser is expected to decrease the anisotropy further by another factor of two.

4.2 The Scanner

The second component of the new method to calibrate the fluorescence telescopes is the machinery to move the light source through the aperture. It needs to be able to move the sphere in two dimensions. The installed system is provided by the company Igus [96] and is commonly used in 3D printing and other manufacturing processes. It consists of two independent linear stages. The vertical direction (y-axis in the following) has two tracks, permanently mounted on the left and the right of the UV-filters. As these remain in place and are exposed to dust and other environmental influences at night time, it is advantageous that the system does not need any grease. A prototype for a cover of the tracks exists and is currently being tested in the field. Without the cover, however, no cleaning measures were necessary before operation, after half a year of exposure to the Argentinian pampa. The motor to move the y-axis is located in the bottom center of the aperture box. As electromagnetic waves do influence the flasher electronics, this motor has a mechanical brake, which has to be held open actively to move the axis. No current is needed when the system does not move. To minimize the path in the vertical direction, the grid of flasher positions is processed in rows. The x-axis is mounted on the sleds of the y-axes. For this axis the motor is attached to the right-hand end of the axis, no break is needed here. The x-axis is only mounted for measurements, there are fewer x-axes than systems total, this reduces the overall cost. For mounting and unmounting of the x-axis only four screws are needed. This can be easily done with two persons on site. A test at night-time, with dim red lights only, unmounting of the sphere and the x-axis and mounting on a different telescope took less than 20 minutes, including the cabling and a short functionality test. This is short enough to reach the goal of being able to calibrate three telescopes in one night. Multiple x-axes and electronic boxes further reduce the needed time. A picture of a complete XY-Scanner is shown in Fig. 4.10.

The electronics needed to steer the XY-Scanner is assembled into a box which gets mounted on the right side of the aperture box, as shown in Fig. 4.10. This includes the power supply and controllers for the x and y motors. Both the x- and y-axis are equipped with stepper motors and are self-correcting. For the absolute positioning, reference sensors are used. The positioning of the scanner is precise in the sub mm range, which is better than needed for this task. The steering software runs on a Raspberry Pi, which is also built into the electronics box. Likewise, the board to distribute the trigger signal to the light source and the telescope is built into this box. The cable going to the light source is only for power and the trigger signal. The communication with the flasher board is done via WiFi, therefore a router is put into the aperture box as well. Early tests with the router inside of the FD building led to a rather unstable connection. As most of the electronic parts have status LEDs the box is light-tight.

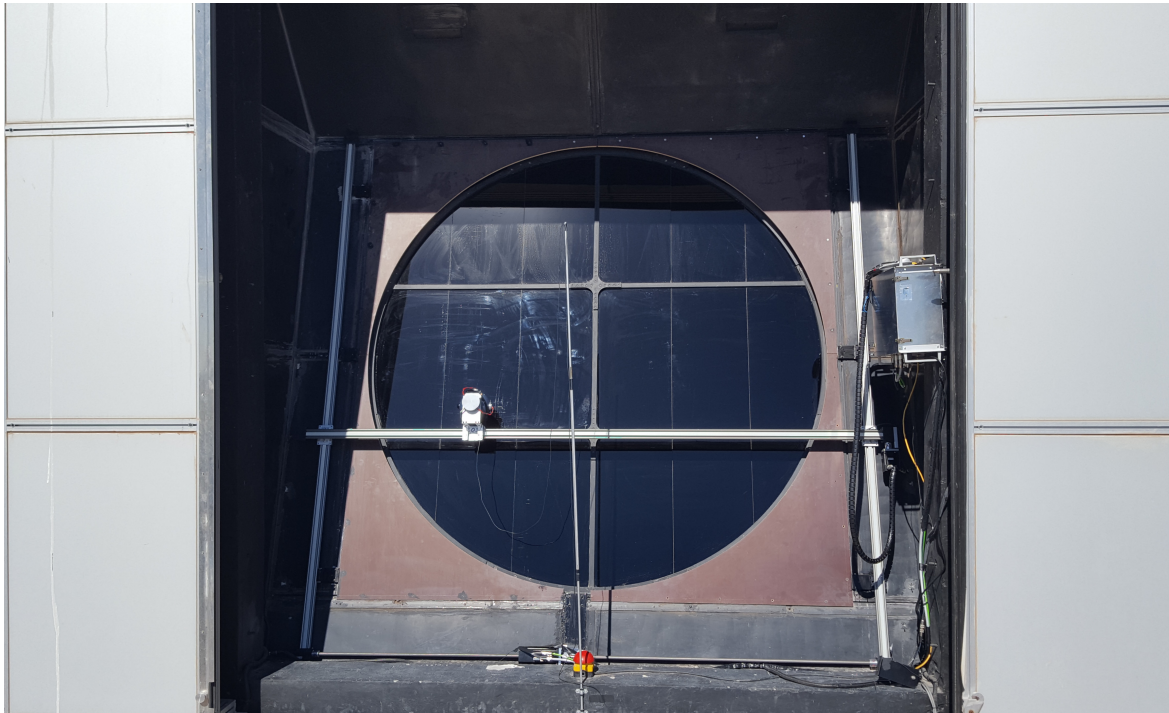


Figure 4.10: The full XY-Scanner mounted at LL bay 4. The motor for the y-axis is visible on the left behind the red emergency stop bottom. The cables to the x-axis motor are bundled to avoid entanglement, as the y-axis must be able to move. For the same reason, the power cable to the sphere is attached to a rod in the center of the aperture box. The aluminum box on the right side houses all the needed electronics, on top (hardly visible) is the WiFi- router.

CHAPTER

5

First Results from the XY-Scanner

Contents

5.1	Analysis	50
5.1.1	Pulse Finder	51
5.1.2	Normalization	52
5.1.3	Simulation	53
5.1.4	Relative Calibration	54
5.1.5	Single Flashes	55
5.2	Optimal Grid for Calibration	57
5.2.1	Shape of the Grid	57
5.2.2	Distance between the Positions	59
5.2.3	Size of the Exit Port	61
5.2.4	Distance to the UV Filter	62
5.2.5	Offset	63
5.2.6	Conclusion	63
5.3	Reproducibility	63
5.3.1	Short Time-Scale	63
5.3.2	Long Time-Scale	64
5.3.3	Dust Layers on Optical Components	65
5.4	Isotropy of the Light Source	68
5.4.1	Hardware Changes	69
5.4.2	Tilting of the Sphere	69
5.5	Relative Calibration of Telescopes	71

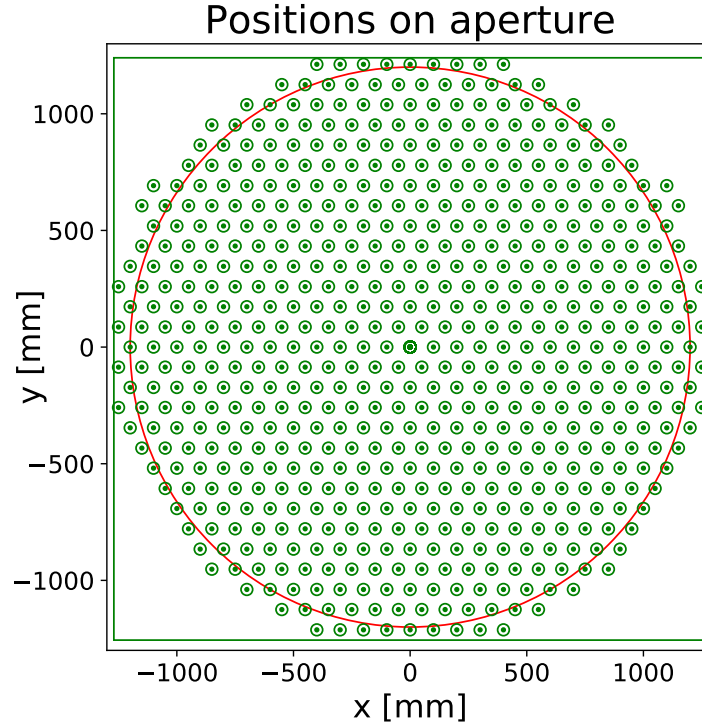


Figure 5.1: Example of a grid of positions used in the measurements with a radius of 1.3 m and a spacing of 10 cm. The green box illustrates the maximum position in x and y direction.

This chapter is about the results from the first three measurement campaigns with the new end-to-end calibration method for fluorescence telescopes, the XY-Scanner. These measurements and accompanying simulations are used to evaluate the performance and systematic uncertainties of the new calibration method. In three campaigns XY-Scanners were built at nine telescopes, of which measurements were taken at seven. These include measurements with different spacing, an example for a grid used in the measurements is shown in Fig. 5.1. Specific measurements were taken to determine the reproducibility of the method and the homogeneity of the light source. A complete logbook of all XY-Scanner measurements with dates, run numbers, and comments on what was measured, can be found in Appendix A.1.

Whenever a plot in the shape of the camera of a fluorescence telescope is shown, the layout of the pixels is as if one would look at the backside of the camera. The numbering scheme of the pixels on the camera was shown in Fig. 2.13. This is different from the way those plots are usually shown for air shower measurements. There, the plots are inverted to see the air shower going towards ground.

5.1 Analysis

The calibration constants for the FD are the conversion from photons at the aperture to ADC counts in the camera:

$$C_{\text{Cal}} = \frac{N_{\gamma, \text{Ap}}}{\text{ADC}} \quad (5.1)$$

A new pulse-finding algorithm adapted to the known shape of calibration pulses, and the conversion from photons emitted from the light source of the XY-Scanner to photons a PMT

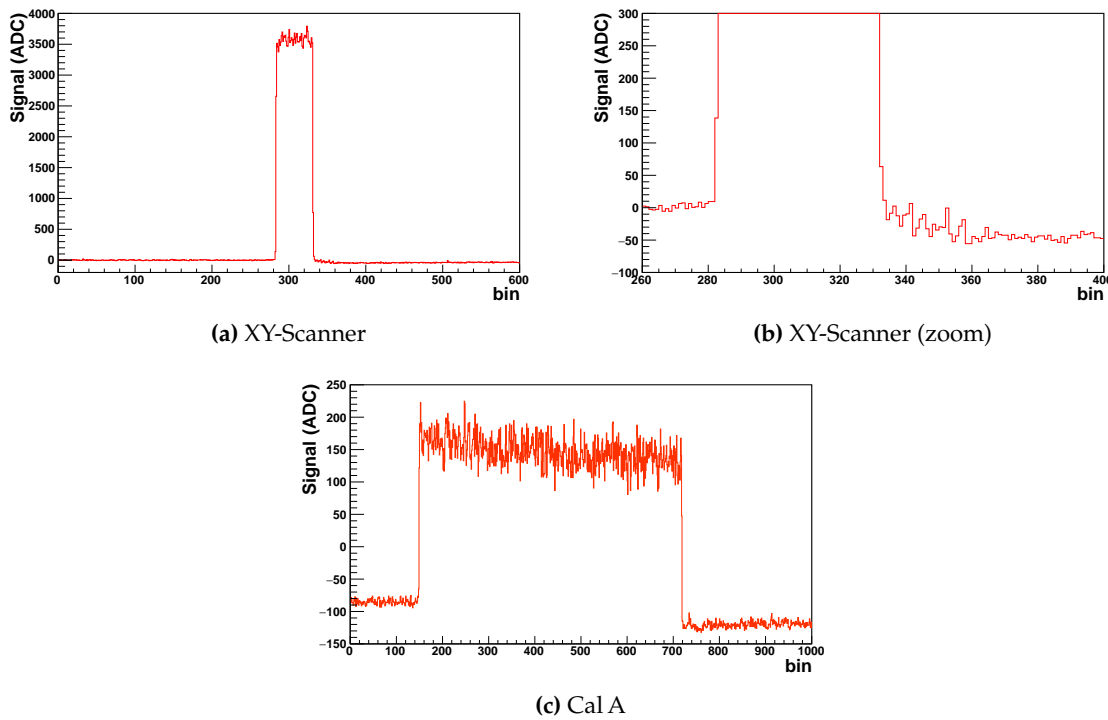


Figure 5.2: Pulse shapes of an XY-Scanner and Cal A flash.

of the camera should see, are described below. To be able to compare two XY-Scanner runs, the results have to be corrected for the drift of the sensitivity of the PMTs. Therefore, Cal A measurements were taken before and after each measurement with the XY-Scanner. At the end of this section, pictures of single flashes from the XY-Scanner are shown. Given the special geometry of the XY-Scanner, shadows of the optical components of the telescope can be seen. The influence of missing positions on the results of the calibration analysis is briefly discussed.

5.1.1 Pulse Finder

The new pulse-finding algorithm utilizes the known shape of the light pulses from the XY-Scanner. A pulse from the XY-Scanner is rectangular and $5\ \mu\text{s}$ long, roughly around bin 300. A plot of an XY-Scanner pulse is shown in Fig. 5.2(a). As the pulses are higher and broader, compared to the pulses from air shower measurements¹, undershoot and afterpulsing are a much bigger problem, as can be seen in Fig. 5.2(b). The standard FD pulse finder in Offline identifies the afterpulsing as part of the pulse, which can broaden the reconstructed pulse by up to $3\ \mu\text{s}$. The new pulse-finding algorithm utilizes the known length of the pulse to cut away the afterpulsing. The amount of afterpulsing was found to be of the order of 1–2% in drum measurements [97]. An example of a pulse from Cal A measurements is shown in Fig. 5.2(c), the same pulse-finding method can be used. The only difference is, that the Cal A pulses show some fluctuation in the pulse length, the first bin with signal below zero is used for the end of the pulse. Afterpulsing, which happens during the pulse, is not corrected for, as it is done for air shower measurements.

¹ for showers far away from the telescope, the pulses can be equally broad but then they are much smaller

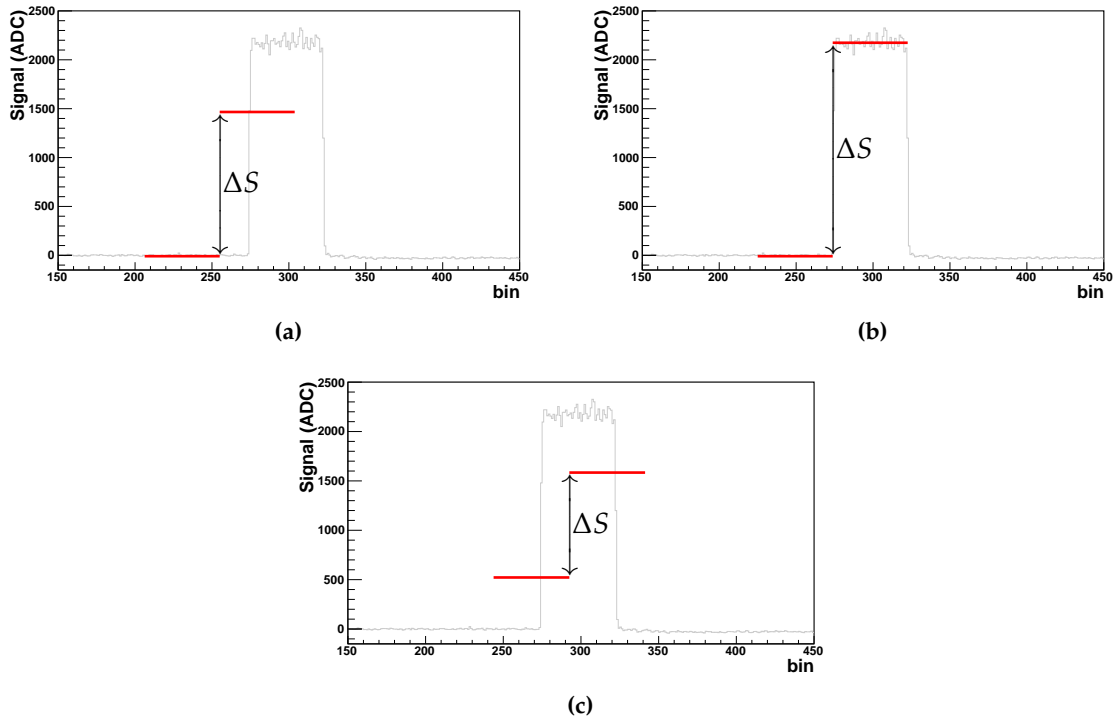


Figure 5.3: Visualization of the new pulse finding algorithm.

The pulses from the XY-Scanner are around bin 300, therefore the new algorithm does not search on the whole trace. In one flash, the beginning of the pulse is at the same position for all pixels. Thus the beginning of the pulse can be searched for by finding a step in all traces. The sum of the signal is formed over two areas of 50 bins², with one bin left out in between. This one bin accounts for the broadening of the pulse by the electronics. When this one bin is at the rising flank of the pulse, the difference between the two areas, ΔS , is the largest. A visualization of the algorithm is shown in Fig. 5.3.

After the location of the pulse in the trace is found, the integral is corrected for undershoot. The baseline after the pulse is calculated as the average of 30 bins, with a distance of 30 bins³ to the end of the pulse to evade afterpulsing. The error introduced by this distance is negligible because of the slow relaxation of the baseline. The correction is done using a linear interpolation of the baseline before and after the pulse.

5.1.2 Normalization

For the drum, the conversion from photons at the aperture to photons a PMT sees was relatively easy. For a sufficiently large drum, the photon density and emission spectrum are the same at the surface of the drum and in the aperture of the telescope. For the XY-Scanner, the same relation holds for the area of the grid of positions, but the photon density has to be corrected for the fraction of illuminated area f . The photon flux in the illuminated area A_{illum} is:

$$\phi = \frac{N_{\gamma}}{A_{\text{illum}} \times \pi \times (1 - \cos \theta_{\text{max}}^2)}, \quad (5.2)$$

² one bin has a width of 100 ns, for HEAT the width is only 50 ns, therefore 100 bins are taken ³ 60 for HEAT

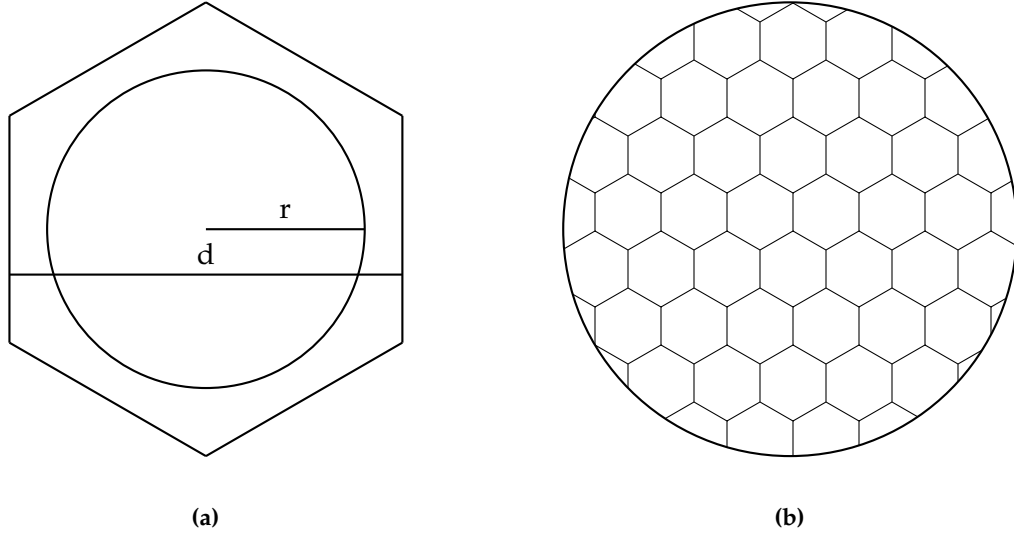


Figure 5.4: (a) Drawing of the light spot of radius r in the unitary cell of a hexagonal grid with side length l (b) repetition of the unitary cell in the hexagonal grid

with $A_{\text{illum}} = A_{\text{flash}} \times N_{\text{flash}}$ being the product of the illuminated area of one flash and the number of positions. N_{γ} is the total number of emitted photons, correspondingly given as $N_{\text{flash}} \times N_{\gamma, \text{flash}}$. The rest of the formula is the integration over the Lambertian emission spectrum, θ_{max} is 90° in measurements or the maximum angle used in simulations. The number of photons a PMT sees is obtained by multiplying the flux with the area of the aperture A_{Aperture} , corrected for the fraction of the illuminated area f

$$N_{\gamma, \text{Pixel}} = \phi \times A_{\text{Aperture}} \times f. \quad (5.3)$$

For a hexagonal grid the fraction of the illuminated area is given as

$$f = \frac{2 \cdot \pi \cdot r^2}{\sqrt{3} \cdot d^2}. \quad (5.4)$$

Where r is the radius of the exit port of the sphere and d is the step width of the grid. An illustration is shown in Fig. 5.4, it is assumed, that truncated positions at the border of the aperture average out and do not affect f .

It is crucial for this calculation that the density of positions is constant over the whole area. Thus the area of the grid has to be larger than the aperture, to avoid underdensities at the border. Additionally positions outside the aperture of the telescope, however, are not a problem. As the number of positions is both in the total number of photons and in the total area, additional positions do not change the flux.

5.1.3 Simulation

For the simulation of the XY-Scanner, the drum simulation module in Offline was modified. The main difference is that the plane in which the photons are generated was moved from the aperture to outside of the UV filter. Generating the photons in the aperture is correct for a uniformly distributed flux and if the UV filter is sufficiently larger than the aperture. For the XY-Scanner the photons are distributed over a grid of positions, for a correct description this grid has to be outside of the UV filter. The adjustable parameters of the grid are:

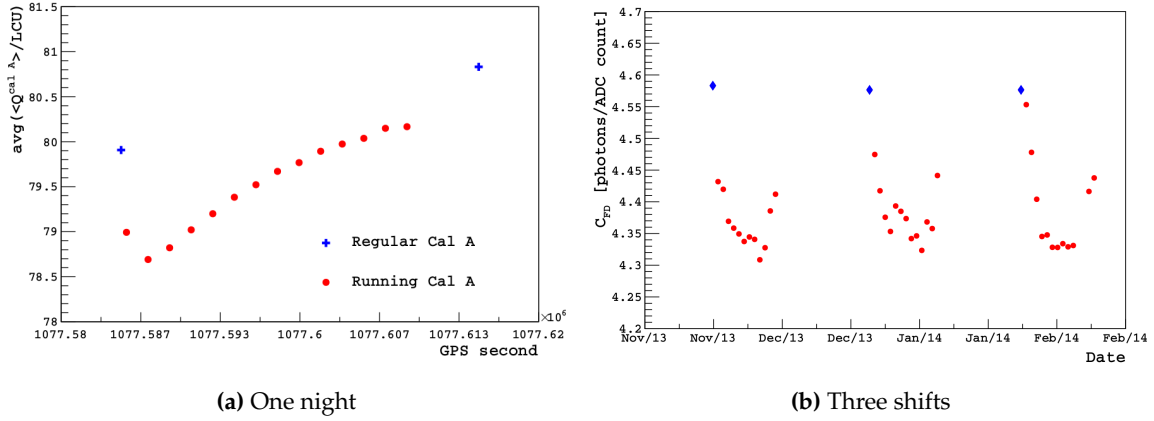


Figure 5.5: Drift of FD calibration over the course of (a) one night and (b) three shifts. Regular Cal A is done with closed shutters at the beginning and end of each night. Running Cal A is done with open shutters during normal data taking. In (b) the last calibration of each night is plotted, the blue marker is the beginning of a shift (taken from [49]).

- Radius of the grid
- Cuts in x- and y-direction
- Distance between positions
- Radius of the exit port of the sphere
- Distance to the filter
- Tilt of the light source in two directions
- Shift of the grid as a whole

The analysis of the simulations uses the same normalization as described above. N_γ in Eq. (5.2) is replaced by the total number of generated photons.

5.1.4 Relative Calibration

A note on the relative difference used in most of the following plots. In simulations where an XY-Scanner simulation is compared to a drum simulation, or also in reconstruction when a subset of a run is compared to the complete run, the following formula is used

$$R_{AB} = \frac{A - B}{B}, \quad (5.5)$$

where B is the drum simulation, or the complete run, and therefore is considered to be the correct result. When two different measurements are compared we do not know which one is correct and the average is used in the denominator

$$r_{AB} = \frac{2(A - B)}{A + B}. \quad (5.6)$$

Over the course of a shift, and also during a night, the sensitivity of the PMTs is changing. This change in sensitivity is tracked with continuous Cal A measurements during the

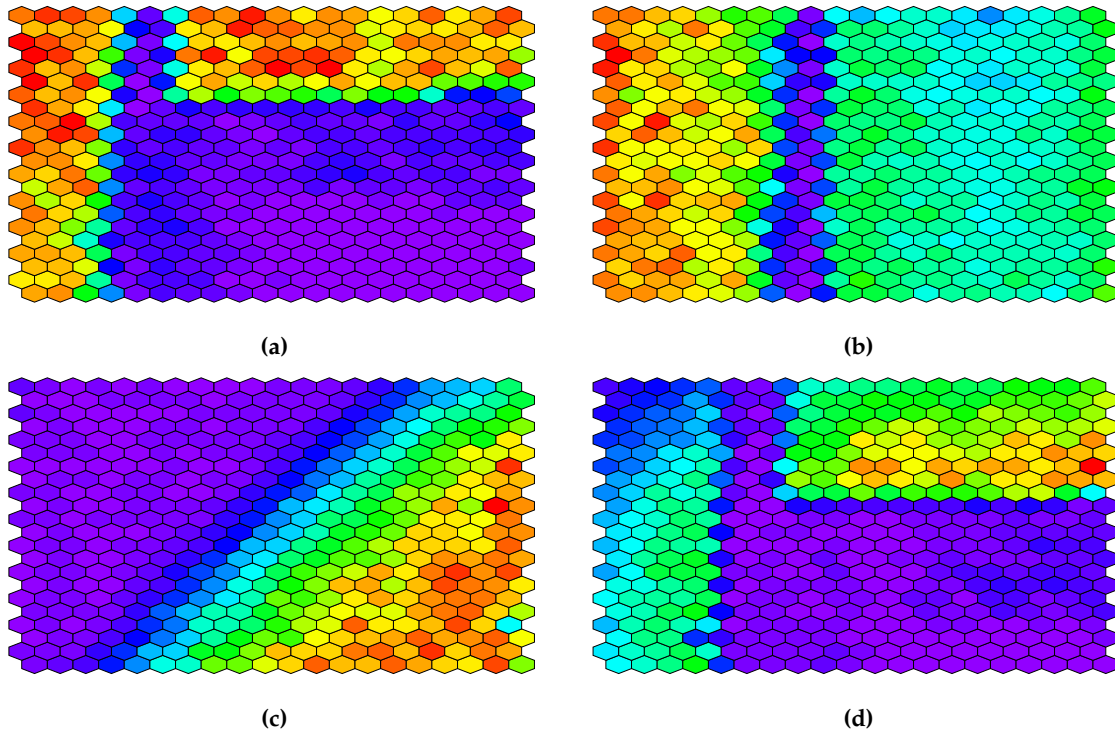


Figure 5.6: Examples for measured images in the camera for a single flash at different positions. The color-coding is the amplitude of the signal from large (red) to roughly zero (purple). The subfigures show different shadows: (a) shows a part of the camera shadow (b) shows the shadow from one of the feet of the camera and fainter shadow on the right from the UV-filter holding structure (c) shows a position at the edge of the aperture (d) shows a combination of many shadows, worth mentioning is the additional blue pixel in the bottom left close to the camera shadow which comes from the Cal B light source.

night [49]. For an impression on how much the calibration changes over a shift/night see Fig. 5.5. As can be seen, the drift is $\sim 2.5\%$ over the course of a night, but strongest at the beginning of the night. A similar trend of about 6% is visible on the time scale of a shift.

To compare two calibration runs with the XY-Scanner, the results have to be corrected for the drift of the calibration. Therefore, Cal A measurements are taken before and after each XY-Scanner measurement. They are used to correct one of the two XY-Scanner measurements. Mathematically, the term B in Eq. (5.6) is replaced by

$$\frac{S_{\text{CalA},B}}{S_{\text{CalA},A}} \times B, \quad (5.7)$$

where S_{CalA} is the pulse height of the Cal A measurement. The size of this correction is shown in an example in Section 5.3.

5.1.5 Single Flashes

Using a light source much smaller than the aperture we get one fundamental difference to images of air shower or the drum calibration method. For many positions in the aperture, PMTs are shadowed by optical components of the telescope and do not receive any direct light. These components are the camera and its support structure, the aperture and the

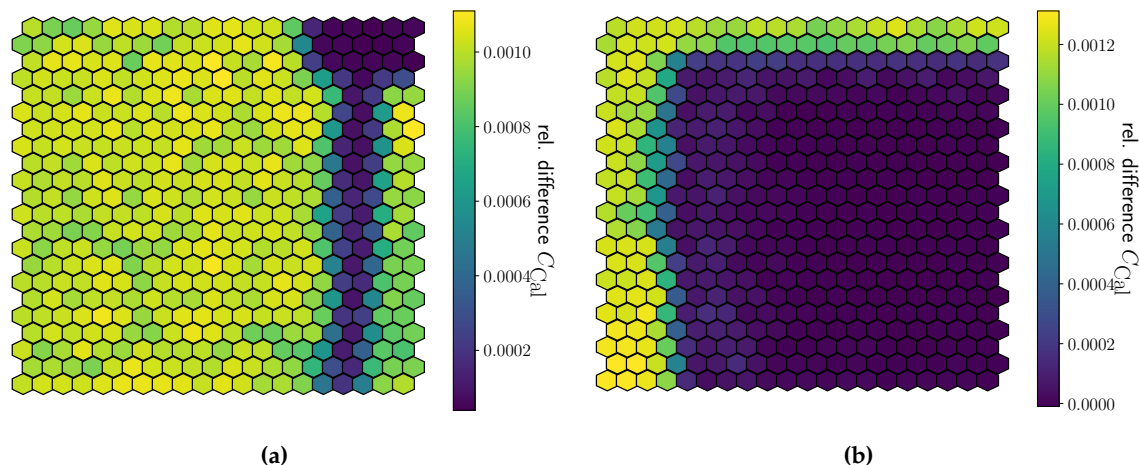


Figure 5.7: Examples for the influence of missing positions on the calibration constants. The comparison to the complete run reproduces the missing image. Missing shadows do not change the calibration constants but the missing pulses increase them. The structure of the mirror is visible in (a).

support structure of the UV filters. As the support bars of the UV filters are thinner than the diameter of the light source, those shadows are not complete but dimmer regions on the camera. At the same time, they are closer to the light source, which makes the shadow broader. Examples of images with various shadows are shown in Fig. 5.6. In the analysis of the calibration, the sum over all position is taken and thus the shadows are averaged out. The difference to air showers measurements, where mainly one pixel is illuminated at a time, is the same for both methods. For the averaging over all positions to be correct, it is important, that the grid of positions spans uniformly over the whole aperture. The optimization of this grid is described below.

Sometimes during the measurements it happens, that a calibration run is split into two or more files. Typically, this happened when the connection to the flasher board was lost and the scanner stopped. In this situation, a bit of carefulness is needed to make sure no position is missing or doubled. The effect of missing positions is shown in Fig. 5.7. In comparison to a complete run, the actual shape of the missing image in the camera can be seen. For shadowed regions the change in the calibration constant is negligible, the missing pulses, however, change the calibration. The amplitude of this effect is the missing signal over the total signal, which roughly scales with the total number of positions. In the case of doubled positions, the sign would change. As the quality of the last flash before a crash is questionable, the new run was usually started at the same position. The surplus flash has to be removed in the analysis.

As a side remark: you can see features of the area on the mirror which was illuminated by the missing flash in Fig. 5.7(a). It's most visible in the bottom left corner. The telescope, used in this measurement, is one with a Czech mirror, which consists of smaller hexagonal mirrors. In between the hexagons is a small gap and in the center of a hexagon is a small hole which is needed in the mounting of the mirror segments. Both the gap between two mirror segments and the hole in the middle appear as slightly darker area in Fig. 5.7(a). If you found the center of this hexagon, the others can be found by counting to six pixels in the horizontal and diagonal direction.

5.2 Optimal Grid for Calibration

The XY-Scanner calibration method for fluorescence telescopes uses a grid of positions over the whole aperture. The sum over all those positions is expected to yield a similar result to the old drum calibration method. A hexagonal grid is being used, as this allows for the densest placement of positions over the aperture area, and also allows to process the grid in lines. This minimizes the path in the y-axis, minimizing the time in which the brake has to be kept open. The parameters of the grid which get discussed here are:

- Radius of the grid, R
- Cuts in x- and y-direction, $x_{\min, \max}, y_{\min, \max}$
- Distance between positions, d
- Diameter of the exit port of the sphere, D
- Distance to the filter, d_F

These parameters are optimized with two goals in mind. The first one is the accuracy of the calibration and is addressed in the following. The second goal is to keep the measurement time as short as possible as the sensitivity of the PMTs changes throughout the night. This consideration will be addressed in Section 5.3.

5.2.1 Shape of the Grid

The first two parameters to be optimized give two different solutions for the outer shape of the grid. The simple solution would be to use the largest possible full circle. The other option is to use a large circle and cut it, to avoid the collision of the light source and the aperture box. This is mainly the case at the top and the bottom of the aperture, at the sides the scanning range is limited by the vertical tracks of the XY-Scanner. Both options are covered in the following paragraphs.

Radius

To check how big the radius of the grid has to be, simulations of XY-Scanner measurements with increasing radius were performed. The mean relative difference in all pixels to a simulation of the drum calibration for each radius is shown in Fig. 5.8(a). The other three plots show the same result from measurements. Here, the comparison with drum measurements is not possible, therefore it was done relative to a reference run⁴. Successively, positions at a larger distance to the center greater than R were removed from the reconstruction. The assumption here is that positions sufficiently far out do not affect the results, as no light from these positions reaches the camera. This assumption is valid as there is hardly any change in the results going from $R = 130$ cm to $R = 124$ cm. The difference between the simulation and the measurement comes from an idealized description of the point spread function of the telescopes. In these simulations, the influence of dust layers on optical components is not considered. Figs. 5.8(c) and 5.8(d) both show the same example of a radius of 116 cm, which is the maximum R for the XY-Scanner used in the first measurement campaign. The mean

⁴ $r = 130$ cm and cuts in x and y direction as specified in Table B.1 for HEAT 1.

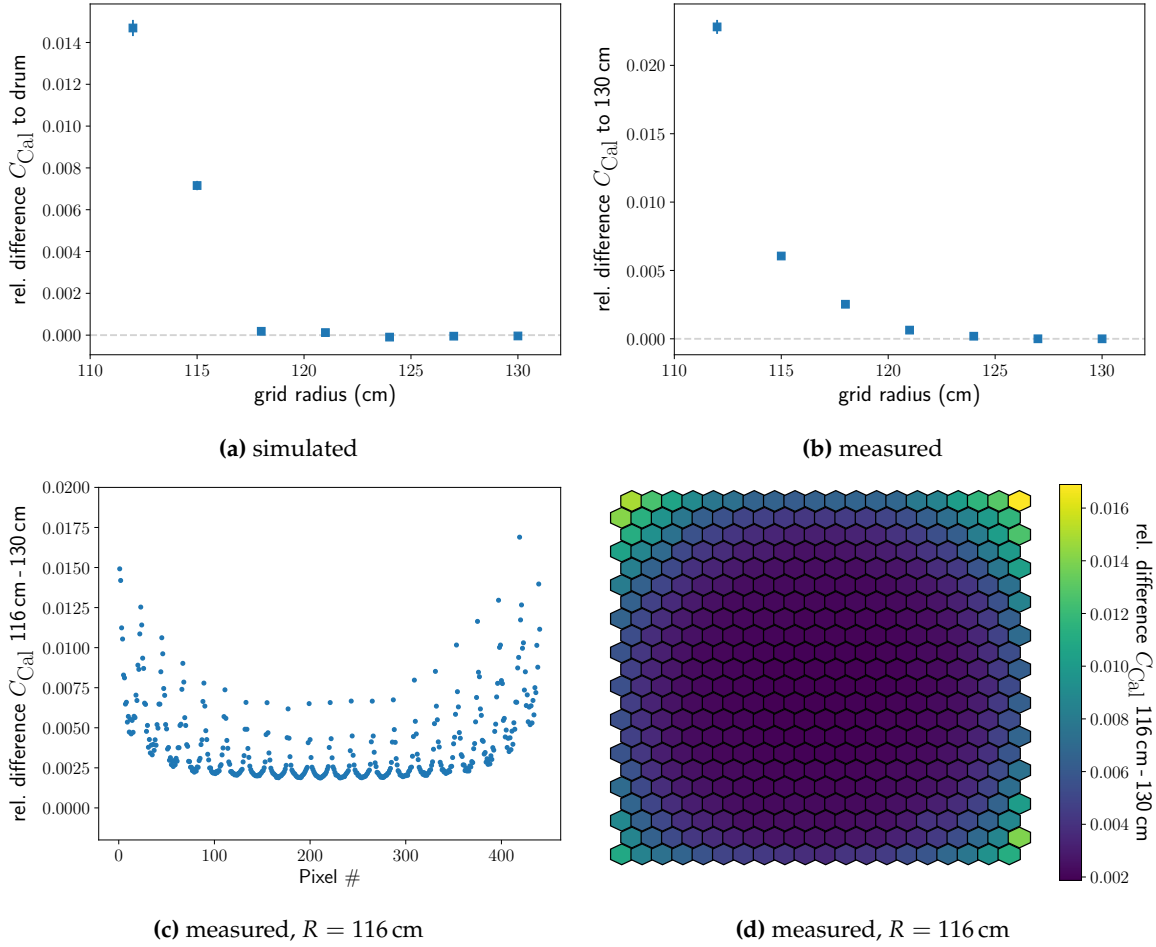


Figure 5.8: Deviations in the XY-Scanner calibration as a function of the grid radius in (a) simulations and (b) measurements. (c) and (d) show one measured example at the size of the first prototype.

relative difference to the reference run is already below 0.5% but up to $\sim 2\%$ for single pixels. This was the main reason to build bigger XY-Scanners with longer tracks, starting from the second campaign on. The 2D plot shows that the pixels with a larger difference to the full run are on the edges of the camera. From the positions at the edges of the aperture, only the photons with a high angle to the optical axis of the telescope can reach the camera, and therefore hit a PMT of the outermost columns or rows. For the XY-Scanners built from the second campaign on the maximum radius for a full circle on the filter is ~ 124 cm. For this radius, the deviation to the drum simulation is below 0.1%, even in single pixels.

Cuts

The PMTs do not see photons originating from the whole area of the UV filter, but they see a projection of the aperture to the plane of the UV filter with the viewing angle of each pixel. This angle is 15° to the optical axis for the left and right pixel in the central row⁵, but $\sim 20^\circ$ for pixels in the corners of the camera. Therefore, the grid has to extend further on the diagonal axis, compared to the x- and y-axis. This coincides with the scannable area in

⁵ likewise for the top and bottom pixel in the central column

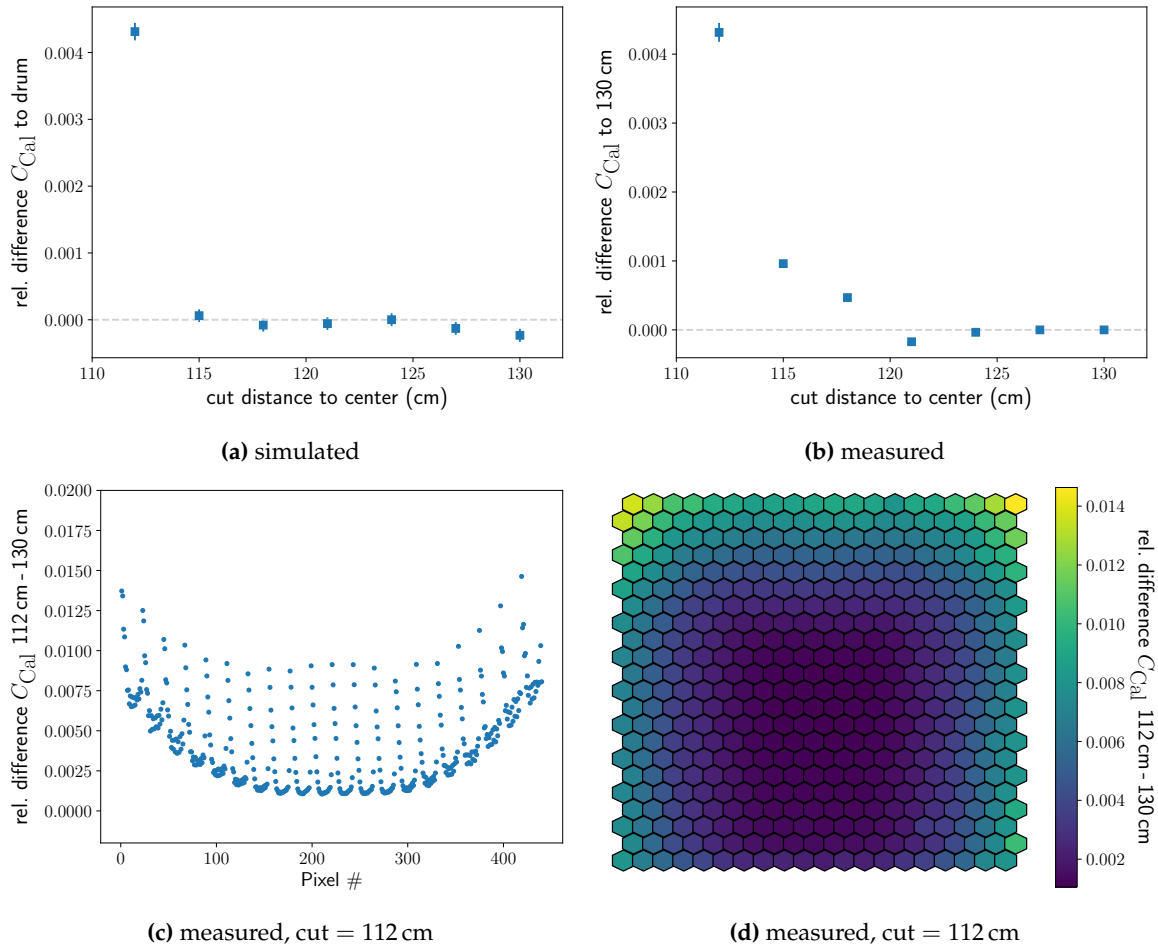


Figure 5.9: Deviations in the XY-Scanner calibration as a function of the cut value in (a) simulations and (b) measurements. (c) and (d) show one measured example with cuts at 112 cm.

the measurements. The scannable distance is smallest in x- and y-direction where the light source collides with the aperture box. Therefore, a grid with a larger radius and cuts to the maximum distance in x and y direction can be used. The cut values for all built XY-Scanners can be found in Table B.1.

The results of the simulations and measurements for this layout are shown in Fig. 5.9. Both are made with a grid radius of 130 cm. In comparison to the results for the simpler layout shown in Fig. 5.8, the deviation to the simulation of the drum, respectively the reference run, is reduced by a factor of ~ 5 . More importantly, with the size of the XY-Scanners built from the second campaign on, we have large enough scanners to only have a negligible bias in our measurements coming from the size of the scannable aperture.

5.2.2 Distance between the Positions

The next parameter to be studied is the distance between two positions in the grid. This has the largest impact on the time needed for one complete scan, as the number of positions depends quadratically on this parameter. In practice one flash every 1.4 seconds was found to be practicable, the maximum readout frequency of the FD is 1 Hz. A lower bound for the

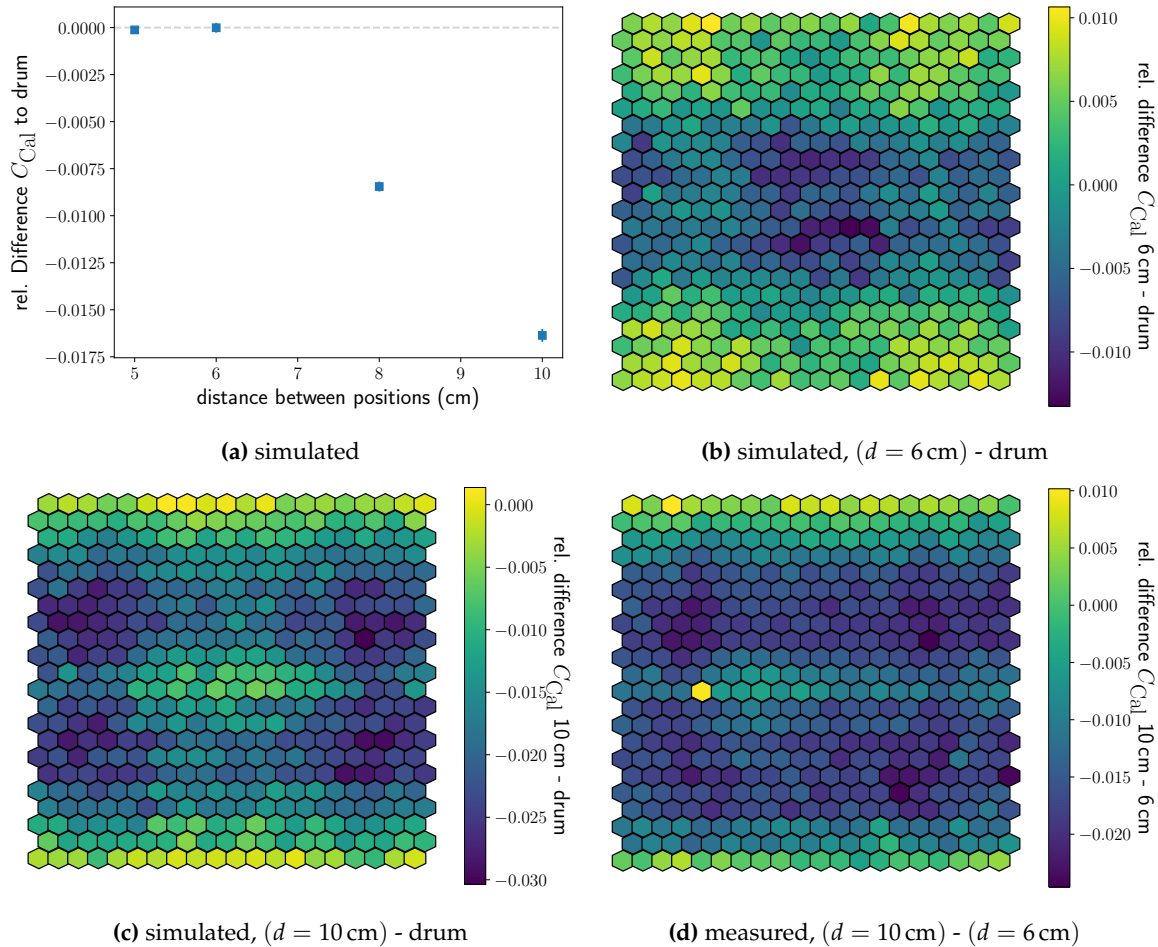


Figure 5.10: Deviations in the XY-Scanner calibration as a function of the distance between positions in simulations (a) with examples for (b) 6 cm and (c) 10 cm and the difference between 6 cm and 10 cm in measurements (d).

distance between positions is the diameter of the exit port. If positions are overlapping it is more complicated to get a constant flux over the whole aperture and the grid of positions has to be bigger to avoid under-densities at the border. In this set of simulations and measurements, the diameter of the exit port was fixed to 5 cm and the distance in between the positions was varied. The results are shown in Fig. 5.10. The results are closest to the drum simulation when the distance between the positions is equal or close to the diameter of the exit port. For larger distances the obtained calibration constants get smaller, indicating that positions with shadows in the camera are lost. Fig. 5.10(b) and Fig. 5.10(c) show the pattern in the camera for 6 cm and 10 cm distance between the positions. The same plots can not be made from measurements, as we do not have the drum as a reference but the difference of the 6 cm and 10 cm distance measurements is shown in Fig. 5.10(d). With the two other plots to compare, most of the effect in the measurements appear to originate from the 10 cm distance run. For a 6 cm distance grid, which was used in most of the test measurements, the deviation in single pixels is up to 1% while the average is still compatible with zero. One calibration run with this 6 cm distance grid takes about 45 min.

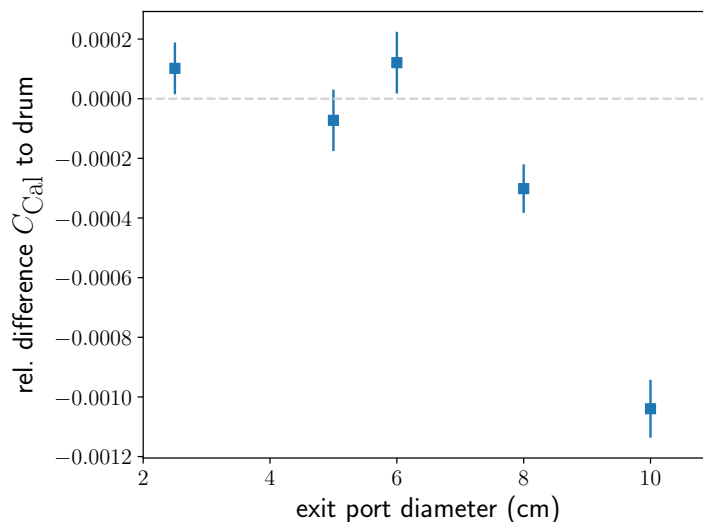


Figure 5.11: Deviations in the XY-Scanner calibration as a function of the exit port diameter. The distance between the positions was changed accordingly.

5.2.3 Size of the Exit Port

The effect on the calibration constants from increasing the distance between the positions of the XY-Scanner can be compensated by adjusting the diameter of the exit port to the distance between the positions. Thus, the optimal condition found above, where the deviation to the drum simulation was smallest when the illuminated circles on the grid touched, can be kept and the number of positions can be reduced. The result of these simulations is shown in Fig. 5.11. Small deviations to the drum simulations appear at a larger exit port diameter, presumably from the growing gaps between the circles on the hexagonal grid and steps at the edge of the grid. As expected the effect is smaller than what was shown in Fig. 5.10. However, in practice going to a higher exit port diameter is an undesirable option. As discussed in Section 4.1.2 the ratio of the sphere diameter to the exit port diameter should be greater than three for a homogeneous light source. Even with the current sphere, we do not meet this condition and the effect this has on calibration measurements at the telescope will be shown below. A bigger exit port would impose the need for a bigger sphere, which would reduce the scannable aperture to avoid collisions with the aperture box. Also, the additional weight increases the torque induced onto the x-axis, which might lead to additional complications in the mechanics of the XY-Scanner.

Measurements were done with 1 and 2 inch port reducers. Both were done with the same distance between the positions of 6 cm for time reasons. Half the distance would have quadrupled the time needed for the run, which then would have been around 3 h. However, the result from these measurements are inconclusive, several effects have an impact here. The sphere would need to be calibrated for each port reducer which until now we did not do, this produces a constant offset. As it will be shown later in Section 5.4 the emission spectrum deviates from that of a Lambertian emitter. The amplitude of this deviation changes with the diameter of the exit port. A third contribution comes from the distance between the positions for the 1 inch measurement. As discussed in the previous section the diameter of the exit port and the distance between the positions should be close. In this case, this requirement is

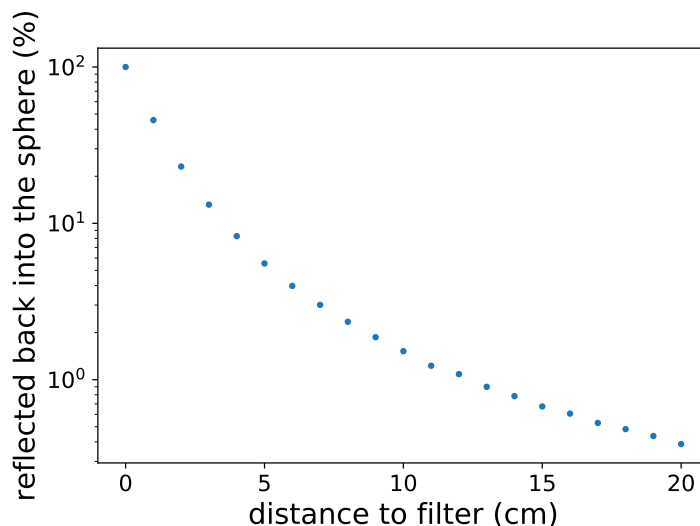


Figure 5.12: Fraction of specular reflection back into the sphere as a function of the distance of the exit port to the UV filter. The closest the sphere can be positioned to the UV filter in the field is 9 cm. Non-specular reflections are ignored in this simulation.

not met. The effects can not be separated. The presumably much longer measurement time needed to reach comparable results disfavors the 1 inch port reducer.

5.2.4 Distance to the UV Filter

This parameter addresses one of the difficulties of the old absolute calibration method. The drum is a big reflecting box mounted on the telescope. Light coming from the drum which is reflected on the UV filters, or in the telescope and left through the filter, is back-reflected from the drum. This problem is well known and needed to be corrected for in the analysis of the drum data [98]. In the case of the XY-Scanner, back-reflected light should be a much smaller problem as the exit port is small compared to the size of the aperture, therefore, photons coming from the inside of the telescope can be neglected⁶. The dominant term should be specular reflection on the UV filter. Fig. 5.12 shows the results of a simulation where the photons from a Lambertian light source get reflected at a plane in x cm distance, with specular reflection only. The closest the light source can be positioned to the filter of the telescope is 9 cm. For this distance the fraction of photons that are reflected back into the sphere is 1.87%. At the wavelength of our LED the reflectivity of the UV filter is around 20% (see Fig. 2.12(b) [39]). Therefore, the amount of photons reflected back into the sphere is $\sim 0.4\%$. This is an upper limit because non-specular reflection, for example on dust particles, is not included in the data-sheet reflectivity. We propose to correct for half of the effect and to add 0.2% to the systematic uncertainty. The effect can be further reduced by increasing the distance between the sphere and the filter of the telescope. The size of the grid would have to be increased accordingly, as this changes the distance to the center of the aperture from which photons can reach the PMTs.

⁶ $\sim \frac{1 \text{ inch}^2}{(1.2 \text{ m})^2}$

5.2.5 Offset

In the field, the XY-Scanner is positioned relative to the support structure of the UV filter, at most at mm precision, see also Fig. 4.1(b). Therefore, it was checked if an off-center placement of the grid changes the results of the analysis. In simulations as well as in measurements no significant change of the calibration constants was found. As long as the scanning pattern is large enough to cover the edges, and the density of positions is constant over the aperture, a constant offset on all the positions does not change the results.

5.2.6 Conclusion

Most of the test measurements were done with a radius of $r = 130$ cm with cuts around 124 cm. A list of the cut values for all XY-Scanner built is shown in Table B.1. The distance between the positions was 6 cm and the port diameter 2 inch, the distance to the UV filters was 9 cm. With these settings, the discretization artifacts are well below 0.01 %, see Fig. 5.9 and the backreflection of photons is ~ 0.4 %, which can be corrected in the analysis. One calibration run takes ~ 45 min, which is short enough to reach the goal of calibrating three telescopes in one night. A full calibration of the FD would then take 9 days and thus easily fit in one FD shift.

5.3 Reproducibility

The reproducibility of the new calibration method has been tested on two different time-scales. Long time-scale means measurements from two different campaigns here. The short time-scale measurements address the stability of the detector during the measurements. As shown above the sensitivity of the PMT is changing throughout a shift/night, each calibration run needs to be short enough to effectively see a stable detector. Different calibration runs can only be compared if they are corrected by surrounding Cal A measurements.

5.3.1 Short Time-Scale

The short time-scale test of the reproducibility of the calibration aims at the drifting of the sensitivity of the PMTs. If the drifting is too large on the time-scale of one run, this would reduce the accuracy of this method drastically. To test it two runs are done consecutively, but the order of the positions on the aperture is reversed. By this, we get the maximum time interval for the positions at the beginning and the minimum for positions at the end of the grid. By design, we illuminate all pixels from all positions, so this should have no impact on the result, but when shadows are taken into account this is no longer the case. With shadows the positions at the borders of the aperture illuminate only the opposite pixels on the camera, therefore we should get the same time structure in the illumination of the pixels. A similar contribution comes from the slightly different part of the scanning area seen by different PMTs, as discussed above. Thus, if the effect from the drifting of the sensitivity is large, one expects to see some structure in the comparison of the two runs.

The results are shown in Fig. 5.13 for two independent measurements. Both times the change in calibration constant is a constant and shows no systematic structure which could come from geometry. However, there are a lot of outliers. Those are suspected to be short-time

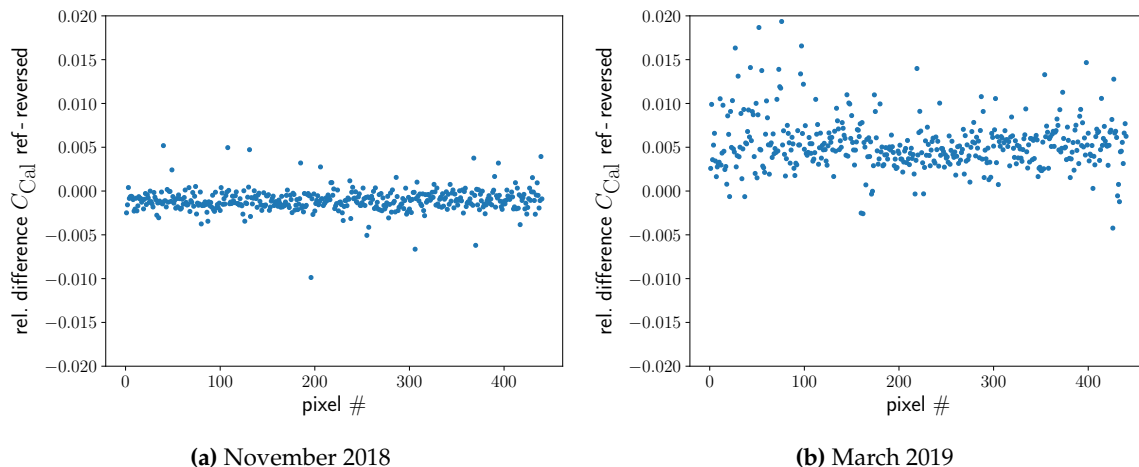


Figure 5.13: Relative difference of calibration constants obtained by one scan upwards and one scan downwards. (a) was taken in November 2018, (b) was taken in April 2019. The main difference is that (a) was taken at the end of a shift and (b) at the beginning.

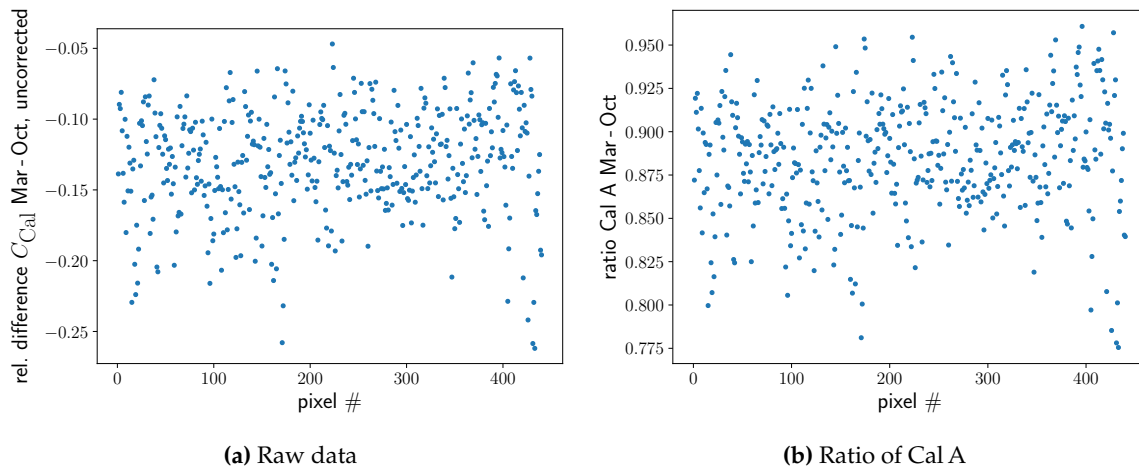


Figure 5.14: (a) uncorrected difference between two XY-Scanner measurements with six months in between, (b) ratio of the Cal A measurements accompanying the XY-Scanner measurements

drifts of single pixels which are therefore not tracked by the intermediate Cal A. Both the number of outliers as well as the offset to zero is considerably larger for the measurements in April of 2019. The main difference to the measurements in November of 2018 is that these measurements were done at the beginning of the shift when the camera is not so stable yet, and the drifting of the calibration is stronger. It is, therefore, important for future measurements to do the XY-Scanner calibration in the middle of an FD-shift. The results of the calibration analysis are reproducible within 0.5 %.

5.3.2 Long Time-Scale

In Fig. 5.14 the uncorrected difference between two XY-Scanner measurements from the first and the second shift is shown, as well as the ratio of the corresponding Cal A measurements. After applying the correction explained above, the remaining difference shown in the upper

example in Fig. 5.15. The effect is bigger than the reproducibility of the method derived at short time-scales. For most of the pixels, the difference is within 2%. The signature shown in Fig. 5.15(a) looks like what one would expect from the accumulation of dust on the mirror. The lower part of the mirror is less inclined and therefore the accumulation of dust is larger, leading to more absorption of photons which would hit the PMTs in the lower rows of the camera. It should be noted here, that inaccuracy in the mounting of the light source can lead to similar effects on the measurements. The effect of tilting the light source will be discussed in Section 5.4.2.

The same comparison was also done for the second and the third campaign. The result for CO 3 are also shown in Fig. 5.15. For the other telescopes measured in both campaigns, this comparison is not possible. At the end of the November 2018 campaign, the flasher electronics was changed⁷, the difference between LED heads has a larger effect and is discussed in Section 5.4.1. For CO 3 the same column structure as in the first measurements is observed. The offset to zero⁸ can be explained by the port reducer being replaced, a direct comparison of the two port reducers was not possible.

5.3.3 Dust Layers on Optical Components

Dust layers on optical components, especially the mirror, are presumably the source of the change in the optical properties of the telescope found above. The accumulation of dust on optical components is a long-known problem for the FD and needs to be included in the calibration. Previous measurements on how dust layers on the mirror and the UV filters change the optical properties of a telescope can be found in [99, 100]. Note, however, that the XY-Scanner is not the ideal device for those measurements, as all pixels are illuminated simultaneously a lot of the information is lost. Scattered photons which are missing in one pixel show up in another. As this happens for all pixels simultaneously it is not separable. For the measurement of the point spread function, a collimated light source is better suited. When only one pixel is illuminated the fraction of scattered light can be measured. Plans for such a light source exist and will be a part of future work. However, the amount of absorbed light is also missing when all pixels are illuminated, and the size of this effect can be determined. In the following XY-Scanner measurements of dust layers on a mirror and UV filters will be discussed.

Dust on a Mirror

The dust layer on a mirror is not uniform because of its shape. It is a spherical mirror, therefore, the inclination depends on the position on the mirror. At the top, the mirror is almost vertical and hardly any dust accumulates, at the bottom, it's much easier for the dust particles to stick to the mirror. The change in calibration constants when a mirror is cleaned is shown in Fig. 5.16, the effect is of order 0–5%. This is compatible with results obtained in [100, 101]

As explained before, the XY-Scanner method is only sensitive to the absorption of photons, the change of the point spread function vanishes in the simultaneous measurement of all pixels. However, the closest we get to the state of only one pixel being illuminated is when large parts of the camera are shadowed. The optimal position of the XY-Scanner for this

⁷ for a finer stepping in LED current ⁸ dust only lessens the signal, thus increases the calibration constant and leads to negative values for the relative difference

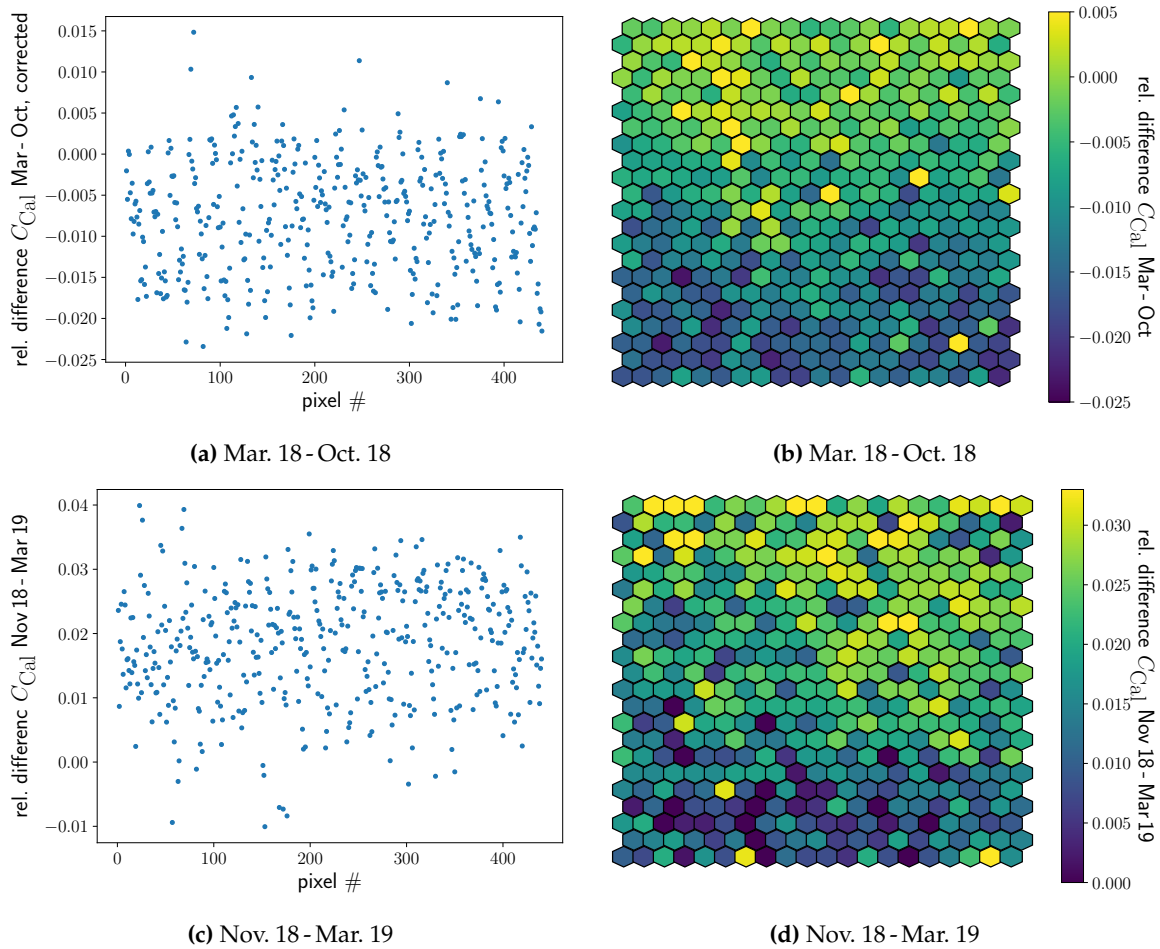


Figure 5.15: Difference between measurements from two different XY-Scanner campaigns. (a) and (b) show the difference between the first and the second campaign. (a) and (b) between the second and the third. The column structure comes from the ordering of the PMTs on the camera and translate to a top/bottom difference in the 2D representation.

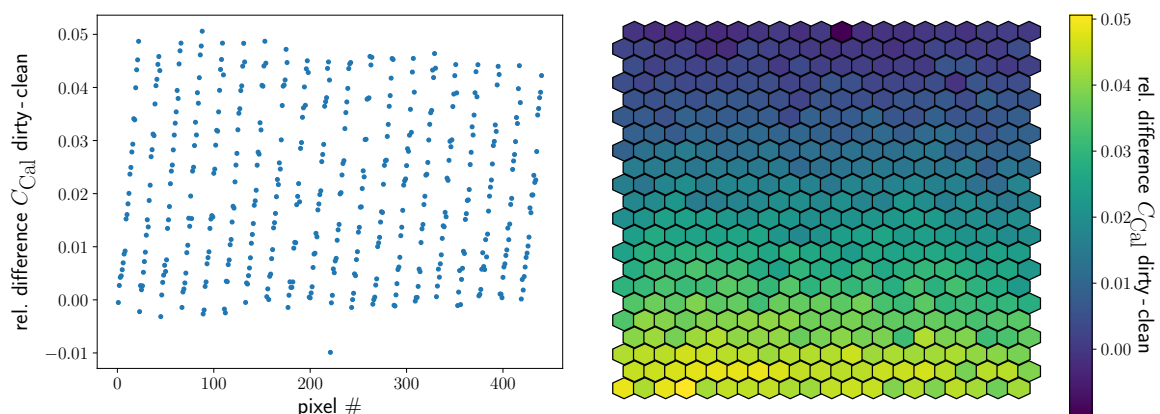


Figure 5.16: Cleaning of a mirror. The dust layer was thicker on the bottom of the mirror, thus the change in calibration constant is the strongest there.

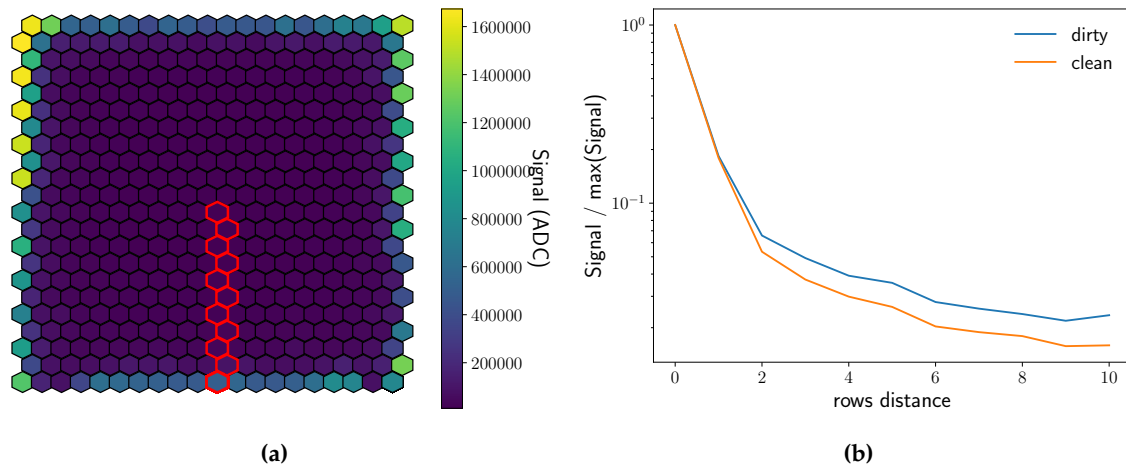


Figure 5.17: Point spread function like measurements with the XY-Scanner. (b) shows the relative signal in the marked pixels in (a) for a clean and dirty mirror. The marked pixel at the border should give the dominant contribution to the scattered light in the other pixels, but contributions from all other illuminated pixels are inseparable. No phase space correction was done.

is the central position⁹ of the grid. There, most of the light is blocked by the backside of the camera and only pixels at the border are illuminated, as shown in Fig. 5.17(a). One column of the camera is then used to get a comparison before and after the cleaning of the mirror. In Fig. 5.17(b) the signal is plotted relative to the signal in the border pixel. This, however, incorporates contributions from every other illuminated pixel at the border of the camera. A proper point spread function, measured with the octocopter as a light source, can be found in [99]. Similar measurements can be made in the future with a collimated light source mounted on the XY-Scanner. This would also overcome shortcomings of the octocopter method, which was limited in flight altitude and therefore was only able to directly illuminate pixels at the bottom of the field of view. The measurements with the octocopter also included scattering in the atmosphere¹⁰ contrary to the XY-Scanner.

Dust on UV Filters

The outside of the UV filters is exposed to the environment during measurements. Therefore, the accumulation of dust is much faster compared to the mirror. After previous measurements [100] a four monthly cleaning schedule for the standard telescopes, and monthly for HEAT¹¹, has been established. Even towards the end of a cleaning cycle, and with additional dust from the building procedure, only a small effect on the calibration was found when a filter was cleaned between two measurements. The difference is shown in Fig. 5.18 and is $\sim 1\%$, twice the reproducibility of the method derived above. The cleaning interval seems, therefore, to be short enough. As mentioned before the effect this dust layer has on the point spread function of the telescope can not be studied with the XY-Scanner.

⁹ This position exists multiple times in one run, see Appendix A.1 ¹⁰ a typical distance to the telescopes is ~ 1 km ¹¹ in upward position the filters are less inclined which accelerates the accumulation of dust

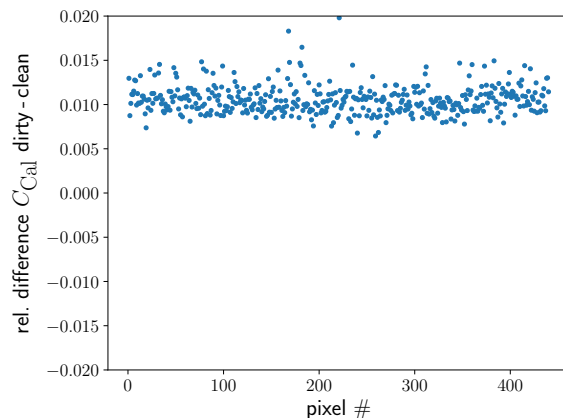


Figure 5.18: Difference between two measurements with the UV filter being cleaned in between.

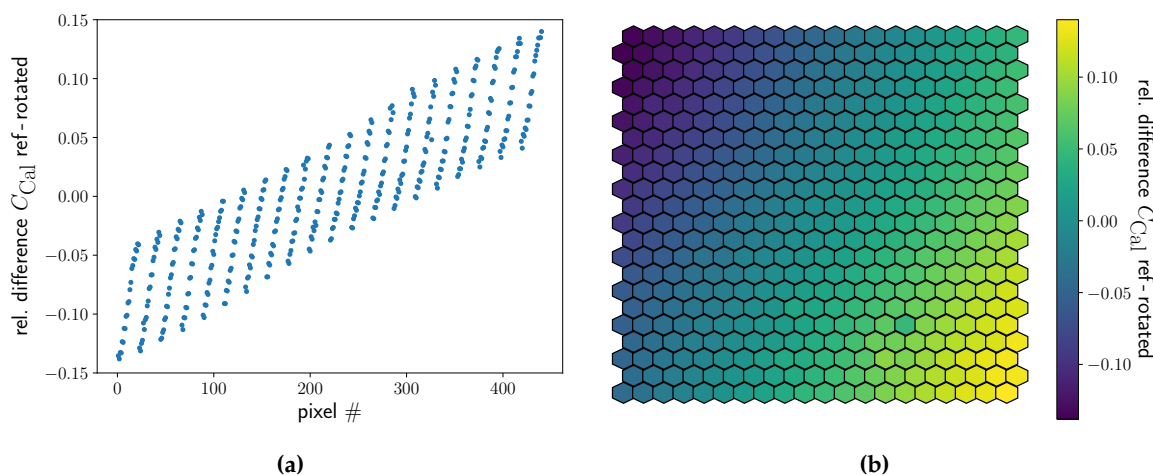


Figure 5.19: Comparison of two measurements, where in between the sphere was rotated by 180° , for the Karlsruhe sphere. The influence of the shadow of the baffle is clearly visible on the diagonal axis of the camera.

5.4 Isotropy of the Light Source

The analysis of the XY-Scanner calibration assumes a perfect Lambertian emission spectrum if this is not the case the deviation contributes to the systematic uncertainty. An integrating sphere is a Lambertian light source by design, however, the Karlsruhe sphere shows distinct deviations to a Lambertian emission spectrum, as discussed in Section 4.1.2. To test the influence of the deviation from the Lambertian emission spectrum on the calibration analysis a special set of measurements was performed. In between two measurements, the sphere was rotated by 180° around its optical axis to invert the emission spectrum. Over- and under-densities in the emission should then show up in the comparison of the two.

The first measurements presented here were done with the Karlsruhe sphere as it was delivered from the manufacturer. The results are shown in Fig. 5.19. The effect is at its maximum on the diagonal axis of the camera. This coincides with the placement of the LED in the integrating sphere which is at $\sim 45^\circ$ to the vertical axis. The baffle is too big and thus shadowed parts of the exit port. The effect was found to be $\sim 15\%$ at maximum, which is close to the

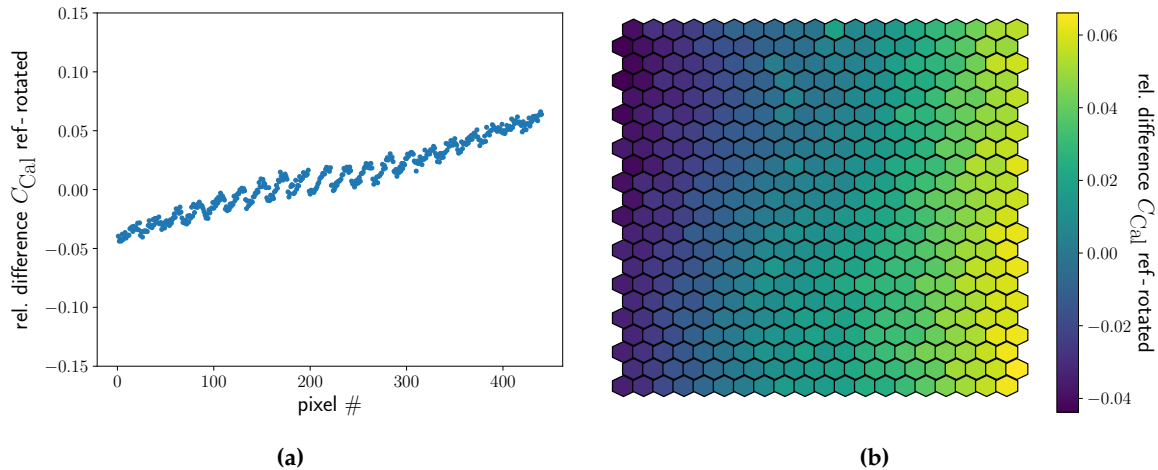


Figure 5.20: Comparison of two measurements, where in between the sphere was rotated by 180° , for the Czech sphere. Compared to Fig. 5.19 the sphere was rotated by 45° so that the LED is now in the horizontal plane.

12% reported from the measurements in Olomouc [87]. The difference between the two measurements can be explained by the difference in the experimental set-up. The measurements in Olomouc were done at 5 representative spots in the exit port, whereas at the telescope the whole area of the exit port contributes to the results.

The updated design presented in Section 4.1.2 was also measured in April 2019. The new baffle was much smaller and moved to the LED head it now blocks only the LED used in the on-site measurements. The diffuser described in Section 4.1.2 was not yet included at the time of the measurements. The results are shown in Fig. 5.20. The amplitude of the effect is reduced by roughly a factor of three, the maximal deviation is now 5%. There also is a flatter region in the center of the camera, the effect does not extend as far to smaller angles as before. A second difference is the orientation of the sphere. The LED head is now in the horizontal plane, where the maximum viewing angle is 15° , and not $\sim 20^\circ$ as on the diagonal. This decreases the influence of inhomogeneities at larger angles in the direction of the LED head.

5.4.1 Hardware Changes

As mentioned above the results change quite drastically when the flasher board and especially the LED head are exchanged. A measurement of this change can be found in Fig. 5.21. This is caused by imperfections in the production of the used LEDs. Sometimes the LED is tilted which also tilts the emission spectrum [95]. This can be avoided by preselecting the LEDs and the diffuser in front of the LED which was built into the Czech sphere.

5.4.2 Tilting of the Sphere

Similar signatures in the camera, to both the isotropy measurements and the cleaning of a mirror, can be produced by tilting the sphere. Several reasons are possible why the exit port of the light source could not be parallel to the aperture of the telescope. They range from imperfections in the construction of the aperture box and the XY-Scanner to imprecise mounting of the x-axis or the sphere. In the final procedure, when the goal is to calibrate

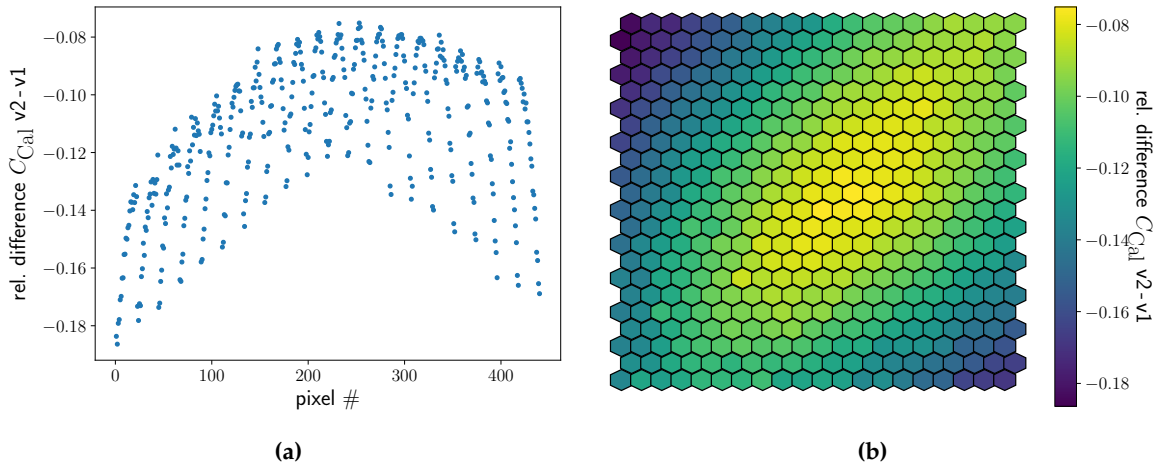


Figure 5.21: Difference between two identical measurements where only the electronics of the sphere was exchanged. The constant offset comes from the unknown difference in light output, the structure comes from imperfection in the production and placement of the LED.

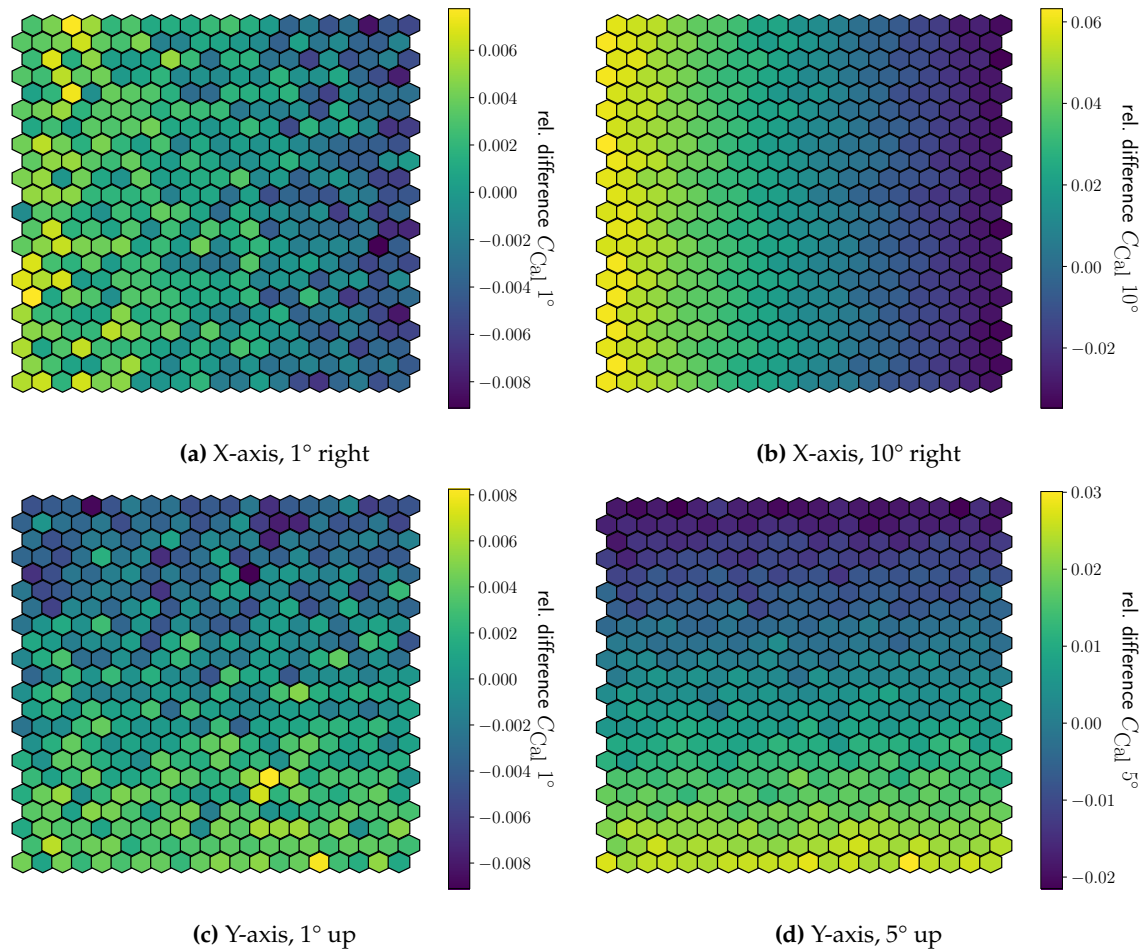


Figure 5.22: (a), (b) Tilting of the sphere in direction of the X-axis and (c), (d) in direction of the Y-axis. The effect grows with the tilting angle and gets asymmetric at larger angles.

multiple telescopes in one night, the mounting has to be done during the night. Simulations were done to estimate the influence of the sphere-tilt on the calibration analysis. Both a tilt in x- and in y-direction has been simulated and the results are shown in Fig. 5.22. The difference of the calibration constants grows with the tilting angle. It is also asymmetric, this comes from the Lambertian emission spectrum which is proportional to the cosine of the angle to the optical axis. In the direction of the tilt, the pixels are shifted to smaller angles where the cosine is rather flat. In the other direction, pixels are shifted to higher angles where the cosine falls more steeply.

The tilt in the direction of the y-axis looks just like the effect from the dust layer on the mirror, compare Figs. 5.16, 5.22(c) and 5.22(d). The only difference is that here the effect is somewhat symmetrical around zero, whereas for the mirror cleaning it is always positive. To get the same amplitude of the two effects the sphere would need to be tilted by $\sim 5^\circ$. Which over the 60 mm width of the sled on the x-axis would mean that there is a gap to the sphere holding structure on one side of the sled of ~ 5 mm. A gap this large would have been noticed when tightening the screws. Another possible reason is the shearing of the X-axis by the torsional moment which is caused by the off-center placement of the light source on the X-axis. In measurements with an inclinometer, this was found to be negligible ($\pm 0.15^\circ$).

A tilt in the X-axis direction gives a similar signature to the isotropy measurements, compare Figs. 5.20(b), 5.22(a) and 5.22(b). Again, the effect here is not symmetrical, whereas the isotropy measurements are symmetrical by design.

5.5 Relative Calibration of Telescopes

A first and preliminary calibration of the Karlsruhe sphere was done in Wuppertal. This calibration was done with the parameters used in most of the measurements of the third campaign: 5 μ s pulses, the electronics version which is capable of 0.1 A steps in the LED current and the 2 inch port reducer. Using this calibration of the sphere for the calibration of CO 3 run 13853, the ratio to the standard calibration was 1.036 ± 0.002 . This would be a good agreement between the two methods within the systematic uncertainties. However, both the calibration of the sphere and the analysis of the XY-Scanner calibration of the telescopes assumes a perfect Lambertian emission spectrum, which, as shown above, is not the case. But, the measurements can still be used for a relative comparison of the energy calibration of the telescopes

The relative energy calibration of the FD telescopes was tested many times before. Examples are shown in Fig. 5.23. Fig. 5.23(a) was done with stereo FD events. Due to the low statistics, this was done on the level of FD buildings. Additionally, most of the stereo events are in the area directly between the buildings and thus appear in a subset of the telescopes. Fig. 5.23(b) was done in comparison to the energy measured with the SD. As this energy is calibrated with FD data this shows the deviation of single telescopes to the mean. However, these measurements take the average over a large time window, whereas with the XY-Scanner we get the state of the detector at one point in time. That the calibration can change quite drastically with time is shown in Fig. 5.23(c). This analysis uses stereo events when HEAT is in downward mode and a fit of the longitudinal air shower profile with a step in upward mode.

The ratio of the standard calibration constants [104] to the calibration constants derived with the XY-Scanner method should be a constant over all telescopes. If the PMTs in one

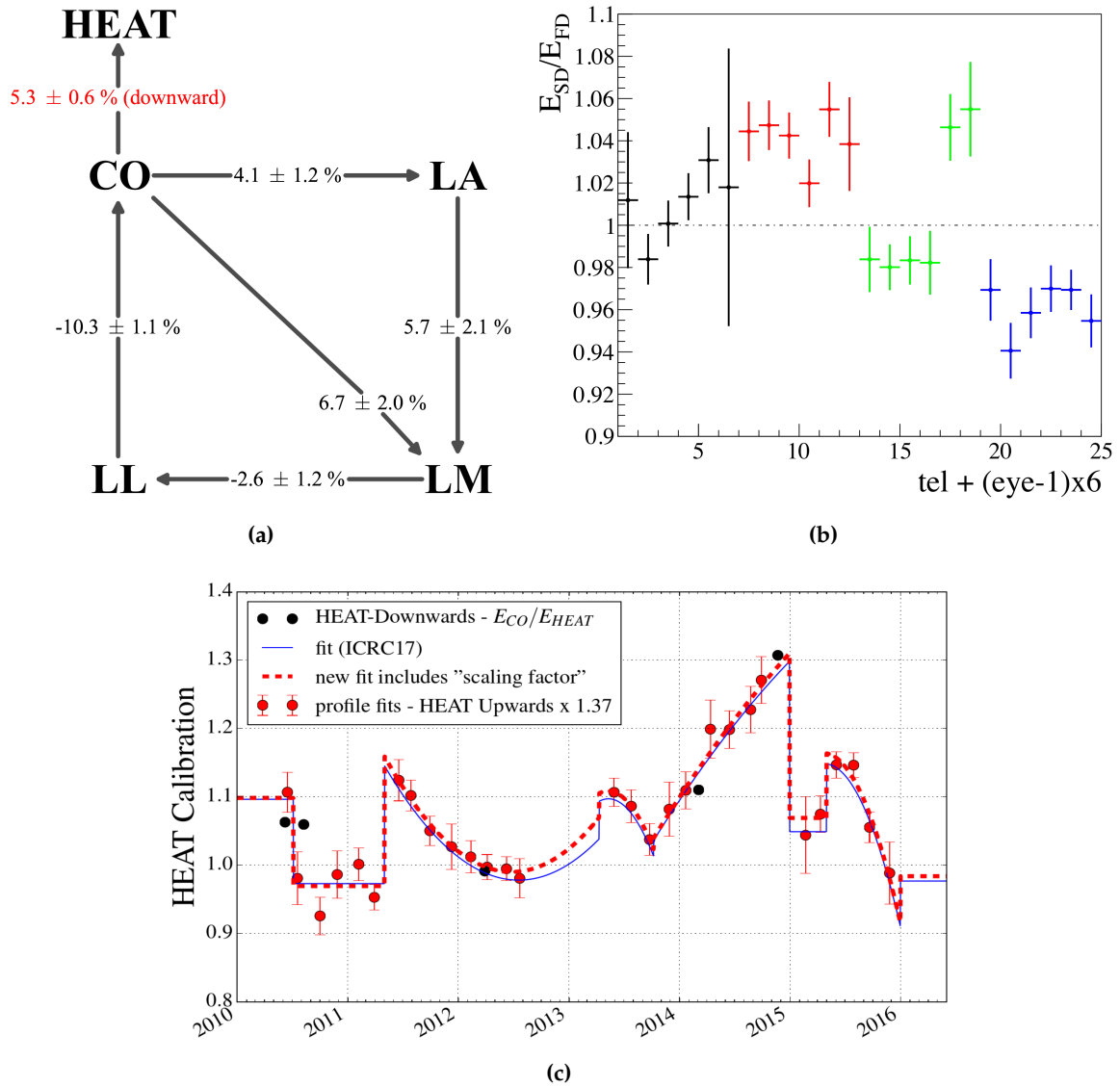


Figure 5.23: Previous energy scale comparisons (b) in comparison to SD measurements [102], (a) with stereo air showers in FD data [79] and (c) also stereo events with time dependency [103].

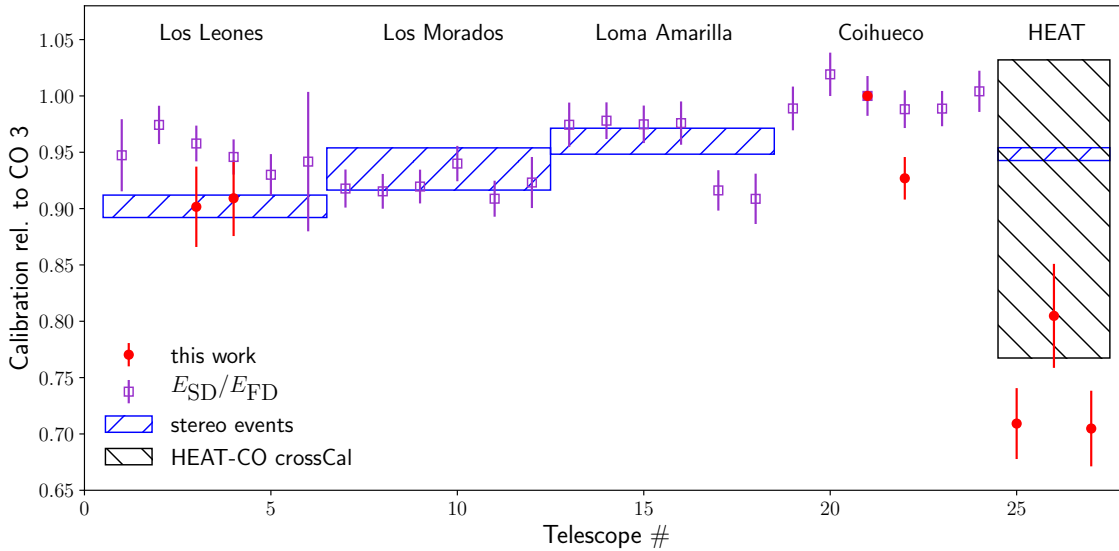
telescope are more sensitive, both methods should yield lower values for the calibration constants. It was shown above that the results from the XY-Scanner method are reproducible within 0.5%. Larger deviations in the ratio of the standard and the new calibration constants are thus likely to originate from the relative calibration in the long period since the last drum measurements. The results from the comparison of XY-Scanner measurements with the standard calibration are shown in Table 5.1, relatively to Coihueco telescope 3. This telescope was chosen as the reference, as it sees the CLF and was not changed by us during the measurements¹².

The results are also shown in Fig. 5.24, together with the other relative calibration studies shown above. As can be seen, the relative differences are within [0.9, 1.0] and it can thus be concluded that the relative differences are within $\pm 5\%$. The cleaning of a mirror changes the calibration by half of the maximum reported in Section 5.3.3, as it is to be expected. For

¹² For Los Leones telescope 4 the mirror was cleaned, see Section 5.3.3

Table 5.1: Test of the energy scale between telescopes. The difference is compared to Coihueco bay three, if the XY-Scanner calibration can be assumed constant.

telescope	difference [%]	std. dev. [%]	comment
LL 3	-9.8 ± 0.2	3.7	
LL 4	-11.5 ± 0.2	3.8	before mirror cleaning
LL 4	-9.1 ± 0.2	3.4	after mirror cleaning
CO 3	0	0	reference
CO 4	-7.3 ± 0.1	1.9	
HEAT 1	-29.1 ± 0.2	3.1	
HEAT 2	-19.5 ± 0.2	4.6	
HEAT 3	12.6 ± 0.3	5.5	
HEAT 3	-29.5 ± 0.2	3.4	After correction for jump in calibration in 2016 [105]

**Figure 5.24:** Combined plot of different studies of the relative calibration of the FD relative to CO 3. For the points of this work, the standard deviation is used for the error, as shown in Table 5.1. For the other analyses, the uncertainty of the mean is shown.

the HEAT telescopes, we find a significantly different calibration and the relative difference to CO is around 0.7 for HEAT 1 and 3 and 0.8 for HEAT 2 (or about 0.75 ± 0.05 for the whole HEAT system). This might be explained by the special geometry of HEAT. In “upward” mode the whole building is tilted backward by 30° , from that follows that the large parts of the mirror surface are less inclined and dust accumulation is expected to be increased. To test this hypothesis, it would be necessary to clean the mirror of a HEAT telescope.

As a crosscheck, air showers, recorded from April 1, 2019 to April 13, 2019, were reconstructed with both calibrations. This was done for HEAT 1 and CO 3, as those telescopes have approximately the same field of view when HEAT is in downward mode. The energy ratio, E_{CO}/E_{HEAT} , was found to be 1.41 ± 0.06 for standard calibration and 0.97 ± 0.05 for the

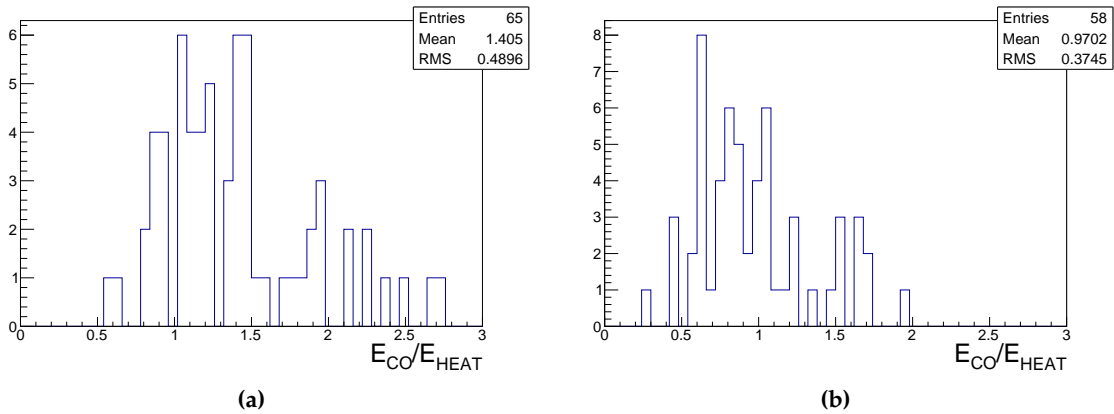


Figure 5.25: Ratio of the reconstructed air shower energy in CO 3 and HEAT 1 for (a) standard calibration and (b) the XY-Scanner calibration.

XY-Scanner calibration. The distributions are shown in Fig. 5.25. This is in agreement with the comparison between the standard and the XY-Scanner calibration. It also shows significant improvement for the new calibration method. However, the errors are purely statistical, for example, the drift of calibration constants, as shown in Fig. 5.5 and atmospheric corrections were ignored. For the other two telescopes of HEAT, this crosscheck is not possible as the overlapping telescopes of CO are not yet equipped with XY-Scanners.

CHAPTER

6

Summary and Outlook

In this work, we presented two studies of high relevance for the future operation of the Fluorescence Detector (FD) of the Pierre Auger Observatory. The first part is dedicated to decreasing the statistical uncertainties at the highest energies for measurements with the FD. An extension of the duty cycle of the FD increases the detection rate in the remaining lifetime of the Pierre Auger Observatory. The second topic is a new method for the end-to-end calibration of large-aperture telescopes, called the “XY-Scanner”. The main difference to the previous method, the “drum”, is, that the measurement is split into many measurements at different positions on the aperture with a small and flexible light source that is easy to handle and to calibrate.

The increase of the duty cycle of the FD fits nicely into the upgrade of the Pierre Auger Observatory, which aims at improving the composition sensitivity of the experiment. The main part of the upgrade is the addition of scintillators and radio antennas to the existing water-Cherenkov detector (WCD). These different parts of the new Surface Detector (SD) stations respond differently to the electromagnetic and muonic components of an air shower, which can be used to discriminate between different primary particles. However, the expected mass sensitivity does not match that of the depth of the shower maximum (X_{\max}), which can be directly observed with the FD. The low duty cycle of the FD comes from the night-sky background. For measurements with a higher night-sky background, the gain of the photo-multiplier tubes (PMTs) has to be reduced. In a detailed simulation study, as presented in Chapter 3, it was shown, that at the highest energies air showers can be detected with fluorescence telescopes at low gain. At $1 \times 10^{19.5}$ eV, full reconstruction efficiency over the SD array is reached and the amount of additional events increases with the duty cycle. With an increase of the duty cycle by $\sim 50\%$, the number of additional events per year above $1 \times 10^{19.5}$ eV can be increased from 7 to ~ 11 . At the same time, the decrease of the experimental resolution due to the increased background noise in the additional time periods is acceptable. Both X_{\max} and energy resolution were found to deteriorate by less than 50% of their current values.

In test measurements, we have shown that the detector behaves well under switching of gain levels and the relative calibration system can be used to track the status of the detector. We

have successfully reconstructed 28 events from nine nights of data taking during high night-sky background with reduced gain, out of which three were in the targeted energy range above 1×10^{19} eV. The detector is ready for operation at reduced gain and the additional measurement time can be included in the standard schedule with only minor changes to the steering software of the FD.

The XY-Scanner calibration method is described in Chapter 4. The development of a new method for the FD calibration became necessary since the old calibration method was effectively discontinued after the last measurements six years ago. The new light source consists of a light-emitting diode (LED) inside an integrating sphere, mounted on an XY-Scanner. A near-uniform coverage of the aperture, similar to the drum, is achieved by taking many measurements at different positions on the aperture. In simulations, we have shown, that the parameters of the grid of positions on the aperture can be chosen such that the difference to the drum are negligible. The reflection of back-scattered photons from the telescope, a big uncertainty in the drum calibration, is less than 0.4 % according to our simulation. With the default settings, one telescope can be calibrated in 45 minutes, which is short enough to reach the goal of being able to calibrate three telescopes in one night. The whole FD can thus be calibrated in nine days.

The results are reproducible within $\sim 0.5\%$, as derived by comparing repeated measurements of the same telescope within one night. Larger differences were found by comparing measurements of the same telescopes separated by more than six months, but it seems plausible that these differences are not due to the instability of the XY-Scanner method but in fact a measurement of the effect of accumulating dust on the FD mirrors. The effect the cleaning of a mirror has on the calibration was found to be between 0 and 5 % depending on the elevation on the mirror. The general purpose sphere, used in most of the presented measurements, showed large deviations from a Lambertian emission spectrum of up to 15 %. A prototype of an improved sphere was also tested and showed a better homogeneity by a factor of three (up to 5 %). The most recent prototype of the sphere in its near-final design is expected to reduce the inhomogeneity by another factor of two (up to 2.5 %). The remaining inhomogeneity is thus very small and can easily be corrected for in the analysis of the calibration constants. A study of the relative calibration of the telescopes was presented. The difference between the measured standard telescopes is within $\pm 5\%$, for the HEAT telescopes the calibration was found to be $0.75 \pm 0,05$ relative to Coihueco. The work of this thesis thus shows that the XY-Scanner is a promising technique to provide an absolute calibration of large-aperture telescopes and that it is a suitable replacement for the previous method of calibrating the FD telescopes with the drum.

Acronyms

This is a list of acronyms used within this work sorted alphabetically according to the short version.

AERA	Auger Engineering Radio Array
AMIGA	Auger Muon Detectors for the Infill Ground Array
CMB	cosmic microwave background
Cal A	Calibration A
Cal B	Calibration B
Cal C	Calibration C
CLF	Central Laser Facility
CO	Coihueco Auger Telescope Site
FD	Fluorescence Detector
FLT	first level trigger
FoV	field of view
GZK	Greisen–Zatsepin–Kuzmin
HEAT	High Elevation Auger Telescopes
LA	Loma Amarilla Auger Telescope Site
LCU	LED Calibration Unit
LED	light-emitting diode
LL	Los Leones Auger Telescope Site
LM	Los Morados Auger Telescope Site
PMT	photo-multiplier tube
SALLA	Short Aperiodic Loaded Loop Antenna
SD	Surface Detector
SiPM	Silicon Photomultiplier
SLT	second level trigger
SSD	Scintillating surface detector
TA	Telescope Array
TLT	third level trigger
UHECR	ultrahigh-energy cosmic ray

UV	ultraviolet
VAOD	vertical aerosol optical depth
WCD	water-Cherenkov detector
XLF	eXtreme Laser Facility

APPENDIX

A

Logbook

Dates, run numbers and extra information for both the XY-Scanner campaigns, results discussed in Chapter 5, and the extended uptime test measurements, Chapter 3.

A.1 XY-Scanner

This section contains the logbook for the three XY-Scanner campaigns starting in March and October of 2018 and March 2019. The main goals for each campaign and additional information are given as far as it's important to understand what was done.

Steering files are used to tell the XY-Scanner the sequence of positions for the flashes. These positions are given in (x, y, t) , where x and y are positions on the aperture in millimeter and t is the pause time in seconds. The pause time is needed so that the maximum readout frequency of the telescopes of 1 Hz is not exceeded. The comment at the beginning of the file gives information on the parameters of the grid: distance between the positions, radius, and cuts. The cut values give the maximum distance from the center of the aperture in any direction before the sphere crashes into the structures of the aperture box. As the value of these cuts can be different for each telescope, the telescope the steering file was generated for is also given. To make it easier to check a run for completeness ten dummy flashes in the center of the aperture were added at the beginning and the end of each run. An example is given in Listing A.1. In the following, the steering files are given as plots. Green circles with a dot in the center mark the flasher positions on the aperture. The center mark is used in the calculation of the positions, as long as it is inside the grid radius the position is included, even if part of the spot is outside. The circle has the size of the default 2 inch exit port (Fig. B.2). The size of the drum cover¹ is indicated by a red circle. If the steering file was generated after the implementation of the cuts a green box indicates the reachable area of the aperture. The plots are in Figs. A.1 to A.6.

¹ cover at the aperture to facilitate a light-tight mounting of the drum

Listing A.1: Example of an XY-Scanner steering file. The header gives information on which telescope this file was generated for as well as the grid parameters and cut values. Each job starts and ends with 10 flashes in the center.

```
# Coihueco , bay 3
#
# generated by /home/auger/src/XYScanner/Scanner/scripts/
# generate_hexpattern.py at 2018-11-07 01:51:16.836275
#
# Grid size: 100mm
# min. Radius: 0mm
# max. Radius: 1300mm
# cut: -1270 <= x <= 1270
# cut: -1256 <= y <= 1240
# Pause: 1s
# Center: (0mm, 0mm)
#
# x, y, t
# 10 dummy positions:
0, 0, 1
[...]
0, 0, 1
# done
400, -1212, 1
300, -1212, 1
200, -1212, 1
100, -1212, 1
0, -1212, 1
-100, -1212, 1
-200, -1212, 1
-300, -1212, 1
-400, -1212, 1
-550, -1125, 1
-450, -1125, 1
[...]
-100, 1212, 1
-200, 1212, 1
-300, 1212, 1
-400, 1212, 1
# 10 dummy positions:
0, 0, 1
[...]
0, 0, 1
# done
```

The cut values for all telescopes used in the measurements up to March 2019 are given in Table B.1. The values differ only marginally, therefore the steering files for different telescopes are identical most of the time. In Figs. A.1 to A.6 they are therefore only plotted if no identical plot exists.

The light source contains three LEDs, for measurements at the telescopes LED 2 is used. The other LEDs are used to check the aging of LED 2 and for measurements in the lab.

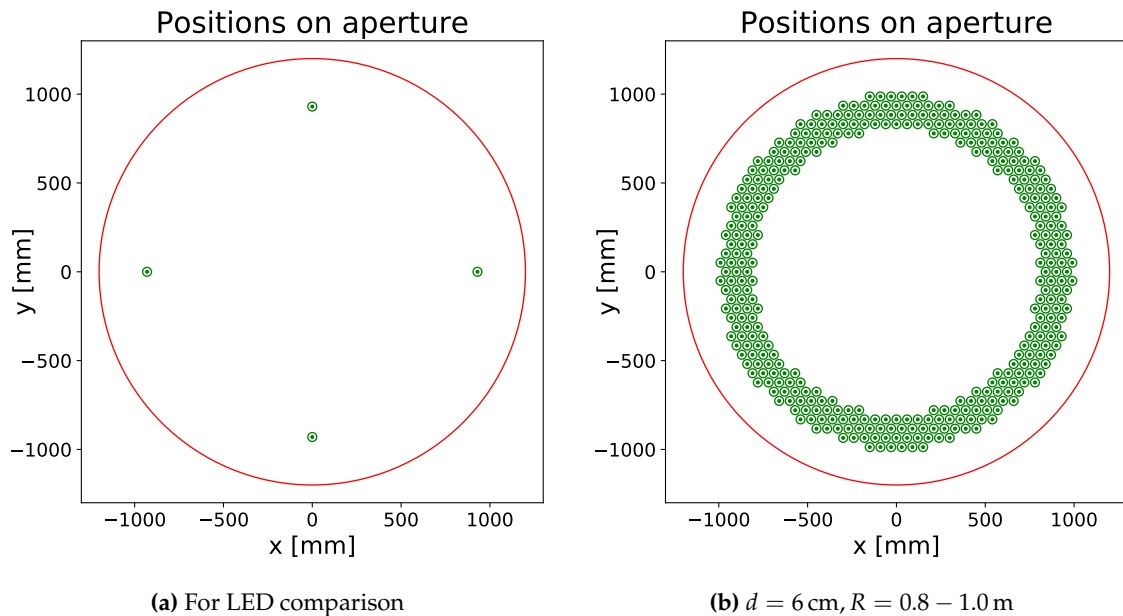


Figure A.1: General purpose XY-Scanner steering files, these can be used for all telescopes. (a) shows the pattern used for relative strength comparisons between the different LEDs, the positions where chosen so that the amount of shadows in the images is small. d is the distance between the positions and R the range in grid radius.

A.1.1 March 2018

In March 2018 the first XY-Scanner was installed at Coihueco (CO) 4. A second XY-Scanner was installed at Los Leones (LL) 4, to test how it can be mounted on different aperture bay designs, but was never operated. As discussed in Section 5.2 one of the main results was that the prototype was not big enough. The log is given in Table A.1, each measurement there links to a steering file which is given in Figs. A.1 to A.3.

A.1.2 October 2018

This campaign started with repeating the measurements at CO 4 to test the long-time stability of the new calibration system (Section 5.3). Then the old XY-Scanners were dismantled and parts were used to build the new, bigger Scanners. These were mounted at CO 3 and HEAT 1. The log for CO is in Table A.2, the one for HEAT in Table A.3. The new steering files can be found in Fig. A.4 and Fig. A.5. Towards the end of the previous campaign, the peaks in the camera started to saturate. A new version of the sphere electronics, with finer steps in LED current, was used in this campaign, see Table B.2.

A.1.3 March 2019

New measurements in this campaign were done at LL 3 & 4, and HEAT 2 & 3. One of the main goals was to measure the effect on measurements when a mirror gets cleaned. This was done at LL 4. The new sphere holding structure used at CO was tested to correct for small position errors of the previous design. For a picture see Fig. B.4. In the future, the same holding structure as for the Czech sphere will be used, see Fig. 4.6.

Table A.1: XY-Scanner logbook March 2018 at Coihueco 4. If not stated otherwise in the comment column the following parameters apply: The port reducer has a diameter of 2 in (Fig. B.2), the distance piece on the sled is 10 cm long (Fig. B.3), the electronics v1 (Table B.2) gets used and the shutters are open. All steering files plotted in Fig. A.2 have positions outside of the accessible area, these flashes were done as far out as possible and should be removed in reconstruction.

date	run number	pattern	comment
07/03/18	12 723–12 725	Fig. A.1(a)	Testpattern for relative strength comparison of LEDs in order 2, 1, 3, closed shutter
	12 727	Fig. A.2(a)	closed shutter
	12 729	Fig. A.2(a)	reversed order of positions, closed shutter
	12 732–12 734	Fig. A.1(a)	LED testing, order 1, 2, 3, closed shutter
08/03/18	12 739, 12 741	Fig. A.1(b)	five flashes at each position, closed shutter
	12 744	Fig. A.1(b)	five flashes at each position, sphere rotated by 180°, closed shutter
09/03/18	12 754	Fig. A.2(a)	run into rising moon, enough clouds so background variance was no problem
10/03/18	12 765–12 769	Fig. A.2(c)	no Cal A
	12 770–12 772	Fig. A.2(b)	no Cal A
	12 773, 12 774	Fig. A.2(d)	no Cal A
	12 775–12 779	Fig. A.2(b)	no Cal A
	12 780	Fig. A.2(c)	no Cal A
12/03/18	12 792–12 795	Fig. A.2(e)	3 cm distance piece
	12 799	Fig. A.2(c)	3 cm distance piece, five flashes at each position
	12 801	Fig. A.2(f)	3 cm distance piece, pattern shifted by 3 cm
13/03/18	12 807, 12 808	Fig. A.3(a)	3 cm distance piece
	12 810	Fig. A.3(a)	3 cm distance piece, reversed order of positions
	12 812	Fig. A.3(c)	3 cm distance piece, no port reducer
	12 814	Fig. A.3(c)	3 cm distance piece, no port reducer, sphere rotated by 180°
15/03/18	12 826–12 828	Fig. A.1(a)	LEDs testing: order 1, 2, 3, wrong initialisation resulting in the pattern being slightly shifted
	12 830–12 832	Fig. A.1(a)	LED testing, order 1, 2, 3, wrong initialisation, 3 cm distance piece
	12 833–12 835	Fig. A.1(a)	LED testing, order 1, 2, 3, 3 cm distance piece
	12 837–12 839	Fig. A.1(a)	LED testing, order 1, 2, 3
	12 841, 12 842	Fig. A.3(b)	3 cm distance piece, saturated peaks
	12 845	Fig. A.3(b)	3 cm distance piece, saturated peaks, cleaned UV filters
	12 848	Fig. A.3(b)	3 cm distance piece, low gain

The log and the new steering files can be found at:

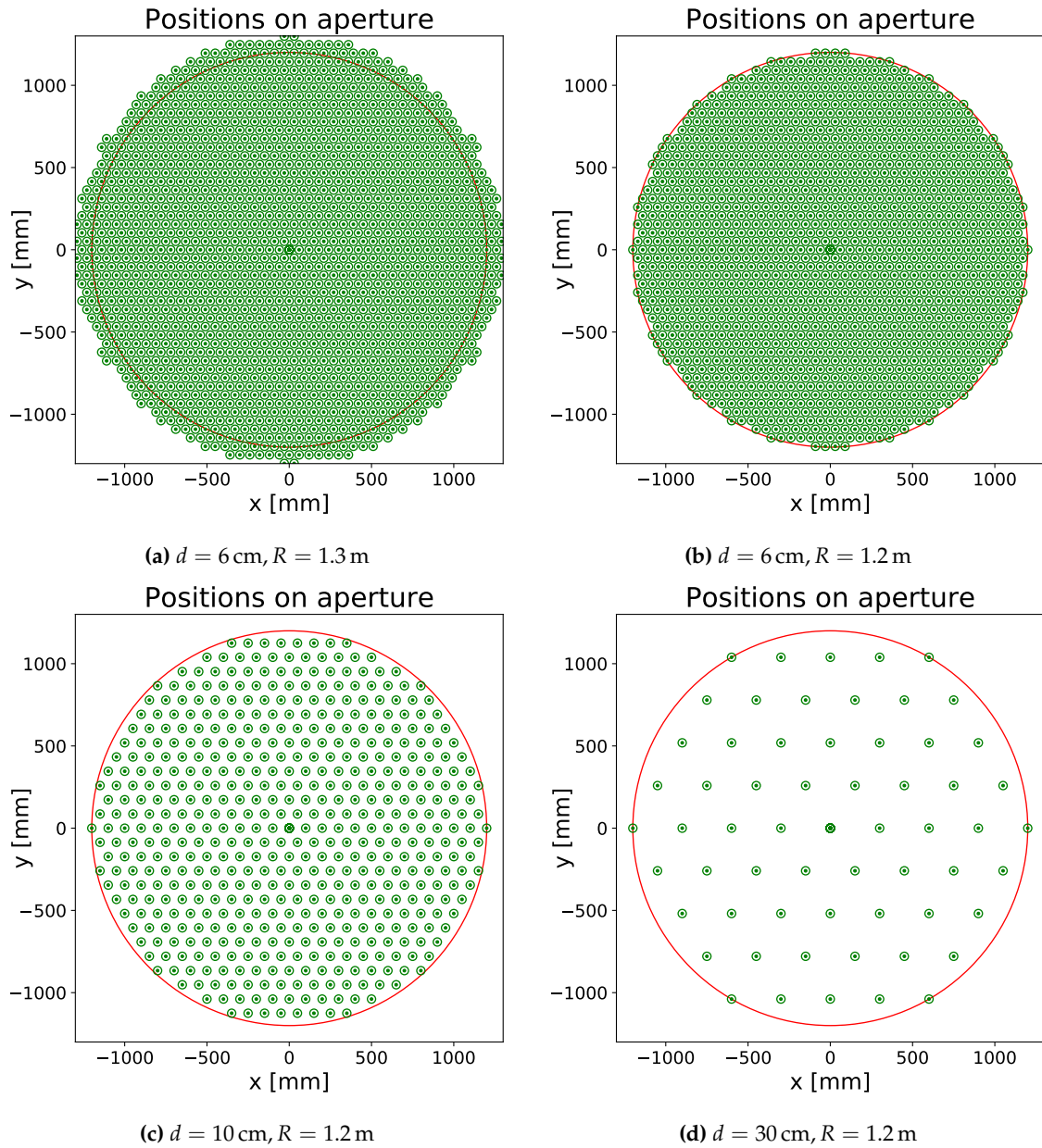


Figure A.2: XY Scanner steering files without cuts, therefore unreachable positions at the edges of the aperture exist. These flashes were done as far out as possible and should be removed in reconstruction. d is the distance between the positions and R the maximal grid radius.

- LL: Table A.4 and Fig. A.6
- CO: Table A.5
- HEAT: Table A.6

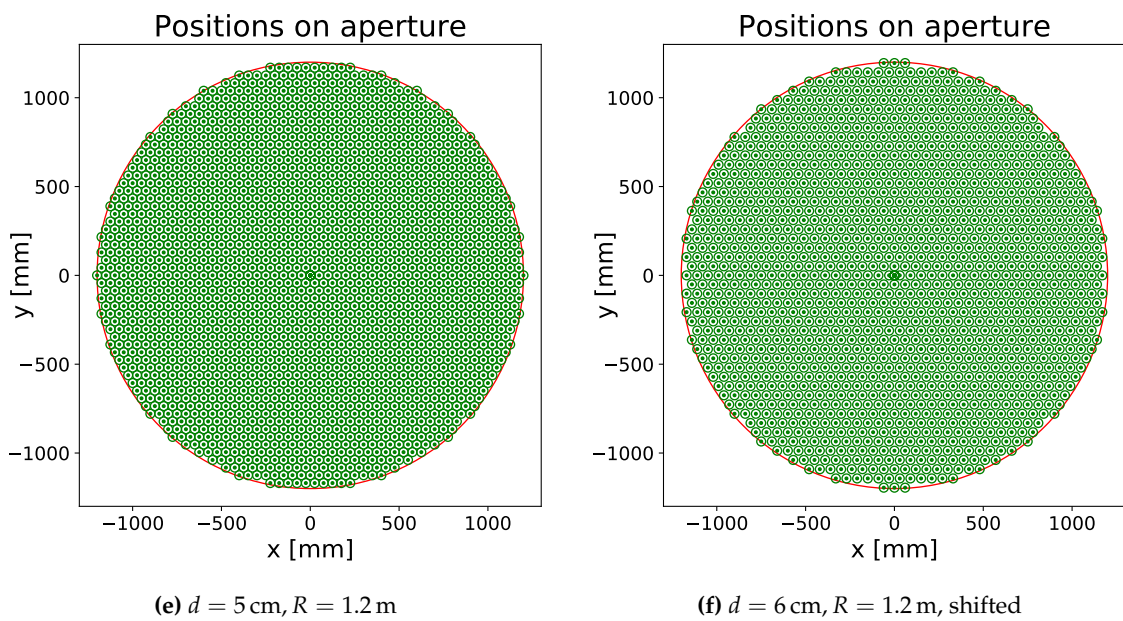


Figure A.2: XY Scanner steering files without cut, therefore unreachable positions at the edges of the aperture exist. These flashes were done as far out as possible and should be removed in reconstruction. d is the distance between the positions and R the maximal grid radius.(cont.)

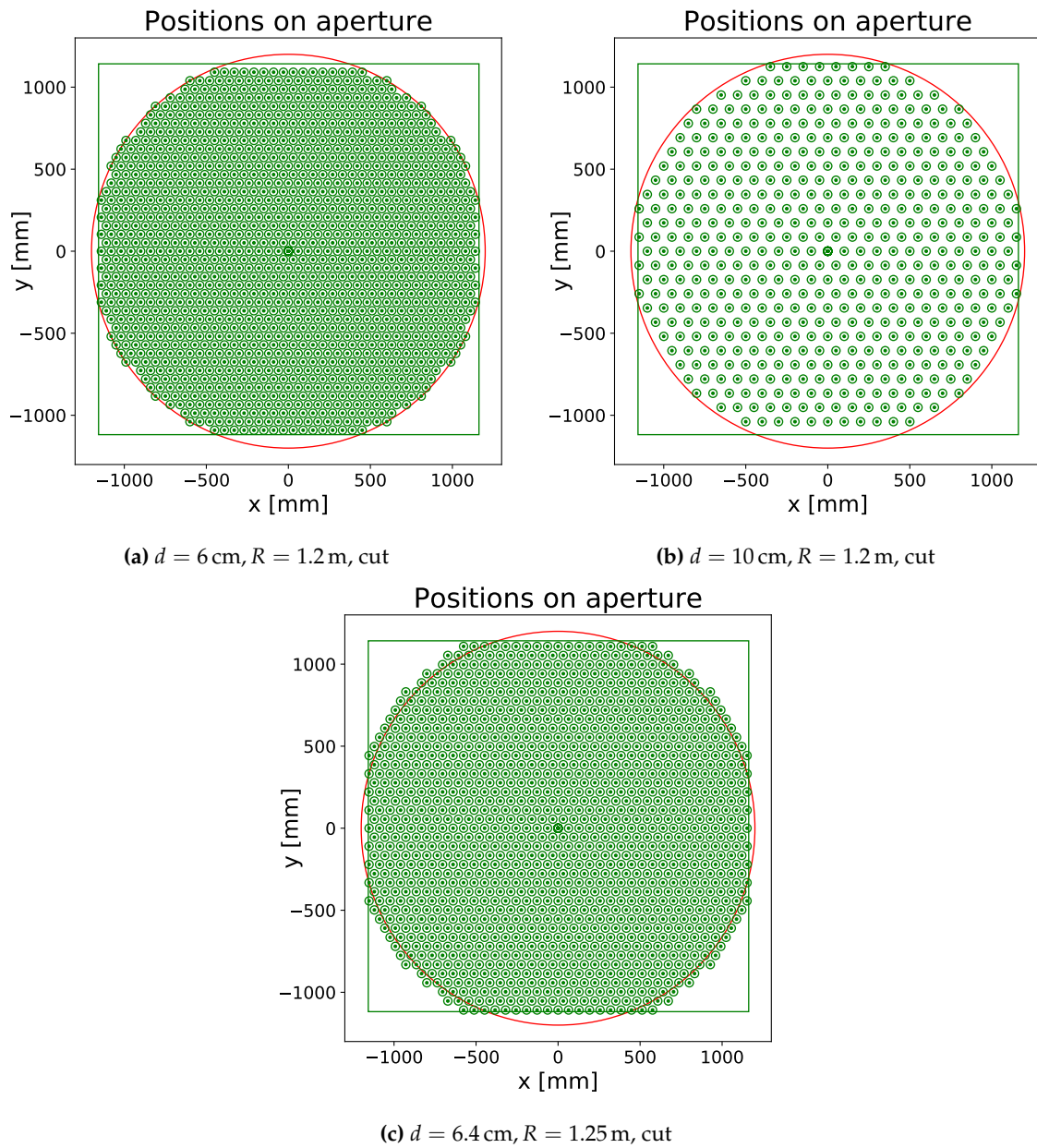


Figure A.3: XY Scanner steering files with cuts for CO 4 first prototype: The cuts were done to avoid unreachable positions in the aperture and are given in Appendix B.1. d is the distance between the positions and R the maximal grid radius.

Table A.2: XY-Scanner logbook October 2018 for Coihueco . If not stated elsewhere in the comment column the following parameters apply: The port reducer has a diameter of 2 in (Fig. B.2), the distance piece on the sled is 3 cm long (Fig. B.3), electronics v1 gets used (Table B.2) and the shutters are open. Only in this campaigns different tracelengths in the readout of the camera were used, non-standard tracelength is indicated as well.

date	run number	telescope	pattern	comment
26/10/18	13 382–13 385	4	Fig. A.3(b)	short traces, do not use run 13384
	13 389–13 394	4	Fig. A.3(b)	do not use run 13391
28/10/18	13 400, 12 402	4	Fig. A.3(b)	
	13 404–13 408	4	Fig. A.3(a)	do not use run 13406
	13 410–13 412	4	Fig. A.1(a)	LED testing, order 1, 2, 3
	13 413, 13 415	4	Fig. A.3(b)	closed shutter
06/11/18	13 453	3	Fig. A.4(a)	
	13 455	3	Fig. A.4(b)	short traces
	13 456	3	Fig. A.4(b)	
	13 458	3	Fig. A.4(a)	port reducer 1 in
	13 460	3	Fig. A.4(a)	port reducer 1 in, reversed order
07/11/18	13 468	3	Fig. A.4(a)	
	13 471	3	Fig. A.4(b)	
08/11/18	13 482	3	Fig. A.4(a)	electronics v2, sphere rotated by 180°
	13 484	3	Fig. A.4(a)	electronics v2, port reducer 1 in, sphere rotated by 180°
	13 486	3	Fig. A.4(a)	electronics v2, port reducer 1 in
	13 488–13 490	3	Fig. A.1(a)	electronics v2, LEDs testing, order 1, 2, 3
	13 492, 13 493	3	Fig. A.4(a)	electronics v2
12/11/18	13 514, 13 515	3	Fig. A.1(a)	LEDs testing, order 2, 3, LED 1 broken

Table A.3: XY-Scanner logbook October 2018 for HEAT. If not stated elsewhere in the comment column the following parameters apply: The port reducer has a diameter of 2 in (Fig. B.2), the distance piece on the sled is 3 cm long (Fig. B.3), electronics v1 gets used (Table B.2) and the shutters are open.

date	run number	pattern	comment
07/11/18	4088	Fig. A.5(a)	
	4090	Fig. A.5(b)	

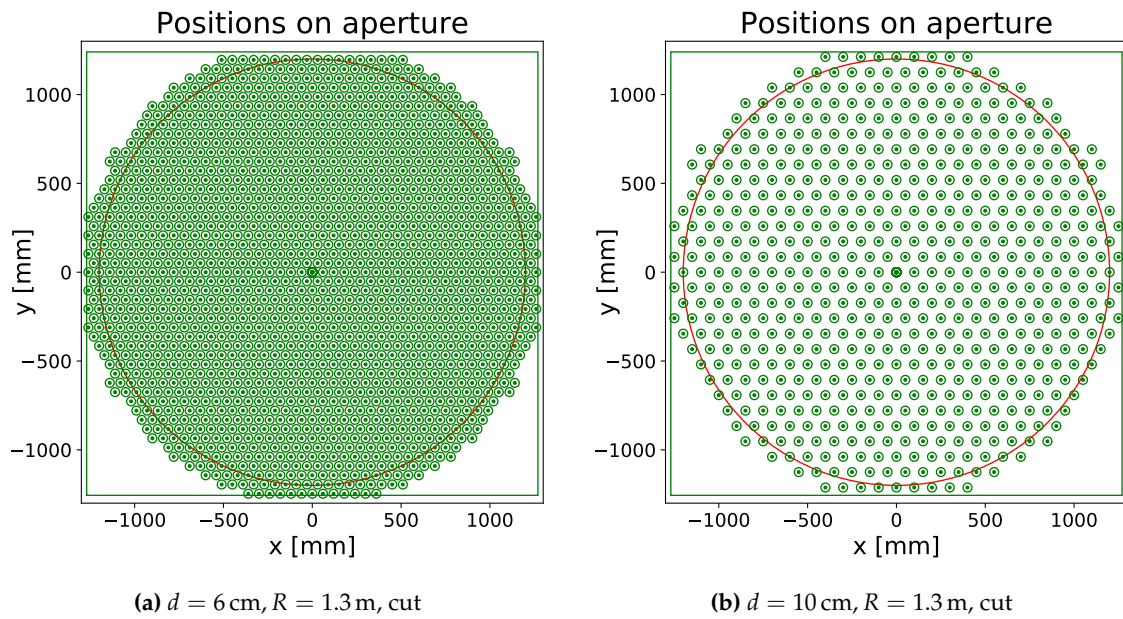


Figure A.4: XY Scanner steering files with cut for CO 3. The cut values are given in Appendix B.1. d is the distance between the positions and R the maximal grid radius. The steering files for the other standard telescopes equipped with an XY-Scanner are identical and are therefore not shown separately.

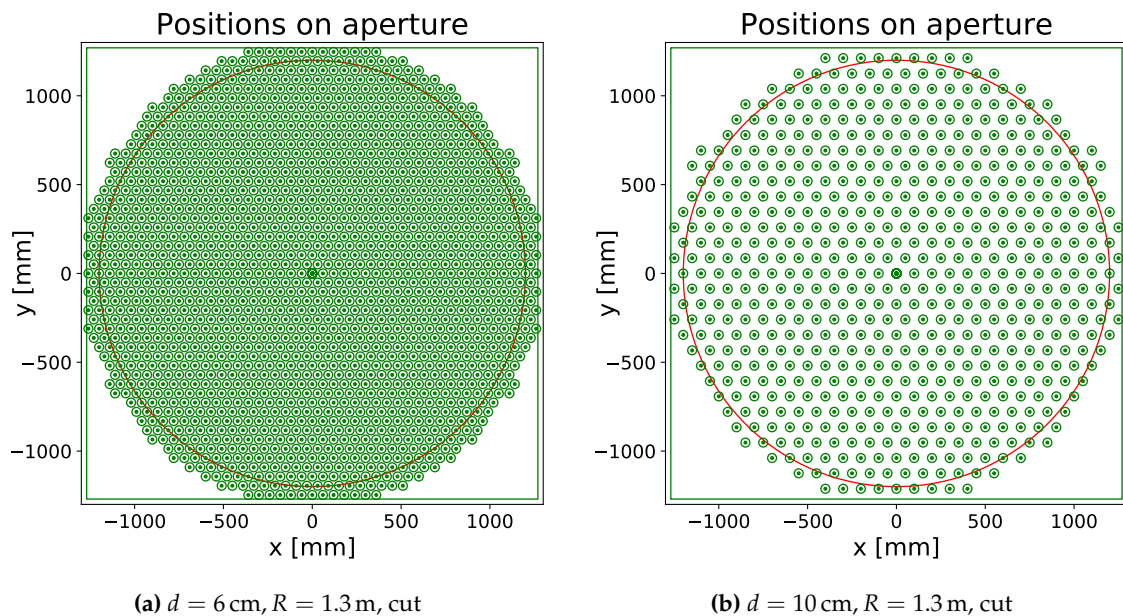


Figure A.5: XY Scanner steering files with cut for HEAT 1. The cut values are given in Appendix B.1. d is the distance between the positions and R the maximal grid radius.

Table A.4: XY-Scanner logbook March 2019 for Los Leones . If not stated otherwise in the comment column the following parameters apply: The port reducer has a diameter of 2 in (Fig. B.2), the distance piece on the sled is 3 cm long (Fig. B.3), electronics v2 gets used (Table B.2) and the shutters are open. The Czech sphere came with its own mounting (Fig. 4.6). For explanation of the position of the LED and photodiode head on the Czech sphere see Fig. B.1.

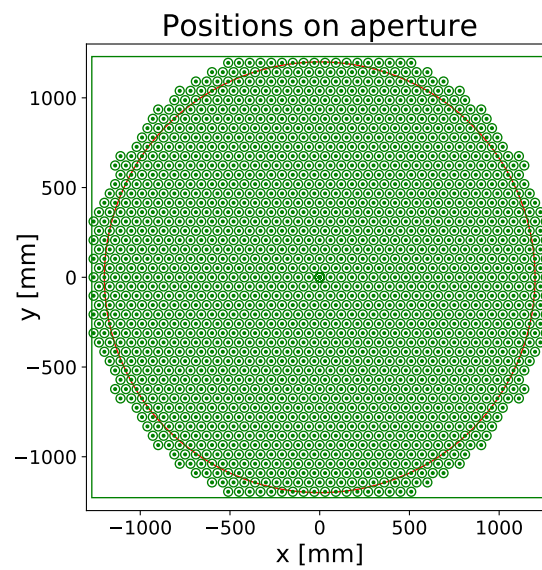
date	run number	telescope	pattern	comment
02/04/19	14 080	4	Fig. A.4(a)	
	14 083	4	Fig. A.4(a)	cleaned Filter
	14 085	4	Fig. A.4(b)	
03/04/19	14 091	4	Fig. A.6(a)	Czech sphere, electronics v3, opt. pos.
	14 093	4	Fig. A.6(a)	Czech sphere, electronics v3, opt. pos. + 90°
	14 095	4	Fig. A.6(a)	Czech sphere, electronics v3, opt. pos. + 180°
	14 097	4	Fig. A.6(a)	Czech sphere, electronics v3, opt. pos. + 45°
04/04/19	14 102	3	Fig. A.4(b)	
	14 104	3	Fig. A.4(a)	
	14 107	4	Fig. A.4(a)	
05/04/19		4		Cleaning of the mirror
07/04/19	14 116	4	Fig. A.4(a)	
	14 118	4	Fig. A.4(b)	
	14 128	4	Fig. A.6(a)	Czech sphere electronics v3, opt. pos. + 90°
	14 131	4	Fig. A.6(a)	Czech sphere electronics v3, opt. pos. + 270°
10/04/19	14 141	4	Fig. A.6(a)	Czech sphere, electronics v4, opt. pos. + 270°
	14 143	4	Fig. A.6(a)	Czech sphere, electronics v4, opt. pos. + 90°

Table A.5: XY-Scanner logbook March 2019 for Coihueco . If not stated otherwise in the comment column the following parameters apply: The port reducer has a diameter of 2 in (Fig. B.2), the distance piece on the sled is 3 cm long (Fig. B.3), electronics v2 gets used (Table B.2) and the shutters are open.

date	run number	telescope	pattern	comment
25/03/19	13 802	3	Fig. A.4(b)	electronics v1, new sphere holding structure
	13 804	3	Fig. A.4(a)	electronics v1, new sphere holding structure
26/03/19	13 809	3	Fig. A.4(b)	electronics v1
01/04/19	13 844	4	Fig. A.4(a)	
	13 846	4	Fig. A.4(b)	
	13 848	4	Fig. A.4(a)	reversed order of positions
	13 853	3	Fig. A.4(a)	
	13 855	3	Fig. A.4(b)	

Table A.6: XY-Scanner logbook March 2019 for HEAT. If not stated otherwise in the comment column the following parameters apply: The port reducer has a diameter of 2 in (Fig. B.2), the distance piece on the sled is 3 cm long (Fig. B.3), electronics v2 gets used (Table B.2) and the shutters are open.

date	run number	telescope	pattern	comment
08/04/19	4229	1	Fig. A.5(b)	
	4231	1	Fig. A.5(a)	
	4234	3	Fig. A.5(a)	
09/04/19	4241	2	Fig. A.5(a)	



(a) $d = 6$ cm, $R = 1.3$ m, cut

Figure A.6: XY Scanner steering files with cut for the mounting structure of the Czech sphere. There is an offset in vertical placement as the sphere is rotatable here. Thus the steering file misses one line of positions at the bottom compared to Fig. A.4(a). d is the distance between the positions and R the maximal grid radius.

A.2 Extended Uptime

The dates and run numbers of the four measurement campaigns at reduced gain are given in Table A.7.

Table A.7: Complete logbook for all test measurements taken with reduced gain.

date	run numbers	telescopes	comment
27/02/15	5423	LL1	moon: 68 %, [83]
28/02/15	5424 and 5425	LL1	moon: 77 %
01/03/15	5426	LL1	moon: 84 %
02/03/15	5427–5429	LL1	moon: 91 %
03/03/15	5430	LL1	even lower gain setting moon: 95 %
11/06/16	6002	LL 1 and 4	during shift before measurements start, moon: 42 %
14/06/16	6006	LL 1	Three nights after shift end moon: 70 %
15/06/16	6007	LL 1	moon: 78 %
17/06/16	6008	LL 1	moon: 92 %
05/03/18	6697–6701	LL 1–6	Three nights before shift start, moon: 86 %
06/03/18	6702–6706	LL 1–6	moon: 78 %
07/03/18	6707–6711	LL 1–6	moon: 69 %
08/11/18	7129	LL 1–6	More laser data, during shift, moon: 1 %
09/11/18	7134	LL 1–6	Possible problems in bay 3, moon: 4 %

APPENDIX

B

Hardware Details of the XY-Scanner

Additional information to the XY-Scanner presented in Chapter 4.

B.1 Size of the Scannable Aperture

The cut values for the scannable aperture discussed in Section 5.2.1 are given in Table B.1. They all include a safety margin of a few millimeters before the sphere would crash into the aperture box or other parts of the XY-Scanner. This was measured for each bay and sphere holding structure individually. As the cut values are similar and the spread smaller than the distance between two rows of positions, the same steering files were used for all telescopes. The cut value is the last allowed position for the center of a flash, positions further out get truncated by the scanner steering software.

B.2 Electronics

Multiple flasher boards and LED and photodiode heads were manufactured. They were matched in pairs and adapted to have low noise. In Table B.2 all combinations of boards and heads, used in measurements in Argentina, are listed and labeled. Once, board and heads were mixed ($\sqrt{3}$), this was because of delayed luggage.

B.3 Czech Sphere Angular Positions

The optimized design of the XY-Scanner sphere came with its holding structure. This holding structure allowed for a free rotation around the optical axis of the telescope, steps of 45° were marked. The optimal position was defined as the LED head being in the horizontal plane. The anisotropy of the lightsource, as discussed in Section 5.4, is largest in the direction of the

Table B.1: Size of scannable aperture for all telescopes with an XY-Scanner. Cut values are given as distance to the center.

Telescope	x_{\min} [cm]	x_{\max} [cm]	y_{\min} [cm]	y_{\max} [cm]	comment
LL 3	127	127	125.5	123.5	
LL 4	127	127	125	124	
LL 4	127	127	122.8	123	Czech holding structure
LA 3	127	127	125.9	123.5	no successful measurement
CO 3	127	127	125.6	124	
CO 3	127	127	125.8	123.7	New sphere holding structure
CO 4	127	127	125.5	124	
CO 4	116	116	112	114	first prototype
HEAT 1	127	127	127	127	
HEAT 2	127	127	127	127	
HEAT 3	127	127	127	127	

Table B.2: Combinations of flasher boards and LED and photodiode heads used in the field. Board and heads are numbered in production and should be used in pairs as the boards are adjusted for features of the heads.

Name	Board	Heads	comment
v1	2	1	Capable of changing LED current in steps of 1 μA
v2	1	2	Capable of changing LED current in steps of 0.1 μA
v3	5	6	Combination because of missing luggage
v4	6	6	Given to our colleagues in Olomouc for testing and improving the sphere geometry

LED head¹. If this is in the horizontal plane² the maximum angular distance on the camera is 15° and not $\sim 20^\circ$ as in the diagonal. The angle to the optimal position is given clockwise when looking at the sphere from the back, as shown in Fig. B.1.

B.4 Minor Hardware Parts

Additional pictures of parts of the XY-Scanner can be found in:

- Fig. B.2 shows pictures of the 2 inch port reducer
- Fig. B.3 shows the used distance parts
- Fig. B.4 shows an alternative design for the sphere holding structure which was only used in a few measurements

¹ as seen from the exit port ² vertical would be the same

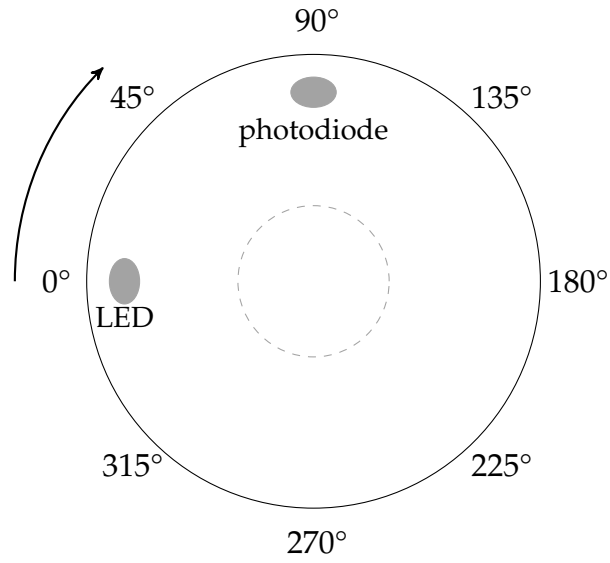


Figure B.1: Definition of the optimal and relative positions for the Czech sphere

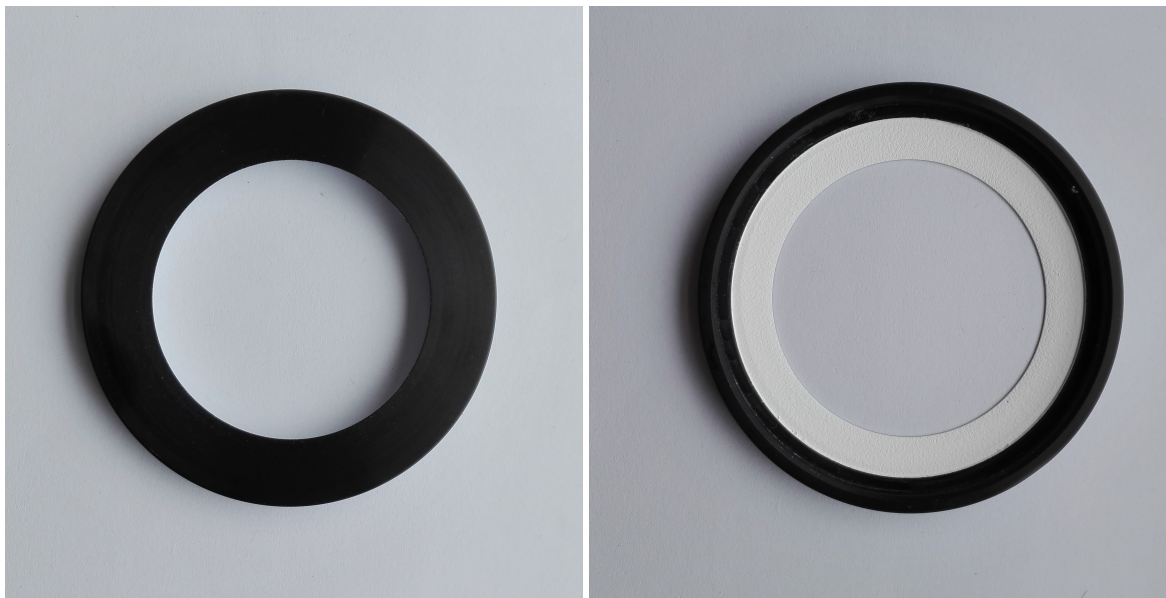


Figure B.2: Photos of the 2 inch port reducer, reflective paint on the inside

- Fig. B.5 shows the transport case of the sphere



Figure B.3: Photos of the distance parts used in the field.



Figure B.4: Photo of an alternative design for the sphere holding structure meant to correct for imprecision in the first prototype. It was only used in few measurements in the field and then dropped in favor of the holding structure of the Czech sphere.



Figure B.5: Transport case of the Karlsruhe sphere, can be brought as hand luggage on flights.

APPENDIX

C

FD trigger threshold in low gain simulations

C.1 Introduction

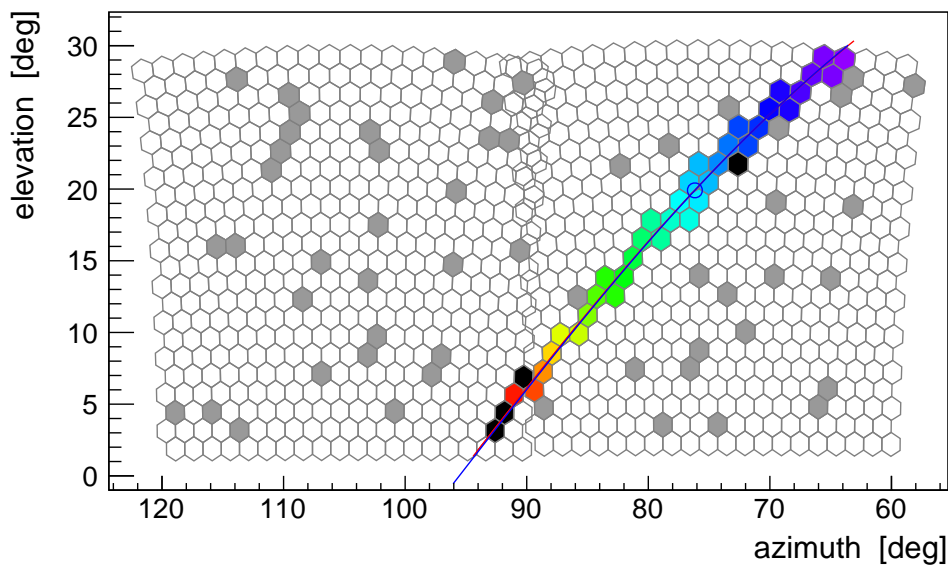
The standard simulation of threshold values for the first level trigger (FLT) in FD simulations is described here [77]. There, the threshold values were tabulated as a function of ADC counts for a given number of photoelectrons. Poissonian fluctuation of the number of emitted photoelectrons as well as Gaussian fluctuation coming from the PMT gain chain have been accounted for in this calculation. For the standard FD operation it was a reasonable assumption that the electronic noise is negligible. However, at reduced gain, this is no longer the case. Here, the electronic noise is the dominant source of fluctuations over a wide range of background light fluxes. As a consequence, the threshold values are underestimated in simulations with reduced gain, resulting in large numbers of randomly triggered pixels (see Fig. C.1).

To not run into the same problem whenever the parameters of the FD measurements are changed we aimed for a fast and easy way to adapt the simulation of threshold values to different sets of parameters. To be independent of differences in implementations, we use the standard `Offline` module for the simulation of FD traces, the `FdElectronicsSimulatorOG`. The detector configuration can be changed with the usual xml config files. The obtained threshold values for different settings are put into a xml file with string identifiers. This identifier is the md5 sum of all detector settings which influence the simulation of FD traces¹.

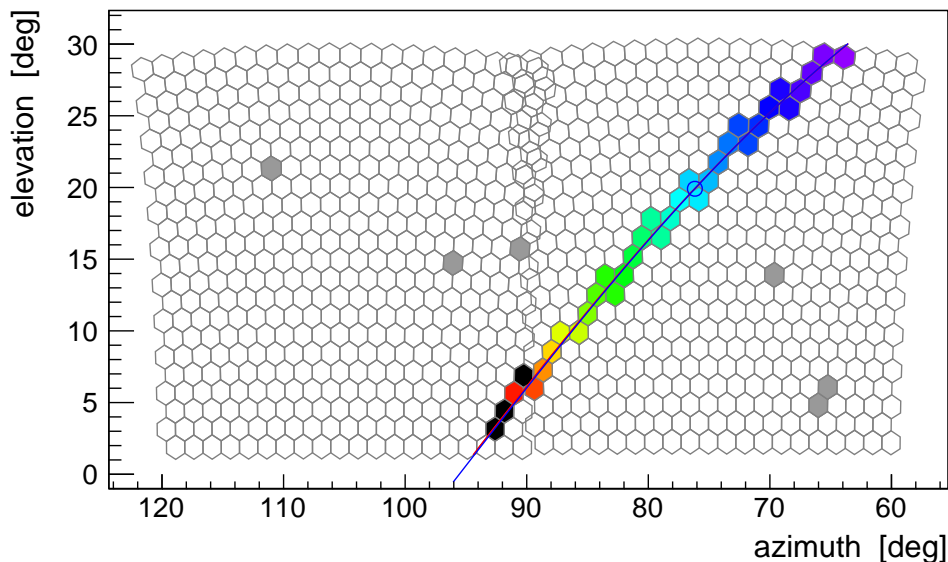
C.2 Threshold simulation

The new simulation of threshold values is implemented as an `Offline` application consisting of three modules:

¹ Similar to how it was done for the simulated calibration constants



(a) Old threshold



(b) New threshold

Figure C.1: Simulation of an FD event for (a) old and (b) new threshold. The simulation with old threshold produces many randomly triggered pixels as well as a wrong T2 trigger pattern in the top left.

1. MeanNpeFillerKG

Dummy module to set up an event and write in all the variables FdElectronicsSimulatorOG needs to run. As we want pure background traces no signal is added. The threshold value is needed for different numbers of photoelectrons at the photocathode. These numbers can be specified in the config xml of this module as well as the number of events that should be simulated.

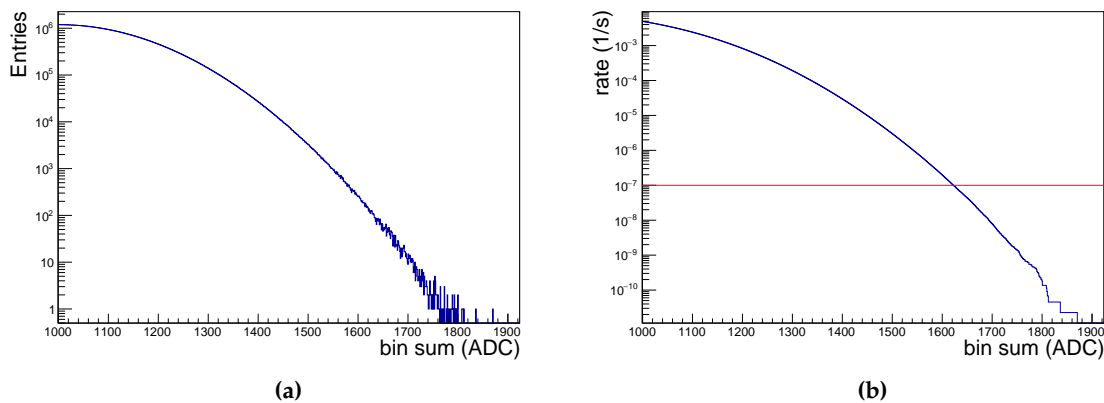


Figure C.2: (a) Histogram of bin sums, (b) cumulative of the same histogram divided by the total length of produced traces. The red line is at a trigger rate of 100 Hz.

2. FdElectronicsSimulatorOG

The standard Offline module. In the config xml <thresholdMode> should be set to "1" as this is expected from the other two modules.

3. ThresholdCalculatorKG

This module does the actual calculation of the threshold values. As for the single PMT trigger, N consecutive bins² are summed up. These sums are written into a histogram (see Fig. C.2(a)). In the end, the histogram is divided by the total length of the simulated traces to get the rate for each sum value to occur. When the cumulative of this histogram reaches 100 Hz the threshold is reached (see Fig. C.2(b)).

An example for standard detector settings can be found in the standard applications folder³. If you change the detector settings, make sure that the fixed and simulated calibration constants are changed accordingly⁴.

C.3 How to use it

To use the new thresholds in simulations change <useNewThreshold> to "1" in the FdElectronicsSimulator.xml file. The threshold values are stored in a separate xml-file as tabulated functions. An example can be found in Code Listing C.1. There, the threshold values for standard telescopes at nominal and at reduced gain are shown. In contrast to the ones at standard gain, the threshold value at reduced gain stays almost constant for the first few entries. This shows that the electronic noise is indeed the dominant contribution for low background flux at reduced gain.

² $N = 10$ for standard telescopes, $N = 20$ for HEAT ³ trunk/Documentation/StandardApplications/FdThresholdSimulation ⁴ Only needed when you change the gain

Listing C.1: FSimulationThreshold.xml.in with entries for standard telescopes with nominal and reduced gain.

```
<?xml version="1.0" encoding="iso-8859-1"?>

<FSimulationThreshold xmlns:xsi="http://www.w3.org/2001/XMLSchema-
instance"
                    xsi:noNamespaceSchemaLocation= '
                    @XMLSCHEMALOCATION@/FSimulationThreshold.
                    xsd'>

  <Threshold signature="2e25a9c959a12cbfcbb4a17bc4a8ab8f">
    <!--Threshold: Gain = 1.754 GainVariance = 0.41 ElectronicNoise
      = 3.5 CutoffFrequency = 0.0031 FLTTriggerRate = 1e-07
      FLTBoxcarSize = 10 Telescopetype = standard-->
    <x> 2 3 5 10 20 30 50 100 200 500 2000 10000</x>
    <y> 55 62 75 99 134 160 204 284 397 621 1237 2742</y>
  </Threshold>

  <Threshold signature="4bd0867d57c9d19eaae37f9af8c6b588">
    <!--Threshold: Gain = 0.1754 GainVariance = 0.41 ElectronicNoise
      = 3.5 CutoffFrequency = 0.0031 FLTTriggerRate = 1e-07
      FLTBoxcarSize = 10 Telescopetype = standard-->
    <x> 2 3 5 10 20 30 50 100 200 500 2000 10000</x>
    <y> 32 32 32 33 34 35 37 42 50 69 127 277</y>
  </Threshold>

</FSimulationThreshold>
```

C.4 Summary

We have introduced a new simulation code for the calculation of threshold values for an FLT in the FD. The code uses standard Offline modules for the simulation of the PMT traces, which makes it easy to repeat the simulations with different detector settings. The code is intended primarily for simulations at reduced gain, but can also be used for simulations with standard settings.

Acknowledgments

First of all, I am very thankful to Professor Ralph Engel for offering me the opportunity to work on improving the Fluorescence Detector of the Pierre Auger Observatory. Thank you for the trust and the freedom to engage in this project. I'd also like to thank Professor Guido Drexlin for accompanying this endeavor as co-referee.

I am especially grateful to my supervisor Dr. Michael Unger for the many ideas and discussions when it came to the details. Additionally, I want to thank Dr. Ralf Ulrich for his insight in the details of the simulation of the Fluorescence Detector.

I would like to thank Kai, Hermann-Josef, Christoph, Heike, and Norbert for the long time we spent together in Argentina. Building the XY-Scanners and taking all the measurements for this thesis would not have been possible without you. My appreciation to all colleagues at IPE and the universities of Wuppertal and Olomouc for the good collaboration on the XY-Scanner.

I want to thank Gaetano Salina for processing the extra relative calibration files to compare the XY-Scanner to and answering my questions on the relative calibration system. To Violet Harvey for having a look at the atmospheric monitoring at reduced gain.

To all the colleagues at IKP which became friends over the years, for all the work- and not-so-much work-related discussions and good companionship. A special thank you goes to Sabine for taking good care of all organizational things. To Daniela, Jürgen, Max, Ralf and all the other Skat players for making the lunch breaks a little bit longer than necessary.

Last but not least I want to express my gratitude to my wife and family for the love and support during these four years, especially in the final phase of this dissertation.

Bibliography

- [1] V. F. Hess, Über Beobachtungen der durchdringenden Strahlung bei sieben Freiballonfahrten, *Phys. Z.* 13 (1912) 1084–1091.
- [2] R. A. Millikan, G. H. Cameron, The Origin of the Cosmic Rays, *Phys. Rev.* 32 (1928) 533–557. doi:[10.1103/PhysRev.32.533](https://doi.org/10.1103/PhysRev.32.533).
- [3] P. Auger et al., Extensive Cosmic-Ray Showers, *Rev. Mod. Phys.* 11 (1939) 288–291. doi:[10.1103/RevModPhys.11.288](https://doi.org/10.1103/RevModPhys.11.288).
- [4] M. Nagano, Search for the end of the energy spectrum of primary cosmic rays, *New Journal of Physics* 11 (6) (2009) 065012. doi:[10.1088/1367-2630/11/6/065012](https://doi.org/10.1088/1367-2630/11/6/065012).
- [5] E. Mocchiutti, Direct detection of cosmic rays: through a new era of precision measurements of particle fluxes, *Nuclear Physics B - Proceedings Supplements* 256-257 (2014) 161 – 172, cosmic Ray Origin – Beyond the Standard Models. doi:[10.1016/j.nuclphysbps.2014.10.019](https://doi.org/10.1016/j.nuclphysbps.2014.10.019).
- [6] M. Casolino, The Pamela Cosmic Ray Space Observatory: Detector, Objectives and First Results, *Frascati Phys. Ser.* 47 (2008) 19–48. arXiv:[0904.4692](https://arxiv.org/abs/0904.4692).
- [7] S. Ting, The Alpha Magnetic Spectrometer on the International Space Station, *Nuclear Physics B - Proceedings Supplements* 243-244 (2013) 12 – 24, proceedings of the IV International Conference on Particle and Fundamental Physics in Space. doi:[10.1016/j.nuclphysbps.2013.09.028](https://doi.org/10.1016/j.nuclphysbps.2013.09.028).
- [8] A. Haungs et al., The KASCADE Cosmic-ray Data Centre KCDC: Granting Open Access to Astroparticle Physics Research Data, *Eur. Phys. J. C* 78 (9) (2018) 741. doi:[10.1140/epjc/s10052-018-6221-2](https://doi.org/10.1140/epjc/s10052-018-6221-2).
- [9] W. Heitler, The quantum theory of radiation, 3rd Edition, The international series of monographs on physics, Clarendon Pr., Oxford, 1954.
- [10] Particle Data Group, [Atomic and nuclear properties of air](#), [Online; accessed 30-September-2019].

- [11] J. Matthews, A Heitler model of extensive air showers, *Astroparticle Physics* 22 (5) (2005) 387 – 397. doi:[10.1016/j.astropartphys.2004.09.003](https://doi.org/10.1016/j.astropartphys.2004.09.003).
- [12] D. Heck et al., CORSIKA: A Monte Carlo code to simulate extensive air showers *Wissenschaftliche Berichte, FZKA-6019* (Februar 98). doi:[10.5445/IR/270043064](https://doi.org/10.5445/IR/270043064).
- [13] V. Verzi for the Pierre Auger Collaboration, [Measurement of the energy spectrum of ultra-high energy cosmic rays using the Pierre Auger Observatory](#), in: *Proceedings, 36th International Cosmic Ray Conference (ICRC2019): Madison, Wisconsin, USA, 2019*.
- [14] T. Antoni et al., The cosmic-ray experiment KASCADE, *Nuclear Instruments and Methods in Physics Research Section A: Accelerators, Spectrometers, Detectors and Associated Equipment* 513 (3) (2003) 490 – 510. doi:[10.1016/S0168-9002\(03\)02076-X](https://doi.org/10.1016/S0168-9002(03)02076-X).
- [15] Y. Tameda, Telescope Array Experiment, *Nuclear Physics B - Proceedings Supplements* 196 (2009) 74 – 79, *proceedings of the XV International Symposium on Very High Energy Cosmic Ray Interactions (ISVHECRI 2008)*. doi:[10.1016/j.nuclphysbps.2009.09.011](https://doi.org/10.1016/j.nuclphysbps.2009.09.011).
- [16] M. Tanabashi et al., Review of Particle Physics, *Phys. Rev. D* 98 (2018) 030001. doi:[10.1103/PhysRevD.98.030001](https://doi.org/10.1103/PhysRevD.98.030001).
- [17] K. Greisen, End to the Cosmic-Ray Spectrum?, *Phys. Rev. Lett.* 16 (1966) 748–750. doi:[10.1103/PhysRevLett.16.748](https://doi.org/10.1103/PhysRevLett.16.748).
- [18] G. T. Zatsepin, V. A. Kuzmin, Upper limit of the spectrum of cosmic rays, *JETP Lett.* 4 (1966) 78–80, [*Pisma Zh. Eksp. Teor. Fiz.*4,114(1966)].
- [19] R. Aloisio V. Berezhinsky, A. Gazizov, Transition from galactic to extragalactic cosmic rays, *Astroparticle Physics* 39-40 (2012) 129 – 143, *cosmic Rays Topical Issue*. doi:[10.1016/j.astropartphys.2012.09.007](https://doi.org/10.1016/j.astropartphys.2012.09.007).
- [20] A. Yushkov for the Pierre Auger Collaboration, [Mass Composition of Cosmic Rays with Energies above \$10^{17.2}\$ eV from the Hybrid Data of the Pierre Auger Observatory](#), in: *Proceedings, 36th International Cosmic Ray Conference (ICRC2019): Madison, Wisconsin, USA, 2019*.
- [21] A. Aab et al., Depth of maximum of air-shower profiles at the Pierre Auger Observatory. I. Measurements at energies above $10^{17.8}$ eV, *Phys. Rev. D* 90 (12) (2014) 122005. doi:[10.1103/PhysRevD.90.122005](https://doi.org/10.1103/PhysRevD.90.122005).
- [22] A. Aab et al., The Pierre Auger Collaboration: Contributions to the 35th International Cosmic Ray Conference (ICRC 2017). [arXiv:1708.06592](https://arxiv.org/abs/1708.06592).
- [23] A. Aab et al., Depth of maximum of air-shower profiles at the Pierre Auger Observatory. II. Composition implications, *Phys. Rev. D* 90 (12) (2014) 122006. doi:[10.1103/PhysRevD.90.122006](https://doi.org/10.1103/PhysRevD.90.122006).
- [24] E. Fermi, On the Origin of the Cosmic Radiation, *Phys. Rev.* 75 (1949) 1169–1174. doi:[10.1103/PhysRev.75.1169](https://doi.org/10.1103/PhysRev.75.1169).
- [25] A. Bell, Cosmic ray acceleration, *Astroparticle Physics* 43 (2013) 56 – 70. doi:[10.1016/j.astropartphys.2012.05.022](https://doi.org/10.1016/j.astropartphys.2012.05.022).

- [26] R. Alves Batista et al., Open Questions in Cosmic-Ray Research at Ultrahigh Energies, *Front. Astron. Space Sci.* 6 (2019) 23. doi:10.3389/fspas.2019.00023.
- [27] A. M. Hillas, The Origin of Ultrahigh-Energy Cosmic Rays, *Ann. Rev. Astron. Astrophys.* 22 (1984) 425–444. doi:10.1146/annurev.aa.22.090184.002233.
- [28] A. U. Abeysekara et al., Observation of Anisotropy of TeV Cosmic Rays with Two Years of HAWC, *Astrophys. J.* 865 (1) (2018) 57. doi:10.3847/1538-4357/aad90c.
- [29] J. C. D. Velez et al., Combined Analysis of Cosmic-Ray Anisotropy with IceCube and HAWC, *PoS ICRC2017* (2018) 539. doi:10.22323/1.301.0539.
- [30] A. Aab et al., Large-scale cosmic-ray anisotropies above 4 EeV measured by the Pierre Auger Observatory, *Astrophys. J.* 868 (1) (2018) 4. doi:10.3847/1538-4357/aae689.
- [31] A. Aab et al., An Indication of anisotropy in arrival directions of ultra-high-energy cosmic rays through comparison to the flux pattern of extragalactic gamma-ray sources, *Astrophys. J.* 853 (2) (2018) L29. doi:10.3847/2041-8213/aaa66d.
- [32] R. U. Abbasi et al., Indications of Intermediate-Scale Anisotropy of Cosmic Rays with Energy Greater Than 57 EeV in the Northern Sky Measured with the Surface Detector of the Telescope Array Experiment, *Astrophys. J.* 790 (2014) L21. doi:10.1088/2041-8205/790/2/L21.
- [33] A. Aab et al., Multi-Messenger Physics with the Pierre Auger Observatory, *Front. Astron. Space Sci.* 6 (2019) 24. doi:10.3389/fspas.2019.00024.
- [34] A. Albert et al., Search for High-energy Neutrinos from Binary Neutron Star Merger GW170817 with ANTARES, IceCube, and the Pierre Auger Observatory, *Astrophys. J.* 850 (2) (2017) L35. doi:10.3847/2041-8213/aa9aed.
- [35] A. Aab et al., Ultrahigh-energy neutrino follow-up of gravitational wave events GW150914 and GW151226 with the Pierre Auger Observatory, *Phys. Rev. D* 94 (2016) 122007. doi:10.1103/PhysRevD.94.122007.
- [36] Pierre Auger Collaboration, *Photos*, Flickr.
- [37] A. Aab et al., The Pierre Auger Cosmic Ray Observatory, *Nucl. Instrum. Meth.* A798 (2015) 172 – 213. doi:10.1016/j.nima.2015.06.058.
- [38] A. Aab et al., The Pierre Auger Observatory Upgrade - Preliminary Design Report, [arXiv:1604.03637](https://arxiv.org/abs/1604.03637).
- [39] J. Abraham et al., The Fluorescence Detector of the Pierre Auger Observatory, *Nucl. Instrum. Meth.* A620 (2010) 227–251. doi:10.1016/j.nima.2010.04.023.
- [40] B. Schmidt, *Ein lichtstarkes komafreies Spiegelsystem*, *Mitteilungen der Hamburger Sternwarte in Bergedorf* 7 (1938) 15–17.
- [41] M. Ave et al., Measurement of the pressure dependence of air fluorescence emission induced by electrons, *Astroparticle Physics* 28 (1) (2007) 41 – 57. doi:10.1016/j.astropartphys.2007.04.006.
- [42] Schott, *M-UG-6*, [Online; accessed 27-August-2019].

- [43] M. Ambrosio et al., The camera of the Pierre Auger Observatory Fluorescence Detector, *Nucl. Instrum. Meth. A*478 (1) (2002) 125 – 129, proceedings of the ninth Int.Conf. on Instrumentation. doi:10.1016/S0168-9002(01)01731-4.
- [44] Pierre Auger Collaboration, [Conventions for the Pierre Auger Project](#), [Online; accessed 05-October-2019].
- [45] P. Abreu et al., The Pierre Auger Observatory V: Enhancements, in: Proceedings, 32nd International Cosmic Ray Conference (ICRC 2011): Beijing, China, 2011. arXiv:1107.4807.
- [46] J. Brack et al., Absolute photometric calibration of large aperture optical systems, *Astroparticle Physics* 20 (6) (2004) 653 – 659. doi:10.1016/j.astropartphys.2003.09.004.
- [47] A. Aab et al., Spectral calibration of the fluorescence telescopes of the Pierre Auger Observatory, *Astroparticle Physics* 95 (2017) 44 – 56. doi:10.1016/j.astropartphys.2017.09.001.
- [48] R. Knapik et al., The Absolute, Relative and Multi-Wavelength Calibration of the Pierre Auger Observatory Fluorescence Detectors, in: Proceedings, 30th International Cosmic Ray Conference (ICRC 2007): Merida, Yucatan, Mexico, 2007, Vol. 4, pp. 343–346, [4,343(2007)]. arXiv:0708.1924.
- [49] P. H. Nguyen, [Energy systematics and long term performance of the Pierre Auger Observatory's fluorescence telescopes](#), Ph.D. thesis, The University of Adelaide (2018).
- [50] L. Tomankova, M. Bohacova, Relative FD Calibration - Effect of mirror and filter cleaning procedures, GAP2011_113, internal notes of the Pierre Auger Collaboration (2011).
- [51] I. Allekotte et al., The surface detector system of the Pierre Auger Observatory, *Nucl. Instrum. Meth. A*586 (3) (2008) 409 – 420. doi:10.1016/j.nima.2007.12.016.
- [52] M. Medina et al., Enhancing the Pierre Auger Observatory to the 10^{17} – $10^{18.5}$ eV range: Capabilities of an Infill Surface Array, *Nucl. Instrum. Meth. A*566 (2) (2006) 302 – 311. doi:10.1016/j.nima.2006.07.023.
- [53] S. Messina, Extension to lower energies of the cosmic-ray energy window at the Pierre Auger Observatory, Ph.D. thesis, University of Groningen (2016).
- [54] B. G. Keilhauer, Investigation of atmospheric effects on the development of extensive air showers and their detection with the Pierre Auger Observatory, Ph.D. thesis, Karlsruhe, Forschungszentrum (2004).
- [55] I. Valino, The flux of ultra-high energy cosmic rays after ten years of operation of the Pierre Auger Observatory, PoS ICRC2015 271. doi:10.22323/1.236.0271.
- [56] I. C. Maris, Measurement of the ultra high energy cosmic ray flux using data of the Pierre Auger Observatory, Ph.D. thesis, 51.53.01; LK 02 (2009). doi:10.5445/IR/200074438.
- [57] J. Hersil I. Escobar D. Scott G. Clark, S. Olbert, Observations of Extensive Air Showers near the Maximum of Their Longitudinal Development, *Phys. Rev. Lett.* 6 (1961) 22–23. doi:10.1103/PhysRevLett.6.22.

- [58] A. Aab et al., Reconstruction of inclined air showers detected with the Pierre Auger Observatory, *JCAP* 1408 (08) (2014) 019. doi:[10.1088/1475-7516/2014/08/019](https://doi.org/10.1088/1475-7516/2014/08/019).
- [59] R. Krause, Detection of Ultrahigh-Energy Cosmic Rays with the Auger Engineering Radio Array, *Nucl. Instrum. Meth. A* 845 378 – 382, proceedings of the Vienna Conference on Instrumentation 2016. doi:[10.1016/j.nima.2016.06.048](https://doi.org/10.1016/j.nima.2016.06.048).
- [60] F. G. Schröder, Radio detection of high-energy cosmic rays with the Auger Engineering Radio Array, *Nucl. Instrum. Meth. A* 824 (2016) 648 – 651, frontier Detectors for Frontier Physics: Proceedings of the 13th Pisa Meeting on Advanced Detectors. doi:[10.1016/j.nima.2015.08.047](https://doi.org/10.1016/j.nima.2015.08.047).
- [61] A. Aab et al., Observation of inclined EeV air showers with the radio detector of the Pierre Auger Observatory, *Journal of Cosmology and Astroparticle Physics* 2018 (10) (2018) 026–026. doi:[10.1088/1475-7516/2018/10/026](https://doi.org/10.1088/1475-7516/2018/10/026).
- [62] B. Daniel et al., The AMIGA enhancement of the Pierre Auger Observatory, *Journal of Physics: Conference Series* 632 (2015) 012088. doi:[10.1088/1742-6596/632/1/012088](https://doi.org/10.1088/1742-6596/632/1/012088).
- [63] Müller, Sarah, for the Pierre Auger Collaboration, Direct Measurement of the Muon Density in Air Showers with the Pierre Auger Observatory, *EPJ Web Conf.* 210 (2019) 02013. doi:[10.1051/epjconf/201921002013](https://doi.org/10.1051/epjconf/201921002013).
- [64] J. Abraham et al., A study of the effect of molecular and aerosol conditions in the atmosphere on air fluorescence measurements at the Pierre Auger Observatory, *Astroparticle Physics* 33 (2) (2010) 108 – 129. doi:[10.1016/j.astropartphys.2009.12.005](https://doi.org/10.1016/j.astropartphys.2009.12.005).
- [65] B. Fick M. Malek J. A. J. Matthews J. Matthews R. Meyhandan M. Mostafá M. Roberts P. Sommers, L. Wiencke, The Central Laser Facility at the Pierre Auger Observatory, *Journal of Instrumentation* 1 (11) (2006) P11003–P11003. doi:[10.1088/1748-0221/1/11/p11003](https://doi.org/10.1088/1748-0221/1/11/p11003).
- [66] P. Abreu et al., Techniques for Measuring Aerosol Attenuation using the Central Laser Facility at the Pierre Auger Observatory, *JINST* 8 (2013) P04009. doi:[10.1088/1748-0221/8/04/P04009](https://doi.org/10.1088/1748-0221/8/04/P04009).
- [67] S. BenZvi et al., The Lidar system of the Pierre Auger Observatory, *Nucl. Instrum. Meth. A* 574 (1) (2007) 171 – 184. doi:[10.1016/j.nima.2007.01.094](https://doi.org/10.1016/j.nima.2007.01.094).
- [68] L. Wiencke et al., Atmospheric "super test beam" for the Pierre Auger observatory, *Proceedings of the 32nd International Cosmic Ray Conference, ICRC 2011* 3 (2011) 145–148. doi:[10.7529/ICRC2011/V03/0741](https://doi.org/10.7529/ICRC2011/V03/0741).
- [69] A. Dorofeev et al., FD Absolute Calibration, April 2013, GAP2013_058, internal notes of the Pierre Auger Collaboration (2013).
- [70] J. R. Hörandel, A large radio array at the Pierre Auger Observatory, in: *Proceedings, 8th International Conference on Acoustic and Radio EeV Neutrino Detection Activities (ARENA 2018): Catania, 2018*.
- [71] P. Abreu et al., Antennas for the detection of radio emission pulses from cosmic-ray induced air showers at the Pierre Auger Observatory, *Journal of Instrumentation* 7 (10) (2012) P10011. doi:[10.1088/1748-0221/7/10/P10011](https://doi.org/10.1088/1748-0221/7/10/P10011).

- [72] M. L. Ahnen et al., Performance of the MAGIC telescopes under moonlight, *Astroparticle Physics* 94 (2017) 29–41. doi:10.1016/j.astropartphys.2017.08.001.
- [73] S. Archambault et al., Gamma-ray observations under bright moonlight with VERITAS, *Astroparticle Physics* 91 (2017) 34 – 43. doi:10.1016/j.astropartphys.2017.03.001.
- [74] R. Šmída, Programm to calculate FD shift times, private communication (2016).
- [75] Wikimedia Commons, [File:twilight-dawn subcategories.svg — wikimedia commons, the free media repository](#), [Online; accessed 28-February-2019] (2018).
- [76] S. Argiro et al., The Offline Software Framework of the Pierre Auger Observatory, *Nucl. Instrum. Meth. A* 580 (2007) 1485–1496. doi:10.1016/j.nima.2007.07.010.
- [77] R. Caruso et al., A photon background model for the FD trigger simulation, GAP2003_083, internal notes of the Pierre Auger Collaboration (2003).
- [78] T. Bergmann et al., One-dimensional hybrid approach to extensive air shower simulation, *Astropart. Phys.* 26 (2007) 420–432. arXiv:astro-ph/0606564.
- [79] A. Porcelli, Measurement of the Depth of Shower Maximum in the Transition Region between Galactic and Extragalactic Cosmic Rays with the Pierre Auger Observatory, Ph.D. thesis, KIT, Karlsruhe (2014).
- [80] B. Dawson for the Pierre Auger Collaboration, [The Energy Scale of the Pierre Auger Observatory](#), in: Proceedings, 36th International Cosmic Ray Conference (ICRC2019): Madison, Wisconsin, USA, 2019.
- [81] J. Zorn, Preparation of an Extended Measurement Cycle of the Fluorescence Telescopes of the Pierre Auger Observatory, Master’s thesis, Karlsruher Institut für Technologie (KIT) (2015).
- [82] J. Zorn et al., A photomultiplier tube test stand and on-site measurements to characterise the performance of photomultiplier tubes at increased background light conditions and lower gain, *Nuclear instruments & methods in physics research / A* 938 (2019) 20–28. doi:10.1016/j.nima.2019.05.065.
- [83] J. Zorn et al., The first measurement with the FD operated at a reduced PMT gain, GAP2015_021, internal notes of the Pierre Auger Collaboration (2015).
- [84] V. Harvey, VAOD at low gain, private communication (2019).
- [85] J. T. Brack et al., Absolute calibration of a large-diameter light source, *Journal of Instrumentation* 8 (05) (2013) P05014–P05014. doi:10.1088/1748-0221/8/05/p05014.
- [86] Labsphere, [4P-GPS-053-SL](#), [Online; accessed 03-October-2019].
- [87] M. Vacula P. Horváth M. Pech M. Palatka L. Chytka D. Mandát M. Hrabovský, P. Schovánek, Update on integrating sphere homogeneity measurements, talk at XY-Scanner working group meeting, part of future publication (September 2019).
- [88] Labsphere, [Optical-grade Spectralon® Reflectance Material](#), [Online; accessed 03-October-2019].
- [89] Labsphere, [Tech Guide: Integrating Sphere Uniform Light Source Applications](#), [Online; accessed 02-October-2019].

- [90] Roithner Lasertechnik GmbH, [UVLED365-110E](#), [Online; accessed 02-August-2019] (2019).
- [91] Hamamatsu, [S1336-44BQ](#), [Online; accessed 02-August-2019] (2019).
- [92] F. Werner, Design and Test of a Flying Light Source for the Calibration of the Auger Fluorescence Telescopes, Master's thesis, Karlsruher Institut für Technologie (KIT) (2010).
- [93] T. Heibges J. Berens E. Mayotte, J. Rautenberg, Absolute Photometric Calibration of the X-Y Scanner Light Source, Auger Analysis Meeting, Nijmegen (2019).
- [94] T. Heibges E. Mayotte, J. Rautenberg, Preliminary result of the sphere calibration, private communication (September 2019).
- [95] M. Vacula P. Horváth M. Pech L. Chytka M. Palatka D. Mandát J. Šupík L. Kocián M. Hrabovský, P. Schovánek, Latest update on spatial and angular homogeneity measurements of integrating sphere, talk at XY-Scanner working group meeting (2019).
- [96] IGUS®, [drylin®linear guides](#), [Online; accessed 29-August-2019].
- [97] A. Dorofeev et al., FD Response to Light Pulses, Auger Collaboration Meeting (November 2010).
- [98] J. Brack et al., Auger Fluorescence Detector Absolute Calibration January and June 2010, GAP2010_118, internal notes of the Pierre Auger Collaboration (201).
- [99] L. Tománková, Optical Properties and Calibration of the Pierre Auger Fluorescence Detector, Ph.D. thesis, Karlsruher Institut für Technologie (KIT) (2016). [doi:10.5445/IR/1000061954](#).
- [100] J. Debatin, Investigation of Optical Properties of the Fluorescence Telescopes of the Pierre Auger Observatory, Master's thesis, Karlsruher Institut für Technologie (KIT) (2015).
- [101] L. Nozka et al., Monitoring of mirror degradation of fluorescence detectors at the Pierre Auger Observatory due to dust sedimentation, *Journal of Instrumentation* 13 (05) (2018) T05005–T05005. [doi:10.1088/1748-0221/13/05/t05005](#).
- [102] V. Verzi, Status Report on FD Reconstruction, Auger Collaboration Meeting (November 2018).
- [103] J. Bellido, Tracking HEAT and CO calibrations and the effects on Xmax for the HeCo system, Auger Long Time Performance Phone-Meeting (May 2019).
- [104] G. Salina, preliminary FD calibration for the March / April shift, private communication (2019).
- [105] G. Salina, FD Calibration Status, Auger Collaboration Meeting (March 2019).